



저작자표시-비영리-변경금지 2.0 대한민국

이용자는 아래의 조건을 따르는 경우에 한하여 자유롭게

- 이 저작물을 복제, 배포, 전송, 전시, 공연 및 방송할 수 있습니다.

다음과 같은 조건을 따라야 합니다:



저작자표시. 귀하는 원저작자를 표시하여야 합니다.



비영리. 귀하는 이 저작물을 영리 목적으로 이용할 수 없습니다.



변경금지. 귀하는 이 저작물을 개작, 변형 또는 가공할 수 없습니다.

- 귀하는, 이 저작물의 재이용이나 배포의 경우, 이 저작물에 적용된 이용허락조건을 명확하게 나타내어야 합니다.
- 저작권자로부터 별도의 허가를 받으면 이러한 조건들은 적용되지 않습니다.

저작권법에 따른 이용자의 권리는 위의 내용에 의하여 영향을 받지 않습니다.

이것은 [이용허락규약\(Legal Code\)](#)을 이해하기 쉽게 요약한 것입니다.

[Disclaimer](#)

이학박사 학위논문

Precise Compositional and Structural Engineering  
of Multicomponent Nanostructures

다성분 나노 구조체의 정밀한 조성 및 구조에  
관한 연구

2019년 2월

서울대학교 대학원

화학부 무기화학

Mouhong Lin

Precise Compositional and Structural Engineering  
of Multicomponent Nanostructures

다성분 나노 구조체의 정밀한 조성 및 구조에  
관한 연구

지도교수 남좌민

이 논문을 이학박사학위논문으로 제출함

2018년 12월

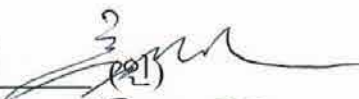


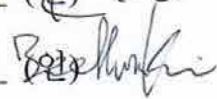

서울대학교 대학원


화학부 무기화학

Mouhong Lin

Mouhong Lin의 이학박사학위논문을 인준함

2018년 12월

위원장	홍병희	
부위원장	남좌민	
위원	이광엽	
위원	김지한	
위원	이동환	



# Abstract

## Precise Compositional and Structural Engineering of Multicomponent Nanostructures

Mouhong Lin

Department of Chemistry

The Graduate School

Seoul National University

One grand challenge in current nanotechnology is the increasingly stringent criteria on compositionality, dimensionality and functionality of materials at the nanometer scale. Elaborate design and controllable syntheses of multicomponent nanostructures with precise composition and delicate structure are especially desired for in-depth exploration of the electrical, optical and chemical interactions between these different components. Among various nanomaterials, metal and semiconductor nanocomponents are prominent candidates for these researches due to the strong electromagnetic (EM) and photoelectronic interactions between these nanoparticles (NPs). Metal nanocomponents, especially plasmonic metals (such as Au and Ag), are featured with high electron mobility, strong EM field localization capability and high photocatalytic activity, while semiconductor nanocomposites possess unique photoelectronic properties such as temperature-dependent conductivity, photo-induced charge separation and

dopability. The combination of them into metal-semiconductor heterostructures is thus of great interest in many different research fields, including nanoantenna, photocatalysis, optoelectronic devices and various plasmonic-enhanced applications. Due to the structure-dependent plasmonic property and the short lifetime of photogenerated hot carriers, the performance of nanodevices and nanosystems that supported by these heterostructures is highly sensitive to their structural nuances at the nanoscale. However, the precise compositional and structural engineering of these heterostructures remain challenging due to the lack of understanding on their surface/ interfacial energy and the lattice strain induced by the heterointerface.

In this thesis, we focused on the exploration of synthetic tools aiming to promote the precise controllability and structure tunability in heterointerface and multicomponent nanostructures. Special attentions were paid to the heterointerface and the accompanying lattice strain, which were further adopted as a thermodynamic driven force to guide structural evolution. The strategies we developed here were to minimize the interfacial energy/lattice strain under slow growth kinetic, either by crystal structure engineering of seeds in seed-mediated methods, or co-nucleation and simultaneous growth of multiple components to promote in-situ strain equilibrium.

In Chapter 1, recent advances in the synthetic strategy and property exploration of multicomponent structures, especially multimetallic and metal-semiconductor nanostructures, have been summarized. The difference between single component synthesis and multicomponent synthesis, and the structure-property relationship in multicomponent nanostructures were discussed. Some general experience and strategies such as epitaxial growth, ligand-based selectivity and thermodynamic

verse kinetic control can partially explain some phenomena in multicomponent synthesis. However, the intrinsic difference induced by heterointerface largely limits the efficiency of the synthetic tools developed in single-component systems. On the other hand, there were also new opportunities in the multicomponent synthesis due to the existence of heterointerface and lattice strain, which can be used to develop new synthetic methods that cannot be achieved in single component cases.

In Chapter 2, crystal structure engineering has been developed to perform heteroepitaxial growth between largely-lattice-mismatched gold and copper (with a degree of 11.4 %). Two types of crystal structures, including single crystalline and five-fold twin have been demonstrated in the copper secondary structure, induced by the crystal structure-engineered gold seeds, respectively. As a result of heteroepitaxial growth, a cubic shaped copper sub-NP was found in the single crystalline case, while a taper shaped copper sub-NP was obtained in the five-fold twin case. Such symmetry breaking results in a dramatically different electromagnetic communication between gold and copper, where strong enhancement was found in the gold-copper tip-taper nanoparticle. With the localized and enhanced the electromagnetic field, chemical reactions can be activated on the gold tip, and enhanced surface enhanced Raman spectrum (SERS) signal was also demonstrated.

In Chapter 3, the crystal structure corrected gold-copper nanostructures together with kinetic-controlled galvanic replacement have been utilized to obtain precise heterojunction controllability in copper-gold-silver multicomponent anisotropic nanoparticles (MAPs). We showed that two series of well-defined MAPs (transformative gold@copper-silver MAP and copper-gold-silver MAP) can be

synthesized in a high yield, and their structures and plasmonic properties are highly controllable. The nm-scale heterojunction engineering capability with three different components, the tunability over the ‘confined-neck junction’ to ‘open-neck junction’ and the fine balancing of far-field and near-field properties in MAPs offer great opportunity for plasmonic control and enhancement in various metal and semiconductor-based energy applications as well as diffusion-based catalytic applications.

In Chapter 4, a heterointerfacial strain equilibrium (HSE) strategy was explored using metal-semiconductor Ag-Ag<sub>2</sub>S NP as a model. Compared with seed-mediated methods, a HSE process was featured with (i) simultaneous nucleation and growth of multiple components, (ii) low precursor concentration enabled by establishing chemical equilibriums and (iii) surfactant with low facet preference. The HSE-directed growth of Ag-Ag<sub>2</sub>S NPs was studied by time-dependent HRTEM and XRD measurements, evidencing the phase transition of Ag and Ag<sub>2</sub>S. Moreover, the Ag-Ag<sub>2</sub>S NPs were found to possess remarkable thermodynamic stability against chemical oxidation and long term storage. This feature was further used for the site-specific galvanic exchange of Ag into various metal (M)-Ag<sub>2</sub>S (M=Au, Pd, Pt) nanostructures.

In Chapter 5, the one-pot synthesis of cubic Ag-Pt/Ag<sub>2</sub>S metal-semiconductor nanoframe (MSF) was developed by introducing the Pt/Ag<sub>2</sub>S heterointerface as an additional strain source in the HSE strategy. It led to the formation of highly concave Pt/Ag/Ag<sub>2</sub>S metal-semiconductor nanocube (MSC), which further transformed into a hollow MSF by self-etching effect. The MSF structures can be easily tuned from tetrahedron frames to cubic frames with different edge-to-body diameter ratios, simply by altering the Pt/S precursor ratio, indicating high

structure tunability. This method enables the tunable one-pot fabrication of crystalized semiconductor nanoframes with supported metal NPs. The high surface-to-volume ratio of nanoframe structures, the unique photoelectronic, biocompatibility and second NIR absorption of Ag<sub>2</sub>S, as well as the wide application of metal-semiconductor heterointerface suggest the great potential for these MSF nanostructures in catalysis, sensing and biomedical applications, especially deep penetration biotherapies.

**Keywords: Multimetallic; Metal-Semiconductor; Nanoframes; Structural engineering; Heterointerface; Plasmonic Antenna**

**Student Number : 2014-30845**



# Contents

<b>Abstracts.....</b>	<b>V</b>
<b>Contents.....</b>	<b>vii</b>
<b>List of Figures .....</b>	<b>xvii</b>
<b>List of Tables .....</b>	<b>xviii</b>

## **Chapter 1: Introduction**

<b>1.1 Introduction .....</b>	<b>1</b>
<b>1.2 Principles and strategies in nanosynthesis .....</b>	<b>1</b>
<b>1.3 Challenges and opportunities in multicomponent synthesis .....</b>	<b>6</b>
<b>1.4 Recent advances in multicomponent synthesis .....</b>	<b>8</b>
<b>1.5 Plasmonic enhancement of multicomponent nanostructures.....</b>	<b>13</b>
<b>1.6 Hot electron-driven water splitting reactions .....</b>	<b>19</b>

## **Chapter 2: Crystal Structure Engineering in Symmetry**

### **Breaking of Bimetallic Nanoparticles**

<b>2.1 Introduction .....</b>	<b>32</b>
<b>2.2 Experimental section.....</b>	<b>33</b>
<b>2.3 Results and Discussion .....</b>	<b>36</b>
<b>2.4 Conclusion.....</b>	<b>42</b>

## **Chapter 3: Precise Compositional Engineering and Optical Tuning in Multi-metallic Nanoantenna**

<b>3.1 Introduction .....</b>	<b>52</b>
<b>3.2 Experimental section.....</b>	<b>54</b>
<b>3.3 Results and Discussion.....</b>	<b>56</b>
<b>3.4 Conclusion.....</b>	<b>64</b>

## **Chapter 4: Synthesis of Monodisperse Ag-Ag<sub>2</sub>S NPs as Platform for Metal-Semiconductor Nanostructures**

<b>4.1 Introduction .....</b>	<b>77</b>
<b>4.2 Experimental section.....</b>	<b>79</b>
<b>4.3 Results and Discussions .....</b>	<b>81</b>
<b>4.4 Conclusion.....</b>	<b>87</b>

## **Chapter 5: Synthesis and Structure Engineering of Cubic Metal-Semiconductor Nanoframes**

<b>5.1 Introduction .....</b>	<b>100</b>
<b>5.2 Experimental section.....</b>	<b>103</b>
<b>5.3 Results and Discussions .....</b>	<b>104</b>
<b>5.4 Conclusion.....</b>	<b>108</b>
<b>Bibliography .....</b>	<b>117</b>

# List of Figures

## Chapter 1

**Figure 1.1.** (a) The essence of surface energy: Minimizing the energy of the system requires minimizing the number of the surface atoms with unfavorable interactions. (b) Models of the three major low-index planes (111, 100 and 110) in a face-centered-cubic metal and the corresponding numbers of bonds per surface unit cell. (c) Schematic illustrations showing the role of capping agents in directing the growth of a single-crystal seed made. (d) LaMer plot describing nucleation and growth process of monodisperse nanoparticle.<sup>1-2</sup>

**Figure 1.2.** (a) Schematic illustration of the iterative and cyclical process of reductive growth and oxidative dissolution for the synthesis of anisotropic nanoparticle products. (b) High quality single-crystalline gold nanostructures by using single crystalline seeds after iterative and cyclical process.<sup>3</sup> (c) Monodisperse bipyramids, NRs, and decahedra from pentatwinned seeds. (d) TEM images of samples prepared using seeds at different heating times. (e) High quality pentatwinned gold nanostructures by using pentatwinned gold seeds after thermal process.<sup>4</sup>

**Figure 1.3.** (a) In crystallized nanostructures, atom deposition is favored by epitaxial growth which follows the established lattice structures. (b) The heterointerface that combines two types of atoms in atomic bond is associated with the mismatch of lattice parameters. (c) Three types of growth mode at the heterointerface depending on the degree of lattice mismatch.

**Figure 1.4.** (a) Lattice structure of the overgrowth phase in the 2D and the 3D mode of the Stranski-Krastanov model. (b) Morphological evolution of the

seed/Au heterostructure during the pre-nucleation, nucleation and growth periods. The contact angle  $\theta_c$  between the seed and the Au is indicated for the core/shell and the dumbbell. (c) Schematic illustration of the stresses,  $\sigma_{\text{shell}}$ ,  $\sigma_{\text{seed}}$  and  $\sigma_{\text{inter}}$ , within core/shell and dumbbell NPs. (d) STEM-EDX mapping of a CoPt<sub>3</sub>/Au dumbbell. (e) Atomic-resolution annular bright-field STEM image of a CoPt<sub>3</sub>/Au dumbbell and the corresponding FFT image overlapped with those from the seed (blue) and Au (red) domains. (f, g) Magnified images of the area indicated in the insets. Yellow straight lines are extensions of the seed lattice. The direction of the displacement of the lattice planes (white) with respect to the seed lattice (yellow) is indicated with arrows. (h) Magnified image showing 7 adjacent monolayers over the (111) interface and (i) intensity profiles along the dashed lines in the image.<sup>5</sup>

**Figure1.5.** (a) The scanning-probe block copolymer lithography-mediated synthesis of multimetallic NPs and a polyelemental library of unary and multimetallic NPs made via this technique. (b) A schematic illustration of the surface inorganometallic chemistry for the synthesis of supported bimetallic NPs. The HAADF-STEM images of 10 types of supported bimetallic NPs synthesized by this approach. Scale bars are 10 nm.<sup>6</sup> (c) Schematic illustration of the non-epitaxial growth process of hybrid core-shell nanostructures, as well as TEM images and XRD patterns of different synthetic stages. Scale bars are 5 nm. (d) Schematic illustration of the growth procedure of the Au-(CdS+PbS) NP with monocrystalline cation species within the shell (left) and Au-CdS<sub>1-a</sub>Se<sub>a</sub> NP with monocrystalline anion species within the shell (right). Scale bars are 5 nm.<sup>7</sup>

**Figure1.6.** (a) Schematic illustration of the stepwise synthesis of M-Pt-Fe<sub>3</sub>O<sub>4</sub> heterotrimers (M=Ag, Au, Ni, Pd) as well as the possible NP products and their experimental yield. TEM images of Pt nanoparticle seeds (b), Pt-Fe<sub>3</sub>O<sub>4</sub>

heterodimers (c) and Au-Pt- Fe<sub>3</sub>O<sub>4</sub> (d), Ag-Pt- Fe<sub>3</sub>O<sub>4</sub> (e), Ni-Pt- Fe<sub>3</sub>O<sub>4</sub> (f) and Pd-Pt-Fe<sub>3</sub>O<sub>4</sub> (g) heterotrimers. Scale bars are 25 nm. (h) Photographs of a vial that contains Au-Pt-Fe<sub>3</sub>O<sub>4</sub> heterotrimers in hexane with (left) and without (middle) external magnet, and after precipitation with ethanol (right).<sup>8</sup> TEM images and corresponding schematics as control experiments of Ag nucleation on: (i) Fe<sub>3</sub>O<sub>4</sub> NPs, (j) Pt NPs, (k) mixture of Fe<sub>3</sub>O<sub>4</sub> and Pt NPs, (l) Pt-Fe<sub>3</sub>O<sub>4</sub> NPs. Scale bars are 20 nm (main panel) and 5 nm (inset), respectively. (m) Schematic illustration of a solid state protection group in colloidal multicomponent synthesis. (n) Evidence of NP growth from Fe<sub>3</sub>O<sub>4</sub>-Pt NP to Fe<sub>3</sub>O<sub>4</sub>-Pt-Ag NP. (o) Evidence of NP growth from Fe<sub>3</sub>O<sub>4</sub>-Pt NP with iron oxide shell to Ag-Fe<sub>3</sub>O<sub>4</sub>-Pt NP.<sup>9</sup>

**Figure 1.7.** (a) Schematic illustration and solution color of Au-Ag hybrid NPs from Ag nucleation on DNA modified Au NPs with varying salt concentration. (b) TEM images of NPs synthesized at salt concentrations of (1) 0.3, (2) 0.1, and (3) 0.003 M and (4) the corresponding UV-vis spectra. (c) Proposed reaction mechanism at different salt concentrations. (d) Zeta potentials for DNA-AuNPs at 0.003 and 0.3 M salt concentration (left); HRTEM images of Ag nanostructure formation on DNA-AuNPs at intermediate stages (right).<sup>10</sup> (e) Schematics illustrating the four transformation modes of (Au NR-ligand)@PSPAA. Contraction, bimodal contraction, dissociation, and winding modes. (f) The ligand dependence is summarized in the table.<sup>11</sup>

**Figure 1.8.** (a) Schematic and corresponding TEM of an individual photosynthetic unit showing the inner Au nanorod (NR), the TiO<sub>2</sub> cap decorated with Pt NPs, and the Co-OEC material deposited on the lower portion of the Au NR. (b) Hydrogen produced per hour with various illumination wavelengths. (c) At visible wavelengths, the responsivity of the Au NR/TiO<sub>2</sub>/platinum plasmonic

photocathode (line and symbols) tracks the extinction spectrum of the device (red line) faithfully.<sup>12</sup> (d) Scheme of a calculation model consisted of an Ag NR vertically posited on the TiO<sub>2</sub> substrate. (e) The electron injection efficiency and (f) quantum efficiency of the Ag NRs of different aspect ratios.<sup>13</sup> (g) Gold taper used to adiabatically compress a surface plasmon polariton (SPP) into the Au/Si Schottky junction. (h) Geometry of the Au taper that guide the SPP to the tip junction of Au/GaAs interface where strong EM field was localized.<sup>14</sup>

**Figure 1.9.** (a) Chemical structures of pATP (left), pNTP (right), and DMAB (bottom). (b) The time-dependent SERS spectra of DMAB produced from pATP by selective catalytic coupling reaction on silver nanoparticles.<sup>15</sup> (c) Schematic diagram of the photoinduced charge transfer process for nitro and amine functional group on silver surfaces.<sup>16</sup> (d) Proposed SPAC mechanism of conversion process from pATP to DMAB under an atmosphere with both O<sub>2</sub> and H<sub>2</sub>O vapor (upper panel).<sup>17</sup>

**Figure 1.10.** (a) TEM image, (b-e) HAADF-STEM image and elemental maps, and (f-h) elemental profiles of Au NR/TiO<sub>2</sub> dumbbells. (i) Comparison of hydrogen generation rate by various catalysts. (j) Normalized concentration of methylene blue at different irradiation time. Structure and mechanism of operation under visible light of (k) an individual Au NR/TiO<sub>2</sub> dumbbell and (l) core/shell Au NR@TiO<sub>2</sub>.<sup>18</sup>

## Chapter 2

**Figure 2.1.** Schematic illustration of crystal structure-engineered gold seeds for symmetric breaking of gold-copper nanoparticles.

**Figure 2.2.** Cs-corrected high-resolution transmission electron microscopy (HRTEM) images of (a) a gold single-crystalline seed (GSS), (b, c) a gold-copper core-shell (GCCS) NP. Scale bars are 5 nm.

**Figure 2.3.** (a) Schematic illustration of icosahedral twin and HRTEM images of two representative gold icosahedral twin seeds (GTSS). (b) Schematic illustration of the twin structure in gold-copper tip-taper (GCTT) NP and (c, d) HRTEM characterization of a typical GCTT NP. For both GCCS and GCTT, identical growth conditions were used except the difference of gold seeds. Scale bars are 5 nm.

**Figure 2.4.** Schematic illustrations of icosahedral twin seed (a) and GCTT (b, c and f) structures at different orientations. Schemes b, c and f correspond to Figure 1g, S3d and S3g, respectively. (d) HRTEM and (e) corresponding FFT images of a GCTT NP when the electron beam was applied in parallel to the five-fold twin axis. (g, h) HRTEM images of a GCTT NP when the electron beam was applied with a small angle to the five-fold twin axis. Scale bars are 10 nm.

**Figure 2.5.** HRTEM analysis of the crystallinities in GSS (a-c) and GTS (d-f) particles. Examples in crystallinity identification by HRTEM and FFT analysis are given in both GSS (b and c) and GTS (e and f) cases. In each case, 200 particles were analyzed by Cs-corrected HRTEM and FFT. The identification of five-fold twinned NPs was referred to previous experimental and theoretical studies.<sup>3-5</sup> The cases with unidentifiable crystallinity, marked with pink boxes in c and f, were excluded in the data analysis, and other cases correspond to the different types of crystallinity as indicated in g and h. The percentage of single-crystalline NPs, five-fold twinned NPs and single-twinned NPs for GSS (g) and GTS (h) samples are also shown.

**Figure 2.6.** The calculated electromagnetic field distributions of (a) GCCS and (b) GCTT NPs. Scare bar: 10 nm.

**Figure 2.7.** The TEM images and UV spectra of 4-ATP-modified GSSs (a, b) and 4-ATP-modified GTSs (e, f). The TEM images and UV spectra of GCCS NPs using 4-ATP-modified GSSs as seeds (c, d) and GCTT NPs using 4-ATP-modified GTS NPs as seeds (g, h), respectively.

**Figure 2.8.** Schematic illustrations of the photocatalytic reactions on (a) GCCS and (c) GCTT surfaces. The SERS spectra of (b, black line) 4-ABT-modified GSSs, (b, red line) 4-ABT-modified GCCS NPs, (d, black line) 4-ABT-modified GTSs and (d, red line) 4-ABT-modified GCTT NPs (▼: 4-ABT; ■: 4,4'-DMAB).

### Chapter 3

**Figure 3.1.** Schematic illustration of galvanic replacement reaction using GCCS NP (a) and GCTT NP (b) as templates. The electrochemical nature of galvanic replacement reaction provides enhanced site specificity for GCTT structure while the gold tip serves as a “nano-electrode” to conduct the galvanic current.

**Figure 3.2.** (a) Tuning of gold@copper-silver (G@CS) multicomponent anisotropic nanoparticles (MAPs) from GCCS NPs by altering the reaction extent of galvanic replacement reaction. HRTEM images and corresponding EDX mapping images of GCCS NPs and the corresponding galvanic replacement products. (b) Corresponding digital image and extinction spectra of GSS, GCCS NP and G@CS series MAPs. Scale bars are 20 nm.

**Figure 3.3.** (a) Tuning of copper-gold-silver (CGS) MAPs from GCTT NPs by altering the reaction extent of galvanic replacement reaction. HRTEM images and



corresponding EDX mapping images of GCTT NPs and the corresponding galvanic replacement products. (b) Corresponding digital image and extinction spectra of GTS, GCTT NP and CGS series MAPs. Scale bars are 20 nm.

**Figure 3.4.** (a) TEM image of CGS-1-0 MAPs synthesized without the addition of PVP. (b) Magnified image of a CGS-1-0 MAP showing an elongated gold junction, and (c) the corresponding EDX mapping pattern. Scale bars are 100 nm and 10 nm in a and b respectively.

**Figure 3.5.** (a) Schematic illustration of the heterointerface evolutions mechanism in MAPs. GCCS and GCTT NPs were initially capped with PEI (a good ligand for copper), and then partially replaced by PVP (a bad ligand for copper and a good ligand for silver) during the galvanic replacement reaction. Due to PEI protection, multiple nucleation of silver is inhibited, and the polymer exchange mechanism allows us to fine tune the junction properties through the exchange rate. (b, c) TEM images of junction-engineered (b) G@CS MAP series and (c) CGS MAP series, as well as corresponding high-magnification HRTEM images showing four junction morphologies (I to IV), respectively. Scale bars are 20 nm and 5 nm in low-magnification and high-magnification images, respectively.

**Figure 3.6.** Extinction spectra of (a) G@CS-1 and (b) CGS-1 series MAPs synthesized by varying PVP concentrations. Insets show the effect of PVP concentration on NIR peak wavelength (solid black dots) or peak intensity (hollow red bars).

**Figure 3.7.** The extinction cross-sections of (a) the junction-engineered G@CS (models M1 to M4) and (b) CGS (models M5 to M8) MAPs in the NIR region.

**Figure 3.8.** The electric field distributions (left) and magnified junction areas (right) of (a) M1, (b) M2, (c) M3 and (d) M4, respectively, at their respective charge transfer plasmon (CTP) peak wavelengths. Scale bars are 5 nm.

**Figure 3.9.** The electric field distributions (left) and magnified junction areas (right) of (a) M5, (b) M6, (c) M7 and (d) M8, respectively, at their respective charge transfer plasmon (CTP) peak wavelengths. Scale bars are 5 nm.

**Figure 3.10.** The volume integral of square of electric field ( $E^2$ ) from the 2-nm-periphery of each structure ( $\int E_{periphery}^2$ , gray bars) and the defined junction area ( $\int E_{junction}^2$ , black bars).

## Chapter 4

**Figure 4.1.** (a) SEM and (b) TEM images of Ag-Ag<sub>2</sub>S NPs. (c) TEM image showing Ag-Ag<sub>2</sub>S NPs super lattice. (d) EDS mapping result of an Ag-Ag<sub>2</sub>S NPs.

**Figure 4.2.** (a) HRTEM image of a 30-nm Ag<sub>2</sub>S NP. (b-d) Time dependent HRTEM images showing various growth stages of Ag-Ag<sub>2</sub>S NPs, ranging from 20 min (S1), 40 min (S2) to 120 min (S3). Scale bars are 10 nm. (e) EDX spectrum and (f) line profile result showing the elemental distribution of sample S3. (g) Time dependent XRD patterns showing various growth stages of Ag-Ag<sub>2</sub>S NPs and the 30-nm Ag<sub>2</sub>S NP.

**Figure 4.3.** The effect of CTAC concentration to the size and shape of Ag-Ag<sub>2</sub>S NPs. (a-c) TEM iamges show the Ag-Ag<sub>2</sub>S NPs as CTAC concentration increased from 100 mM (Figure 4.1a), 120 mM (a), 140 mM (b) to 160 mM (c). (d) Summery of Ag and Ag<sub>2</sub>S nanocomponent size synthesized at various CTAC

concentration: 100 mM (I), 120 mM (II), 140 mM (III) to 160 mM (IV), indicating a self-limiting growth behavior.

**Figure 4.4.** Etching of Ag from Ag-Ag<sub>2</sub>S NPs in 1% PVP using Fe(NO<sub>3</sub>)<sub>3</sub> solution as etching reagent at a concentration of 10 mM.

**Figure 4.5.** Effect of sulfuration to the structure of Ag-Ag<sub>2</sub>S NPs. TEM images of the products after reacting the Ag-Ag<sub>2</sub>S NPs with (a) 0 mM, (b) 0.1 mM, (c) 0.2 mM, (d) 0.3 mM, (e) 0.5 mM, (f) 0.8mM of Na<sub>2</sub>S<sub>2</sub>O<sub>3</sub> in 100 mM CTAC at 95° C for 1 hour. The Ag-Ag<sub>2</sub>S NPs first remained similar (a-c), and then transformed in shape (d-e) and finally became pure Ag<sub>2</sub>S NPs (f).

**Figure 4.6.** (a) HRTEM, (b) XRD patterns and (c) UV-vis spectra of Ag-Ag<sub>2</sub>S NPs after 3 months of synthesis.

**Figure 4.7. (a)** Schematic illustration of the site-selective heterointerface evolution between Ag and various noble metals. (b) Schematic illustrations of the galvanic replacement reactions and the corresponding multi-component NPs.

**Figure 4.8.** (a,b) HRTEM images, (c) EDX mapping and line profile results of Au-Ag<sub>2</sub>S NPs.

**Figure 4.9.** (a,b) HRTEM images, (c) EDX mapping and line profile results of Ag<sub>2</sub>S@Pd NPs.

**Figure 4.10.** (a,b) HRTEM images, (c) EDX mapping and line profile results of Ag-Ag<sub>2</sub>S@Pt NPs.

## Chapter 5

**Figure 5.1.** (a) TEM image, (b) HADDF image and (c) EDX mapping images of the MSFs. (d) Low magnification and (e, f) high magnification Cs-HRTEM images of MSFs.

**Figure 5.2.** (a) Cs-HRTEM images of MSFs. High magnification images showing lattice structures of (b) a single MSF and (c) the featured corners.

**Figure 5.3.** (a) Low magnification and (b) high magnification SEM images showing the 3D structure of MSFs. (c) Tilted TEM images showing the 3D geometry of MSFs at different orientations.

**Figure 5.4.** (a, b) A single MSF under HAADF-STEM mode, as well as (c) the EDX mapping images, (d) EDX line profile and (e) EDX spectrum showing elemental compositions. (f) XPS spectrum of Pt<sub>4f</sub> in MSFs.

**Figure 5.5.** (a) High resolution SEM image of MSCs. (b) HRTEM image and (c) corresponding SAED pattern and (d) EDX line profile results of a single MSC. (e) Air-based in-situ TEM observations of the transformation from a MSC to a MSF.

**Figure 5.6.** (a) Schematic illustration of the evolution of Ag<sub>2</sub>S@Pt NPs from stepwise galvanic replacement reaction between Ag on Ag-Ag<sub>2</sub>S NP and Pt under 95°C. TEM and Cs-HRTEM of 30 min (b, c), 60 min (d, e) and 180 min (f, g) products. (h) XRD patterns of the Ag<sub>2</sub>S@Pt NPs under various reaction time.

**Figure 5.7.** Schematic illustration and TEM images of precisely-engineered MSFs by increasing the ratio of K<sub>2</sub>PtCl<sub>4</sub> to Na<sub>2</sub>S<sub>2</sub>O<sub>3</sub>.

## List of Tables

### Chapter 2

**Table 2.1.** The geometric parameters of Au seed, GCCS and GCTT.

### Chapter 3

**Table 3.1.** Summary of reaction conditions for synthesis of G@CS and CGS MAPs.

**Table 3.2.** The geometric parameters for gold, copper and silver components in simulation models of various MAPs structures.

### Chapter 4

**Table 4.1.** Standard potentials of half-cell reactions involving some metals participating in galvanic replacement/deposition reactions.

# Chapter 1: Introduction

## 1.1 Background

As advanced application demands continue to expand, multicomponent nanostructures with growing complexity and functionality are increasingly desired.<sup>5, 19-20</sup> Compared with those for single component nanoparticles (NPs), synthetic tools that customized for multicomponent nanostructures are extremely primitive and deficient. The presence of heterointerface that directly bonded two foreign materials into a heterostructure brings up the competition of two different lattice structures at the nanoscale. Lattice strains are thus amplified due to the lattice contraction or lattice expansion in the “core” or “shell” materials,<sup>21</sup> usually depending on their lattice constant. The lattices of these strained materials are not in their relaxed conditions, thus possessing higher surface energy and unexpected growth tendency driven by the restoring force. Thus adds up the barriers for referring of strategies in single component syntheses, which mainly based on facet control under low lattice strain conditions. If the lattice strains are high enough to overcome the energy barrier for atom dislocation, defects are generated to release strains. As a result, epitaxy and highly-crystallized heterostructures were generally found between materials with relatively low lattice mismatch (such as Au/Ag and Pt/Pd). However, the existence of heterointerface and lattice strain also induced new opportunities and controllabilities in syntheses, on condition that these strains can be rationally employed to promote that formation of complex heterostructures of interest.

## 1.2 Principles and strategies in nanosynthesis

### 1.2.1 The interface

The most important difference between nanostructure and bulk material is the amplified NP/air or NP/liquid interface due to the large surface area of NP. Unlike the atoms located inside the NP that bonded at their thermodynamic stable construction, those atoms on the outermost surface of NP are half-bonded (as illustrated in **Figure 1.1a**).<sup>1</sup> As a result, the physiochemical properties of these surface atoms can vary with their chemical environment, naming their bonding energy with surrounding atoms, their interaction with ligands and the collective behavior with other atoms (such as plasmonic effect).<sup>22</sup> The controlling of NP interface means controllability over size (interface area), shape (equilibrium state of interface evolution), functionality (interface type), etc. However, the interface state of a specific NP is an ensemble result of various factors in the often complicated synthesis conditions. To precisely control the NP interface, one have to look at the dynamic evolution of NP interface from both inner factors (crystal structure, lattice strain, etc.) and outer factors (ligand, solvent, etc.)

Among the simplest nanostructures are those that contain single inorganic component. Due to the strong metal-metal bonding, metal nanostructures represent the highest precise controllability and morphology tunability.<sup>23</sup> Current synthetic capability includes uniformity, morphology, dimensionality, and functionality, ranging from simple geometries (cubes, rods, octahedrons etc.) to complex architectures (core-satellite, chiral structures, core-gap-shell, etc.).<sup>4, 24-26</sup>

The synthesis principle in these structures is mainly concerned in facet level, via manipulation the growth rates of different facets to effectively tune their ratio on the nanostructure surface, thus generating various geometries.<sup>23</sup> The strategies to

realize facet selectivity and growth rates can be mainly divided into three ways: (i) intrinsic surface property, (ii) dynamic ligands and (iii) nuclei engineering.

### **1.2.2 Intrinsic surface property**

As shown in **Figure 1.1a**, the minimizing the surface energy provides the driving force for material growth, which is the minimization of number of the surface atoms with unfavorable interactions.<sup>1</sup> For a metal nanocrystal, its equilibrium shape cannot be spherical because many high-index facets with relatively high specific surface free energies would be required for the formation of a perfect sphere.<sup>2</sup> Instead, various facets are formed according to different internal (with surrounding atoms) and external (with ligands or surfactants) bonding conditions under the governing of surface energy (**Figure 1.1a**). In face-centered cubic (fcc) metals, three major low-index planes are  $\langle 111 \rangle$ ,  $\langle 100 \rangle$  and  $\langle 110 \rangle$ , corresponding to different bonding number with surrounding atoms (**Figure 1.1b**). Since facets on fcc crystal surface are symmetrically-distributed, intrinsic facet property difference has been widely utilized in the synthesis of symmetric metal nanocrystals. Simplest example is the cubic nanostructure in fcc metals, which is a result of a faster intrinsic growth rate along  $\langle 111 \rangle$  facets over  $\langle 100 \rangle$  facets. The final structure is enclosed by those facets with slower growth rate, thus resulting a  $\langle 100 \rangle$  enclosed cubic structure.

### **1.2.3 Dynamic ligands**

In solution, the ligand/facet interaction is mostly weak interaction (such as van der Waal force, electrostatic adsorption and hydrophobic effect), thus being a dynamic process. The ligands adsorb to and detach from the nanoparticle facets in dynamic equilibrate.<sup>27</sup> Therefore, further atom deposition has to overcome the barrier of ligand adsorption, generating the growth rate difference according to



the ligand/facet affinity. Assuming all the facets are equally favored, a spherical shape with lowest surface to volume ratio would be preferred (**Figure 1.1c**).<sup>2</sup> At the other extreme, if only one facet is favored, such as  $\langle 111 \rangle$  to octahedral and  $\langle 100 \rangle$  to cubes, a polyhedron with sharp edges and corners will be preferred.<sup>1</sup> Playing between these two extremes, the selection of ligand allows the design of nanostructures with multiple facets and morphologies.

#### **1.2.4 Nuclei engineering**

Since facets play an important role in the subsequent atom deposition, the initial nuclei surface becomes crucial. According to LaMer plot (**Figure 1.1d**), the formation process of monodisperse nanocrystals includes three stages.<sup>28</sup>

Stage I (Pre-Nucleation): Nucleation does not occur even under supersaturated condition ( $S > 1$ ) due to the high energy barrier for spontaneous homogeneous nucleation.

Stage II (Nucleation): Nucleation occurs when the degree of supersaturation is high enough to overcome the energy barrier for nucleation, resulting in the formation and accumulation of stable nuclei.

Stage III (Growth): Nucleation is effectively inhibited as precursor concentration decreases and nanoparticles keep growing as long as the solution is oversaturated.

To produce monodisperse nanoparticles, one critical thing is to achieve burst nucleation and diffusion-controlled growth. Both one-pot and seed-mediated processes have been utilized to synthesize monodisperse nanocrystals by separating nucleation and growth. The hot injection method for monodisperse quantum dots is first developed by M. G. Bawendi<sup>29</sup> The mechanism is achieving short burst of homogeneous nucleation by rapid injection of colder organometallic precursor into a hot coordinating solvent at 300°C. Nucleation in

subsequent nanocrystal growth is effectively inhibited due to the decrease in temperature and precursor concentration. A majority of high-quality colloidal nanostructures have been developed through seed-mediated methods because higher controllability and tunability can be achieved. Development of multiple seed preparation methods enriches the toolbox for the synthesis of precisely-designed nanostructures. When Michael Faraday first synthesized colloidal gold nanoparticles by wet chemistry in 1857, he understood it as “activated gold” due to the red color.<sup>30</sup> The understanding of these tiny nanocrystals was greatly promoted by the invention of electron microscopes in 19<sup>th</sup> century. At first electron microscopes can only differentiate the diameter of nanocrystals roughly. With the development of transmission electron microscopes, nowadays it is able to examine the lattice configurations of nanoparticles at the atomic level. Although it is still challenging to manipulate nanocrystals like molecules in organic chemistry, the precise synthesis of single component nanoparticles have been largely developed. People begin to understand that well-controlled nanoparticle growth is based on epitaxial growth after the formation of nuclei.

Careful engineering of nuclei can largely enhance the thermodynamic and kinetic controllability. The basic principle is not only separation of nucleation and growth stage in LaMer plot, but also the uniformity and quality of nuclei. For example, structure refinement has been developed by Mirkin’s group to optimize the uniformity of single-crystalline gold nanosphere seeds. As shown in **Figure 1.2a**, starting from purified single crystalline seeds, reductive growth and oxidative dissolution were performed several rounds for obtaining highly spherical gold seeds, which were demonstrated to be critical for the production of highly

uniform gold nanostructures by seed-mediated secondary growth.<sup>3</sup> For this technique, single crystallinity and highly spherical seed shape are equally important to achieve a homogeneous surface energy distribution on the seeds. As demonstrated by the authors, the quality of the overgrowth nanostructures was directly affected by the quality of seeds, which is a foundational step for the subsequent kinetic and thermodynamic control (**Figure 1.2b**).

Besides single-crystalline systems, other well-defined crystalline systems, such as various polycrystalline systems, also support nuclei engineering for highly controllable nanostructures. However, due to the relatively high surface energy, it remains challenging to obtain identify polycrystalline seeds at a high yield. Recently, Ana Sánchez-Iglesias et al reported a thermally-induced twinning method for high-yield pentatwinned seeds (**Figure 1.2c**).<sup>4</sup> Interestingly, the yield of these pentatwinned seeds increased with the thermal treatment time (**Figure 1.2d**). Using these twin seeds largely improves the synthetic yield of bipyramids, nanorods (NRs), and decahedra comparing with other methods (**Figure 1.2e**). These works demonstrated that nuclei engineering is a powerful method for the precise control of nanoparticle growth.

### **1.3 Challenges and opportunities in multicomponent synthesis**

#### **1.3.1 Heterointerface**

One grand difference between multicomponent nanostructure and single-component nanostructure is the existence of heterointerface or not. As described in 1.2.1, interface is special in NP synthesis due to the special bonding condition of surface atoms. As shown in **Figure 1.3a**, atom deposition on single-crystalline interface is favored by epitaxial growth, referring to the deposition of a crystalline overlayer on a crystalline substrate. In multicomponent

nanostructures, besides of surface atoms, atoms located at the heterointerface are also of particular interest. These atoms partially bond with their foreign counterparts from another material (**Figure 1.3b**), which alters their electronic structure and leads to the as called “lattice mismatch effect”. Due to the lattice mismatch, at least one part of the atoms across a heterointerface have to partially change into their thermodynamic unstable lattice structure causing a lattice strain. Such phenomenon was first found in 2D films, where three known modes of heteroepitaxial growth have been observed, including Volmer-Weber (V-W) mode, Frank-van der Merwe (FvdM) mode<sup>31</sup> and Stranski-Krastanow (SK) mode (As shown in **Figure 1.3c**).<sup>32</sup>

Recently, Soon Gu Kwon et al. reveals the evolution of the heteroepitaxial structure in the synthesis of multicomponent NPs by in situ synchrotron X-ray scattering and atomic resolution HRTEM.<sup>5</sup> As shown in **Figure 1.4**, they suggested that such mechanisms in 2D films also apply to multicomponent NPs, where the mechanical deformation of the seeds and the overgrowth phase (**Figure 1.4a**) in turn affects the heterogeneous nucleation and growth symmetric (**Figure 1.4b**). At the beginning of the growth of Pt alloy/Au and Pt/Au dumbbells, heteroepitaxial growth of gold (prenucleation) are found at the expense of a lattice stress of 2.4 GPa on the seed. Anisotropic nucleation then happens and the growth direction was governed by the stress relief (**Figure 1.4c**). Atomic resolution HRTEM further revealed that the relief of the lattice strain in the shell was through the slip of Au <111> atomic layers at the seed/Au heterointerface (**Figure 1.4e to i**). This leads to the breaking of the heteroepitaxy and to the nucleation of a strain-free Au domain at the <001> plane (**Figure 1.4e**), similar to the 2D-to-3D transition in the S-K mode (as shown in **Figure 1.3c**).

### **1.3.2 Challenges and limitations in multicomponent synthesis**

The lattice strain that associates with heterointerface has induced multiple challenges in the controllability over both heterointerface itself and the overall multicomponent structure.<sup>19-20, 33-34</sup> Such challenges come from both the uncontrolled atom dislocation and the overwhelming surface energy, which are associated with the stacking fault energy of the materials and the insufficient protection of ligands. Metal components have relatively low stacking fault energy, which means that atom dislocation has relatively low energy barrier, thus defect formation is relatively favored.<sup>35</sup>

To improve structure controllability, seed-mediated methods are widely investigated in multicomponent synthesis.<sup>5, 36-38</sup> Seeds in desired shape can be prepared in advance and heterogeneous nucleation of another material were performed in the next step. The seed-mediated method allows the synthesis of multicomponent nanostructures in diverse morphologies, including core-shell, Janus and tetrapods. However, the controllability of overgrowth material is highly limited to the degree of lattice mismatch. Typical low lattice-mismatched metal pairs such as Au/Ag and Pt/Pd can still take advantage of heteroepitaxial growth. As the lattice mismatch becomes larger, it starts to affect the morphology of the heterostructured NPs.

## **1.4 Recent advances in multicomponent synthesis**

### **1.4.1 Substrate-supported isolated nanoreactor**

In contrast with seed-mediated methods, simultaneously growing multiple components into one well-defined NP is challenging due to the intercrossing of multiple nucleation and growth events, as well as the uneven consumption and diffusion of precursors. Thus several substrate-based methods have been

developed for the universal synthesis of supported multimetallic NPs.<sup>6,39</sup> Recently, Chen et al. adopted dip-pen lithography to form small droplets on the substrate, forcing the precursors to grow into single NPs containing various combinations of five different transition metal ions.<sup>6</sup> As shown in **Figure 1.5a**, the as-developed scanning-probe block copolymer lithography (SPBCL) can deliver attoliter-scale volumes of droplet to a desired location on a surface, which physically creates a nanoreactor for polymers with metal ion precursors to transform into individual site-isolated NPs upon thermal treatment. Based this mechanism, up to five elements consisting Au, Ag, Cu, Co, and Ni was investigated to the combinatorial synthesis of multimetallic NPs. It offers great opportunity for the discovery of physiochemical properties of some multimetallic NPs, such as quinary NPs that cannot be obtained by other method. However, the productivity of SPBCL is highly limited especially when it comes to large scale synthesis. Very recently, Ding et al. reported that adsorbing the double complex salts (DCSs) formed by a cation like  $\text{Pd}(\text{NH}_3)_4^{2+}$  and an anion like  $\text{IrCl}_6^{2-}$  from organic solvents onto silica surface, followed by high temperature treatment under hydrogen gas flow. As shown in **Figure 1.5b**, based on the strong substrate/precursor interaction, metal precursors were successfully anchored to the hydroxide groups on the silica substrate, allowing the following site-isolated formation of small binary NPs. Both of the above methods are taking advantage of the isolated precursor/substrate nanoreactor to form site-isolated multicomponent NPs, which largely improves the universality of the method comparing with wet-chemistry approaches.

#### **1.4.2 Heterointerface reorganization**

To overcome the limitations of structure controllability in multicomponent synthesis, especially when the lattice mismatch is large, new synthetic strategies have been developed. One strategy is based on the idea that lattice strain varies with the condition of heterointerface. Zhang et al. developed a nonepitaxial growth strategy to obtain core-shell multicomponent nanoparticles with large lattice mismatches.<sup>7</sup> Because monocrystalline growth of the semiconductor shell is fully directed by chemical thermodynamic properties of reactions within the matrix, the shell's lattice structure can be independent of that of the core NPs, thus circumventing the limitations imposed by epitaxial strategies.<sup>7</sup> As shown in **Figure 1.5c**, Au-Ag core-shell NP (S2) was first grown from Au seed (S1), followed by sulfidation into Au-amorphous Ag<sub>2</sub>S core-shell NP (S3). The amorphous Ag<sub>2</sub>S layer then served as a sacrificial template in the following cation exchange process (S4-S6), transforming into crystalline Au-CdS core-shell NP. Based on cation exchange and anion exchange, they further demonstrated that their technique can be used to make more complex multicomponent nanostructures with precise structural and compositional tailoring. As shown in **Figure 1.5d**, multiple monocrystalline cation species or anion species within the shell can be achieved through controlled chemical reactions. In this approach, the amorphous to crystalline transformation is critical to allow the reorganization of heterointerface according to thermodynamic preference. Recently, Liu et al reported a DNA origami-silica nanostructure with greatly enhanced nanomechanical properties and structure tunabilities.<sup>40</sup> They first employed molecular dynamic simulations to optimize the chemical interaction between DNA backbone and silica precursor, and then amorphous silica clusters occur before silicification took place. By this approach, they can precisely engineer the

DNA origami-silica nanostructure at accuracy of sub-100 nm<sup>2</sup> pore. Moreover, complex DNA origami-silica nanostructures from two dimensional to three dimensional with various geometries can be prepared with this method.

### 1.4.3 Total synthesis

The concept of total synthesis is first used in organic chemistry, describing the complete chemical synthesis of a complex molecule, often a natural product. Organic chemists approach the synthesis of complex organic molecules by identifying simpler molecules that can be modified rationally or linked together by sequentially applying a set of known chemical reactions.<sup>8, 41</sup> Colloidal multicomponent NPs can be considered as a solid-state analogue of molecules, by assembling single component NPs with high site-specificity and structural order. Based on this idea, Buck et al. developed a total-synthesis framework for complex colloidal multicomponent NPs by merging strategies from molecular organic synthesis.<sup>8</sup> As shown in **Figure 1.6a**, a colloidal Fe<sub>3</sub>O<sub>4</sub>-noble metal hybrid NP model was employed, while M-Pt-Fe<sub>3</sub>O<sub>4</sub> (M=Au, Ag, Ni, Pd) trimer nanostructures were obtained as product with 100% yield. In **Figure 1.6i to l**, a series of control experiments investigating the chemoselective nucleation of Ag on Fe<sub>3</sub>O<sub>4</sub> NPs, Pt NPs, mixture of Fe<sub>3</sub>O<sub>4</sub> and Pt NPs and Pt-Fe<sub>3</sub>O<sub>4</sub> NPs show that nucleation of Ag can occur on both Fe<sub>3</sub>O<sub>4</sub> and Pt NPs except that it selectively nucleated on the Pt component of a Pt-Fe<sub>3</sub>O<sub>4</sub> hybrid NP. It indicates that Pt-Fe<sub>3</sub>O<sub>4</sub> hybrid NP have significantly different reactivity towards the nucleation of Ag than isolated Pt and Fe<sub>3</sub>O<sub>4</sub> NPs, which can be considered as a NP analogue of regioselectivity in organic molecular systems, in which several products with different spatial arrangements of functional domains are possible, but only one product is observed.<sup>8</sup> Another example of borrowing ideas from organic



chemistry to colloidal multicomponent synthesis is the introduction of protecting group. Hodges et al. described a solid state protection group in ternary hybrid NP isomers.<sup>9</sup> As shown in **Figure 1.6m**, the nucleation of Ag occurred on the Pt domain of Pt-Fe<sub>3</sub>O<sub>4</sub> hybrid NP (**Figure 1.6n**), while it happened on the Fe<sub>3</sub>O<sub>4</sub> domain of Pt-Fe<sub>3</sub>O<sub>4</sub> hybrid with a thin layer of Fe<sub>3</sub>O<sub>4</sub> on the Pt NP as protecting group (**Figure 1.6o**). Similar results are obtained for the Au-Pt-Fe<sub>3</sub>O<sub>4</sub> system, where formation of the favored Au-Pt-Fe<sub>3</sub>O<sub>4</sub> configuration is blocked by the Fe<sub>3</sub>O<sub>4</sub> protecting group.

#### 1.4.4 Polymeric surface engineering

Symmetry and site specificity control of the growth phase on a performed heterogeneous seed is a fundamental issue in multicompetent synthesis. Certain nucleation site is often favored by thermodynamics as described in last paragraph; however, such process is in many case lack of tunability. Thus the introduction of ligands to modulate the surface property of the primary structures (seeds) was developed. Lee et al. developed a salt concentration-mediated directional growth of Ag onto DNA-modified AuNPs, achieving highly efficient symmetry control.<sup>10,</sup>

<sup>42</sup> As shown in **Figure 1.7a**, the Ag shell can be continuously tuned from isotropic core-shell to anisotropic head-body by simply altering the salt concentration in the growth solution, which allowed the graduate change of nanostructure and optical properties (**Figure 1.7b**). The possible mechanism was illustrated in **Figure 1.7c**. DNA chains are known to have strong negative charge, which decreases with the increase of salt concentration. Therefore, the DNA was less charged and less protective at high salt concentration, and supporting multiple nucleation and core-shell growth of Ag. In contrast, the DNA chains strongly protect the Au NP surface against the Ag-PVP precursor at a low salt

concentration, which gave rise to a single nucleation of Ag and its anisotropic growth.

Recently, Wang et al. reported a ligand patch-based strategy for the highly selective and tunable protection of Au NR surface.<sup>11</sup> They demonstrated that polymer shells on Au NRs can undergo different modes of shell transformation, allowing them to act as versatile synthetic handles beyond facet control. In their method, Au NRs were first mixed with the amphiphilic polystyrene-block-poly(acrylic acid) (PSPAA) polymer and a hydrophobic ligand (as shown in **Figure 1.7e**) in dimethyl formamide (DMF)/water mixture before heating to assemble the core-shell ((Au NR-ligand)@PSPAA structure. Interestingly, after switching the solvent to water, simple heating can transform the resulting PSPAA shells in different modes (contraction, bimodal contraction, dissociation, and winding), depending on the choice of ligand and their concentration in the initial encapsulation step (**Figure 1.7f**).<sup>11</sup> Such polymeric shell as transformable mask greatly enhances the site specificity in multicomponent synthesis beyond facet selectivity, allowing the subsequent fabrication of more completed multicomponent nanostructures with unprecedented tunability. This new synthetic approach can inspire many further exploitation of the pliable polymer masks, which can bring about a leap forward in sophisticated nanosynthesis.

## **1.5 Plasmonic enhancement of multicomponent nanostructures**

### **1.5.1. Mechanism of plasmonic enhancement**

The plasmonic enhancement in hot electron-mediated chemical reactions is attributed to (i) the heating effect, where the surface plasmons decay through heat generation, (ii) the direct capture of hot electrons from the plasmonic

nanostructure surface by organic molecules to induce chemical reactions, and (iii) the electron-hole pair separation, where the plasmon-induced hot electrons jump across the Schottky barrier and inject into the semiconductor CB, generating a reduction potential for chemical reactions. Both heat release and hot electron generation occur by non-radiative plasmon decay, where the plasmonic nanostructures act as photothermal or photoelectric converters.

The generation of heat usually positively contributes to chemical reactions, because higher temperature increases the reactivity. Generally, chemical reactions can be accelerated through both plasmonic photocatalysis and photothermal heating of plasmonic nanostructures. It was widely believed that the plasmon-induced hot electrons of the metal catalyst were responsible for the high yields, having a higher energy than the normal electrons and therefore being easier to inject into organic molecules to break the chemical bonds.<sup>43</sup> However, the individual roles of the heating and hot electron effects were previously under debate, since these two effects are usually entangled. Recently, Huang et al. experimentally proved that hot electrons sometimes negatively affect plasmon-induced organic synthesis.<sup>44</sup> Based on atomic-level control of the Pd shell thickness on Au NRs, the authors successfully clarified the role of these two effects in catalytic performance, and maximized the catalytic efficiency via delicate material design. This new understanding provides material design guidelines for other types of reactions, where the plasmonic hot electrons can achieve positive contributions.

The hot electrons generated by surface plasmon decay can be readily coupled to chemical reactions. The efficiency of direct hot electron transfer is relatively low because of the short lifetime of hot electrons, which undergo degradation via

various energy relaxation processes. Therefore, only molecules located close enough to the plasmonic nanostructure can capture hot electrons and couple them into reactions.

The metal-semiconductor nanostructure is currently one of the most promising photocatalysts that can extend the utilization of solar energy from UV to visible and NIR regions. Based on plasmon-induced hot electron injection and the presence of the Schottky barrier, electron-hole pairs can be efficiently separated to obtain a metal anode and a semiconductor cathode. According to their band gap structures, this electrical energy can be used to accelerate some important chemical reactions, including hydrogen generation.

### **1.5.2 Role of the electromagnetic (EM) field**

Metal nanostructures as plasmonic antennas can convert optical radiation into intense localized EM fields by light-driven collective oscillations of electron plasma in the metal.<sup>45</sup> Over the past few years, researchers have found that the photocurrent generated by hot electron injection from plasmonic nanostructures into metal oxide Schottky barriers was substantially lower than that in conventional photoexcited solar cells.

To solve this problem, much effort has been dedicated to understanding the hot electron conversion process and developing new technologies to improve quantum efficiency. Mubeen et al. designed a plasmonic solar water splitter with a nanostructured plasmonic antenna, showing a largely enhanced quantum efficiency compared to previous plasmonic conversion systems.<sup>12</sup> As shown in **Figure 1.8a**, their design featured aligned Au NR arrays, a Pt nanoparticle-decorated TiO<sub>2</sub> layer on top of the Au NRs, and a cobalt-based oxygen evolution catalyst (Co-OEC). Under UV-dominated illumination (310 nm

$< \lambda < 520$  nm), the hydrogen generation rate was much lower than those obtained for the visible range ( $\lambda > 410$  nm and  $\lambda > 600$  nm), indicating the minor contribution of conventional electron-hole pair separation (**Figure 1.8b**). The authors demonstrated that all charge carriers originated from the surface plasmons of the Au NR array, and the strong dependence of the LSPR wavelength of the nanostructured substrate (**Figure 1.8c**), indicating the possibility of extending light conversion over the entire solar spectrum using an appropriately designed plasmonic nanostructure. Compared with plain metal substrates, the NR array platform in Figure 5a provides a relatively “rough” metal-semiconductor interface, where strong EM fields can be localized at the interface. The theoretical analysis of wavefunction and EM field enhancement effects on the quantum efficiency in a Au NR/TiO<sub>2</sub> system was conducted by Kumarasinghe et al.<sup>46</sup> Using the same model as in **Figure 1.8d**, they calculated the effect of EM field enhancement in an aligned Ag NR on the efficiency of hot electron injection into a TiO<sub>2</sub> substrate.<sup>46</sup> At constant volume, the hot electron injection (**Figure 1.8e**) is highly dependent on the EM field enhancement factor (**Figure 1.8f**), which increases with the NR aspect ratio. This indicates that the number of hot electrons able to cross the Schottky barrier increases in NRs with strong EM fields.

The strong relationship between surface plasmon polaritons (SPPs) and the hot electron injection efficiency was experimentally proved by Giugni et al., employing an aligned Au taper cone on top of a semiconductor (**Figure 1.8g**).<sup>14</sup> It is well-known that a tapered structure is an efficient wave guide that directs and confines SPPs to the tip, generating a strongly localized EM field (**Figure 1.8h**). Due to the near-field localization effect, the SPP to hot electron conversion rate in this device was above 30%, suggesting the critical role of SPP and EM field

confinement in hot electron utilization. These findings also stress that the intensity and distribution of plasmon-induced EM fields should be a major consideration in the design of plasmonic semiconductor devices. Plasmonic nanostructures capable of generating strong EM fields at the metal-semiconductor interface can greatly boost the hot electron generation efficiency, thus leading to a high conversion rate. Since EM field enhancement can be calculated by a computer, it can provide highly valuable information for the design of plasmonic materials with optimized catalytic properties.

### 1.5.3 Hot electron-driven surface-catalyzed chemical reactions

Hot electrons arising from the surface plasmon decay have high kinetic energy to overcome the reaction barrier, and can be directly transferred to an unoccupied energy level in the adjacent electron acceptor for some surface catalytic reactions. Fang et al. firstly reported the experimental and theoretical evidence of local surface plasmons-driven catalytic reaction by using para-aminothiophenol (pATP) (**Figure 1.9a and b**).<sup>15</sup> With a evidence from the time-dependent surface-enhanced Raman scattering (SERS) spectra of pATP, the p,p'-dimercaptoazobenzene (DMAB, Figure 8a) was produced from pATP by selective catalytic coupling reaction on silver nanoparticles. Heretofore, the three strongly enhanced Raman peaks of pATP at 1143, 1390, and 1432  $\text{cm}^{-1}$  were firstly interpreted and considered as experimental evidence for a chemical mechanism of SERS by Osawa in 1994.<sup>47</sup> With the direct experimental and theoretical evidence from SERS, however, Fang et al. found that the vibrational modes at 1390 and 1432  $\text{cm}^{-1}$  are the  $\nu_{\text{NN}}$  as well as symmetric  $\nu_{\text{CC}}$  vibrations, which means the formation of DMAB from pATP via the -N=N- bond.<sup>15</sup> Generally, SERS has been considered as a noninvasive technique, however, this

foresight confirmed that SERS cannot always provide the vibrational fingerprint information of original surface species under certain conditions. Since 2010, various kinds of experimental and theoretical results have been supported the production of DMAB from pATP by plasmon-driven surface-catalyzed chemical reactions.<sup>16-17, 48-53</sup> Later, it has been also reported that DMAB can be formed from aromatic nitro compounds on the plasmonic nanostructures through the hot electron-assisted surface-catalyzed chemical reactions.<sup>54-67</sup>

Although the possibility of production of azobenzene species from aromatic nitro and amine compounds has been reported, the reaction mechanism was not clear. Zhao et al. proposed the selective formation of azobenzene derivatives from para-substituted nitrobenzene and aniline using photoinduced charge transfer model based on time-dependent density functional theory (TD-DFT) methods (**Figure 1.9c**).<sup>16</sup> Based on photoinduced surface catalytic coupling reactions, the TD-DFT calculations showed that the initial reaction occurs through the electron transfer from silver to the LUMO of the absorbed  $-\text{NO}_2$  group, and from the highest occupied molecular orbital (HOMO) of the absorbed  $-\text{NH}_2$  group to the unoccupied level of silver under visible-light irradiation. Subsequently, the para-substituted  $-\text{NO}_2^-$  and  $-\text{NH}_2^-$  surface species react to form azobenzene derivatives. Xu et al. reported the mechanistic understanding of surface plasmon assisted catalysis (SPAC) reactions of pATP to and back from DMAB on a single silver microsphere under an atmosphere with both  $\text{O}_2$  and  $\text{H}_2\text{O}$  vapor (**Figure 1.9d**).<sup>17</sup> The pATP was converted into DMAB by energy transfer (plasmonic heating) process from surface plasmon resonance to the surface adsorbed pATP. Under this condition,  $\text{O}_2$  which acts as an electron acceptor was essential for the conversion reaction and  $\text{H}_2\text{O}$  which plays the role of a deprotonation agent could

accelerate the reaction. With a help of H<sub>2</sub>O which acts as the hydrogen source, on the other hand, hot electron promoted the reverse reaction (conversion of DMAB to pATP).

## **1.6 Hot electron-driven water splitting reactions**

### **1.6.1 Photocatalysis based on metal-semiconductor nanostructures**

Since Tian et al. found that charge separation can be achieved in metal-semiconductor nanostructures under visible illumination,<sup>68-69</sup> the “hot electron effect” that plasmon-induced energetic electrons can transfer to adjacent electron acceptors, has been intensively studied. Especially, the hot electron injection from metal to semiconductor has become a unique pathway to realize charge separation at visible and near-infrared (NIR) region, which is of particular importance in energy applications. Although the efficiency of hot electron effect is still low, it is comparable to the early values of semiconductor-based photocatalysis when Honda-Fujishima effect was first found.<sup>70</sup>

### **1.6.2 Effects of plasmonic nanostructure geometry**

The LSPR and EM field enhancement of plasmonic nanostructures is highly dependent on their geometry. Sharp corners, tips, or gaps could induce significantly stronger EM fields that are typically referred to as ‘hot spots’.<sup>71</sup> Among the various plasmonic metals, gold is the most widely studied one for hot electron-mediated energy conversion. Previously, larger particles were found to usually exhibit higher quantum efficiencies in photocatalysis. Qian et al. fabricated Au-TiO<sub>2</sub> heterostructures with AuNPs of different sizes, applying deposition-precipitation and photodeposition methods to commercial P25 TiO<sub>2</sub>.<sup>72</sup> The authors compared the hot electron conversion efficiency of 4.4-nm AuNPs with that of 67-nm AuNPs under  $\lambda > 435$  nm illumination. Both 4.4-nm and



67-nm AuNPs could induce the photodeposition of Pt nanoparticles on TiO<sub>2</sub> under illumination; however, only 67-nm AuNPs could induce hydrogen generation under identical conditions. It was therefore concluded that both small and large AuNPs can support hot electron transfer, albeit with different transfer rates. The accumulation of transferred hot electrons in the CB of TiO<sub>2</sub> results in a different energy level, which changes their chemical reduction potential. The authors have further shown that the reduction potential of the transferred electrons can be easily tuned by varying the Au NP size, providing a simple means of tailoring their photocatalytic activity.

Regarding the effect of shape, anisotropic AuNPs such as rods, cubes and stars often exhibit higher LSPR absorption than spherical AuNPs. Sousa-Castillo et al. compared gold nanospheres, NRs and nanostars in Au-TiO<sub>2</sub> nanostructures, both experimentally and theoretically.<sup>73</sup> Both results showed that the catalytic efficiency of these architectures strongly depends on the EM field enhancement of the plasmonic components, which was proportional to their anisotropy degree. Among the shapes studied, Au nanostars exhibited the most intensive local fields around their spikes, thus leading to the highest photocatalytic performance. The strong correlation between the EM field from anisotropic NPs and the enhanced catalytic performance was also supported by observations on Pd concave NPs,<sup>74</sup> Au nano-dimer<sup>75</sup> and Au/AuAg/Ag<sub>2</sub>S/PbS NRs.<sup>76</sup>

### **1.6.3 Effects of metal-semiconductor configuration**

Due to the special nature of hot electron injection, the metal-semiconductor interface plays a more critical role than other nanostructure components. The effect of metal-semiconductor configuration can be mainly attributed to the charge balance or EM field enhancement. Anisotropic metal-semiconductor

nanostructures have been experimentally demonstrated to show a strong catalytic effect, while the metal@semiconductor nanostructure was basically invalid. Recently, Wu et al. developed an Au NR-TiO<sub>2</sub> photocatalyst, with TiO<sub>2</sub> specifically deposited on the tips of Au NRs.<sup>18</sup> As shown in **Figure 1.10**, the as-synthesized Au NR-TiO<sub>2</sub> photocatalyst showed a spatially separated dumbbell structure (**Figure 1.10a-h**), with TiO<sub>2</sub> acting as a filter for hot electrons from Au NRs. **Figure 1.10i and j** compare the catalytic performance of Au NR@TiO<sub>2</sub>, Au NRs/TiO<sub>2</sub> mixture, and TiO<sub>2</sub>-tipped Au NR in both hydrogen generation and the photoreduction of methylene blue. Since the core-shell structure did not show catalytic activity in both cases, it was proposed that restoring the charge balance of the Au core through oxidation reactions on the bare portions of Au NRs is necessary for the reaction to proceed (**Figure 1.10k and l**). The TiO<sub>2</sub> located at the tips of Au NRs generated a concentrated EM field that focused the energy flux around the heterointerface, thus enhancing hot electron generation and photocatalytic activity.

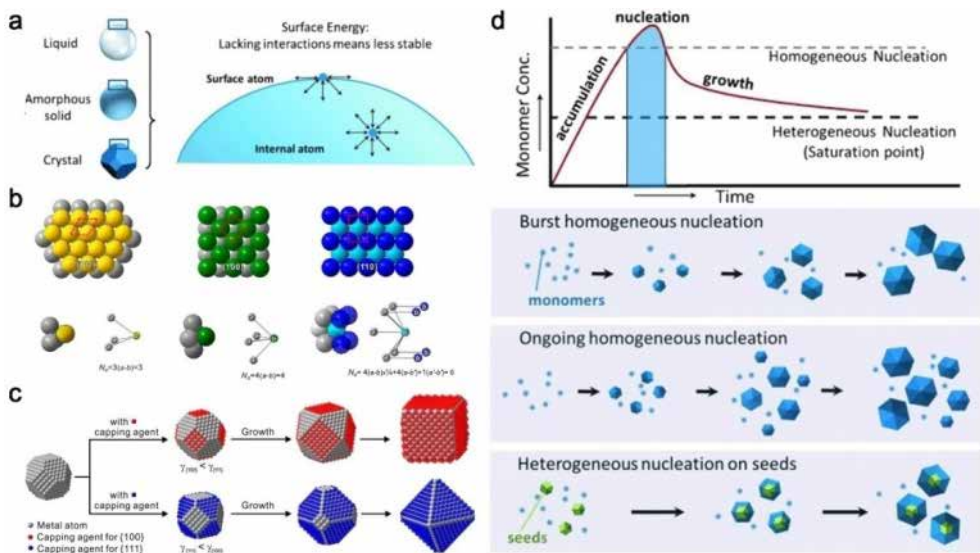


**Figure 1.1.** (a) The essence of surface energy: Minimizing the energy of the system requires minimizing the number of the surface atoms with unfavorable interactions. (b) Models of the three major low-index planes (111, 100 and 110) in a fcc metal and the corresponding numbers of bonds per surface unit cell. (c) Schematic illustration of the role of capping agents in directing the growth of a single-crystal seed. (d) LaMer plot describing the nucleation and growth process of monodisperse NPs.<sup>1-2</sup>

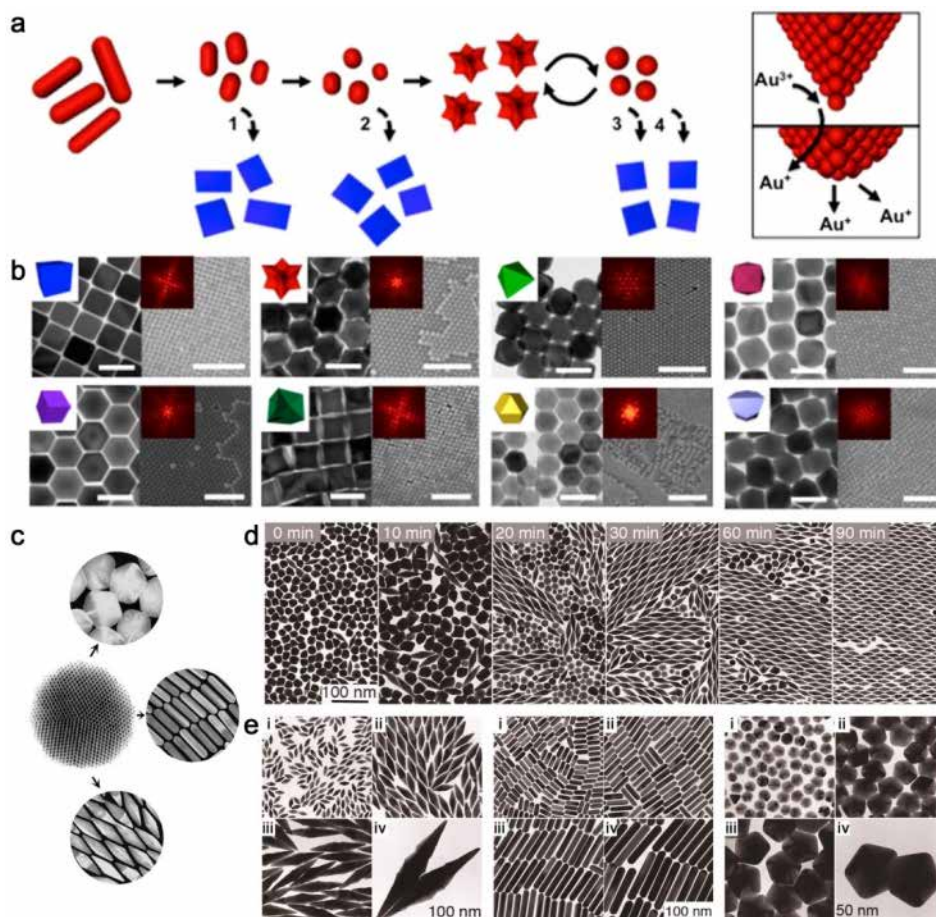


**Figure 1.2.** (a) Schematic illustration of the iterative and cyclical process of reductive growth and oxidative dissolution for the synthesis of high-quality single crystalline Au seeds. (b) High quality single-crystalline gold nanostructures by using single crystalline seeds after iterative and cyclical process.<sup>3</sup> (c) Monodisperse bipyramids, NRs, and decahedra from high-quality pentatwinned seeds. (d) TEM images of samples prepared using seeds at different heating times. (e) High quality pentatwinned gold nanostructures by using pentatwinned gold seeds after thermal process.<sup>4</sup>

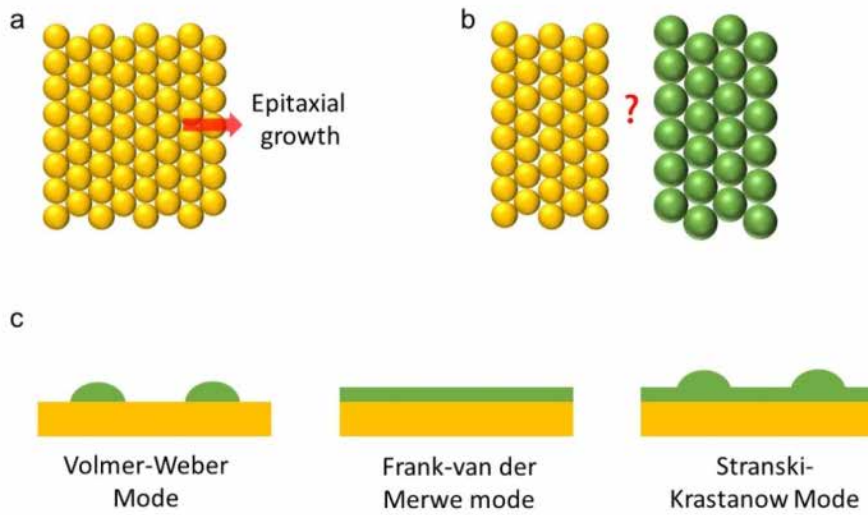


**Figure 1.3.** (a) In crystallized nanostructures, atom deposition is favored by epitaxial growth which follows the established lattice structures. (b) The heterointerface that directly bonded two materials is associated with the mismatch of lattice parameters. (c) Three types of growth mode at the heterointerface depending on the degree of lattice mismatch.

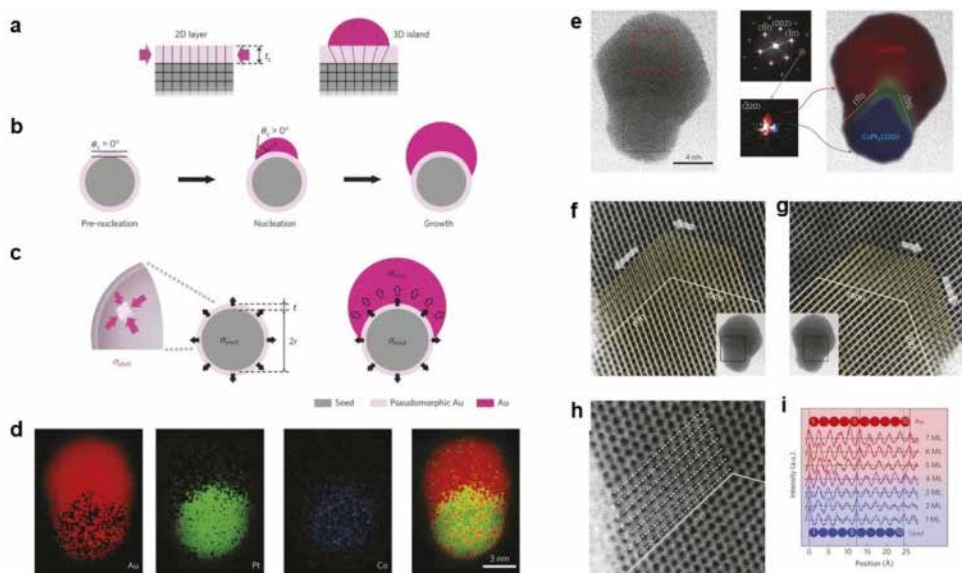


**Figure 1.4.** (a) Lattice structure of the overgrowth phase in the 2D and the 3D mode of the Stranski-Krastanov model. (b) Morphological evolution of the seed/Au heterostructure during the pre-nucleation, nucleation and growth periods. The contact angle  $\theta_c$  between the seed and the Au is indicated for the core/shell and the dumbbell. (c) Schematic illustration of the stresses,  $\sigma_{\text{shell}}$ ,  $\sigma_{\text{seed}}$  and  $\sigma_{\text{inter}}$ , within core/shell and dumbbell NPs. (d) STEM-EDX mapping of a CoPt<sub>3</sub>/Au dumbbell. (e) Atomic-resolution annular bright-field STEM image of a CoPt<sub>3</sub>/Au dumbbell and the corresponding FFT image overlapped with those from the seed (blue) and Au (red) domains. (f, g) Magnified images of the area indicated in the insets. Yellow straight lines are extensions of the seed lattice. The direction of the displacement of the lattice planes (white) with respect to the seed lattice (yellow) is indicated with arrows. (h) Magnified image showing 7 adjacent monolayers over the (111) interface and (i) intensity profiles along the dashed lines in the image.<sup>5</sup>

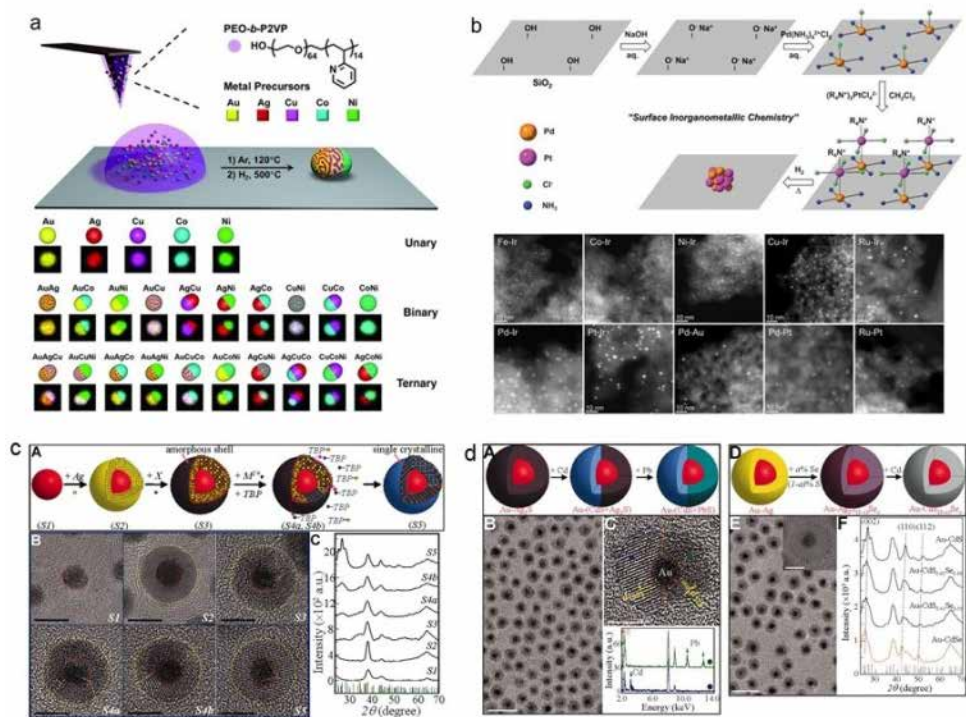


**Figure 1.5.** (a) The scanning-probe block copolymer lithography-mediated synthesis of multimetallic NPs and a polyelemental library of unary and multimetallic NPs made via this technique. (b) A schematic illustration of the surface inorganometallic chemistry for the synthesis of supported bimetallic NPs. The HAADF-STEM images of 10 types of supported bimetallic NPs synthesized by this approach. Scale bars are 10 nm.<sup>6</sup> (c) Schematic illustration of the no epitaxial growth process of hybrid core-shell nanostructures, as well as TEM images and XRD patterns of different synthetic stages. Scale bars are 5 nm. (d) Schematic illustration of the growth procedure of the Au-(CdS+PbS) NP with monocrystalline cation species within the shell (left) and Au-CdS<sub>1-a</sub>Se<sub>a</sub> NP with monocrystalline anion species within the shell (right). Scale bars are 5 nm.<sup>7</sup>



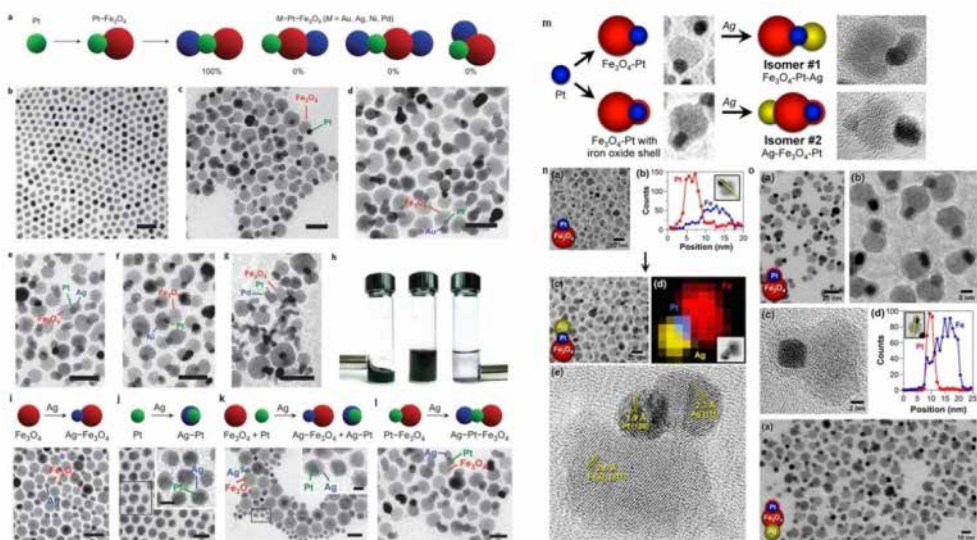


**Figure 1.6.** (a) Schematic illustration of the stepwise synthesis of M-Pt-Fe<sub>3</sub>O<sub>4</sub> heterotrimers (M=Ag, Au, Ni, Pd) as well as the possible NP products and their experimental yield. TEM images of Pt nanoparticle seeds (b), Pt-Fe<sub>3</sub>O<sub>4</sub> heterodimers (c) and Au-Pt-Fe<sub>3</sub>O<sub>4</sub> (d), Ag-Pt-Fe<sub>3</sub>O<sub>4</sub> (e), Ni-Pt-Fe<sub>3</sub>O<sub>4</sub> (f) and Pd-Pt-Fe<sub>3</sub>O<sub>4</sub> (g) heterotrimers. Scale bars are 25 nm. (h) Photographs of a vial that contains Au-Pt-Fe<sub>3</sub>O<sub>4</sub> heterotrimers in hexane with (left) and without (middle) external magnet, and after precipitation with ethanol (right).<sup>8</sup> TEM images and corresponding schematics as control experiments of Ag nucleation on: (i) Fe<sub>3</sub>O<sub>4</sub> NPs, (j) Pt NPs, (k) mixture of Fe<sub>3</sub>O<sub>4</sub> and Pt NPs, (l) Pt-Fe<sub>3</sub>O<sub>4</sub> NPs. Scale bars are 20 nm (main panel) and 5 nm (inset), respectively. (m) Schematic illustration of a solid state protection group in colloidal multicomponent synthesis. (n) Evidence of NP growth from Fe<sub>3</sub>O<sub>4</sub>-Pt NP to Fe<sub>3</sub>O<sub>4</sub>-Pt-Ag NP. (o) Evidence of NP growth from Fe<sub>3</sub>O<sub>4</sub>-Pt NP with iron oxide shell to Ag-Fe<sub>3</sub>O<sub>4</sub>-Pt NP.<sup>9</sup>



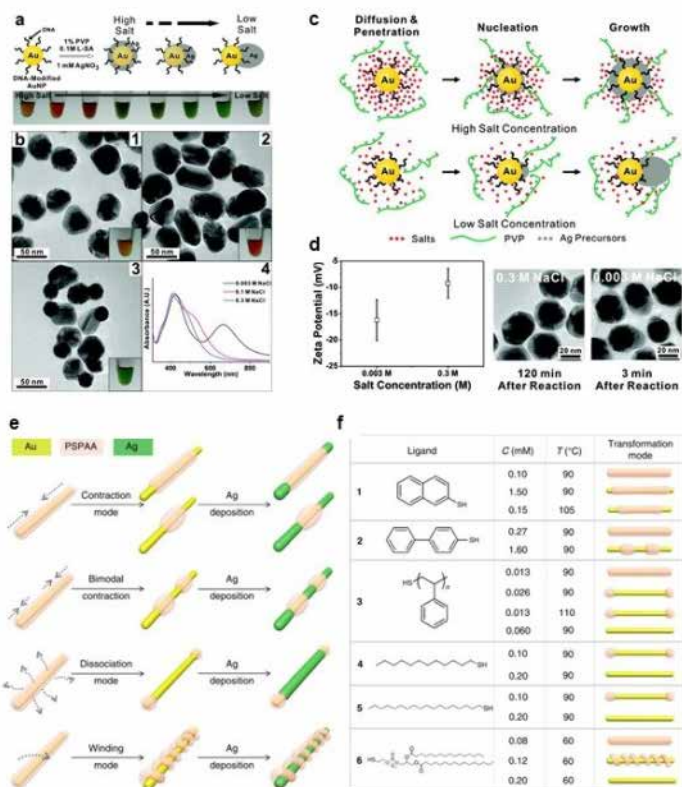


**Figure 1.7.** (a) Schematic illustration and solution color of Au-Ag hybrid NPs from Ag nucleation on DNA modified Au NPs with varying salt concentration. (b) TEM images of NPs synthesized at salt concentrations of (1) 0.3, (2) 0.1, and (3) 0.003 M and (4) the corresponding UV-vis spectra. (c) Proposed reaction mechanism at different salt concentrations. (d) Zeta potentials for DNA-AuNPs at 0.003 and 0.3 M salt concentration (left); HRTEM images of Ag nanostructure formation on DNA-AuNPs at intermediate stages (right).<sup>10</sup> (e) Schematic illustration of the four transformation modes of (Au NR-ligand)@PSPAA: contraction, bimodal contraction, dissociation, and winding modes. (f) The ligand dependence is summarized in the table.<sup>11</sup>

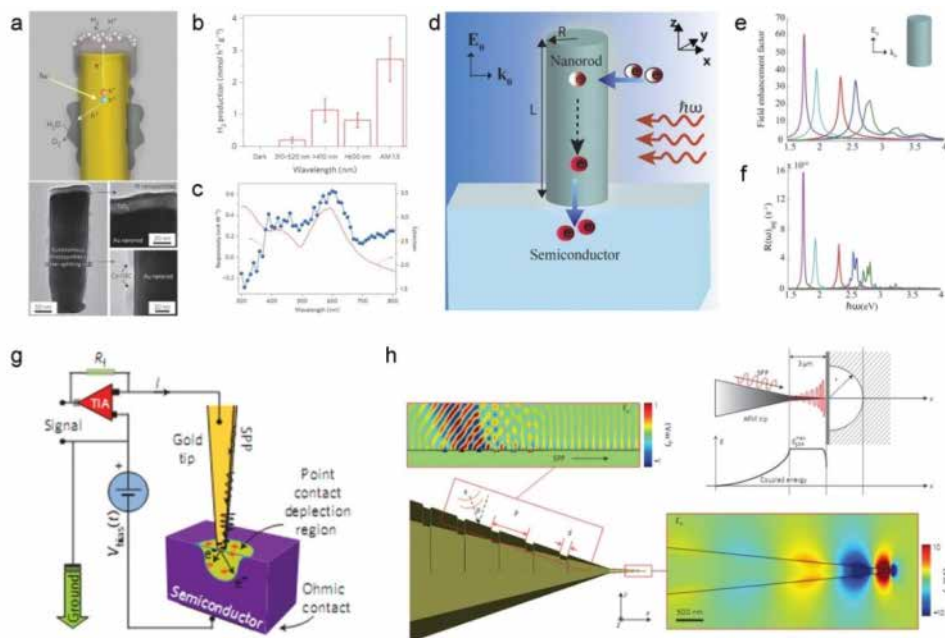


**Figure 1.8.** (a) Schematic and corresponding TEM of an individual photosynthetic unit showing the inner Au NR, the TiO<sub>2</sub> cap decorated with Pt NPs, and the Co-OEC material deposited on the lower portion of the Au NR. (b) Hydrogen produced per hour with various illumination wavelengths. (c) At visible wavelengths, the responsivity of the Au NR/TiO<sub>2</sub>/platinum plasmonic photocathode (line and symbols) tracks the extinction spectrum of the device (red line) faithfully.<sup>12</sup> (d) Scheme of a calculation model consisted of an Ag NR vertically posited on the TiO<sub>2</sub> substrate. (e) The electron injection efficiency and (f) quantum efficiency of the Ag NRs of different aspect ratios.<sup>13</sup> (g) Gold taper used to adiabatically compress a surface plasmon polariton (SPP) into the Au/Si Schottky junction. (h) Geometry of the Au taper that guide the SPP to the tip junction of Au/GaAs interface where strong EM field was localized.<sup>14</sup>

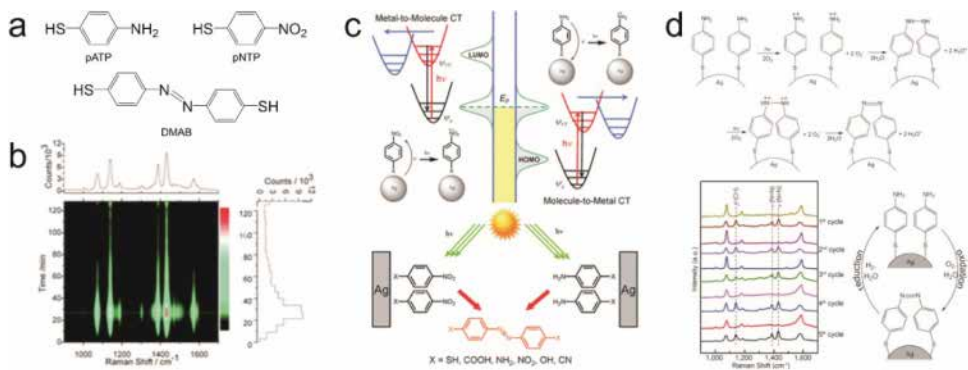


**Figure 1.9.** (a) Chemical structures of pATP (left), pNTP (right), and DMAB (bottom). (b) The time-dependent SERS spectra of DMAB produced from pATP by selective catalytic coupling reaction on silver nanoparticles.<sup>15</sup> (c) Schematic diagram of the photoinduced charge transfer process for nitro and amine functional group on silver surfaces.<sup>16</sup> (d) Proposed SPAC mechanism of conversion process from pATP to DMAB under an atmosphere with both O<sub>2</sub> and H<sub>2</sub>O vapor (upper panel).<sup>17</sup>

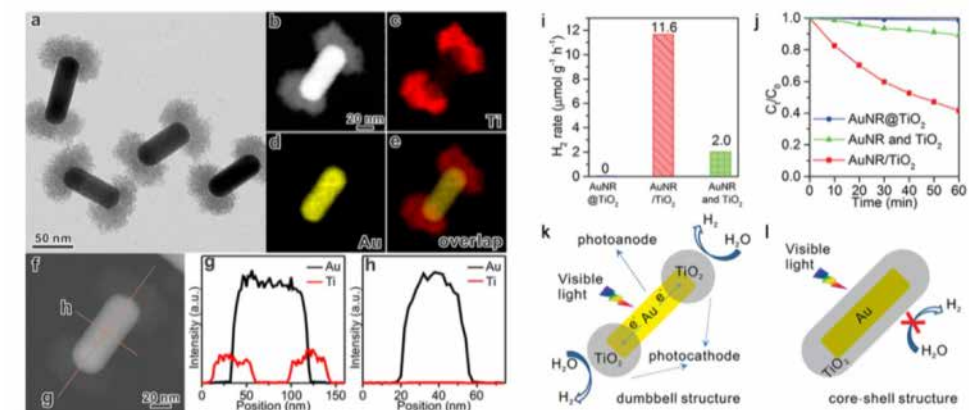


**Figure 1.10.** (a) TEM image, (b-e) HAADF-STEM image and elemental maps, and (f-h) elemental profiles of Au NR/TiO<sub>2</sub> dumbbells. (i) Comparison of hydrogen generation rate by various catalysts. (j) Normalized concentration of methylene blue at different irradiation time. Structure and mechanism of operation under visible light of (k) an individual Au NR/TiO<sub>2</sub> dumbbell and (l) core/shell Au NR@TiO<sub>2</sub>.<sup>18</sup>

# Chapter 2: Crystal Structure Engineering in Symmetry Breaking of Bimetallic Nanoparticles

## 2.1 Introduction

Precise compositional and structural tuning of multiple nanocomponents is a fundamental step in the design and fabrication of sophisticated nanostructures. Although various multi-component nanostructures have been synthesized by heterogeneous nucleation methods,<sup>5, 36-37</sup> growth symmetric and shape evolution of the secondary nanostructures remain challenging. Similar to chemical reactions of molecules, the wet-chemistry formation of nanocrystals in solutions is governed by the thermodynamic versus kinetic evolution on nanocrystal surface<sup>22, 77</sup>, except that nanocrystals are much more challenging to achieve a high purity with identify chemical and physical properties. For example, although spherical shape is usually thermodynamically preferred, the crystal structure and capping ligand difference in two spherical nanocrystals can have vastly different surface properties.

Compare to homogeneous nucleation, heterogeneous nucleation is often associated with more synthetic challenges and less structural tunability. The lattice strain energy emerges simultaneously with the formation of lattice-mismatched heterointerface<sup>5</sup>, which becomes an uncontrollable factor in the subsequent growth. To release the strain energy, defects will form through competing dislocation modes including twin and slip, which are very difficult to predict<sup>78-79</sup>. Once transient dislocation defects are formed, the surface energy distribution

(preferential growth direction) changes as well, leaving directional growth achieved in vain.

Heterogeneous catalysis that couples light into chemical reactions is of paramount importance in chemistry and energy applications<sup>80-81</sup>. The plasmonic enhancement is currently one of the hottest topics in catalysis-driven chemistry and optical materials due to its important role as the main mediator bridging the solar energy with multiple forms of energy. For instance, the photocatalytic water splitting reaction as biomimetic plant photosynthesis represents a promising solution to growing demands for clean and sustainable energy. Plasmon-enhanced photocatalysis has the great potential for overcoming many of the intrinsic limitations of conventional semiconductor photocatalysts, such as short range light response, low light absorption and high recombination rate of photogenerated carriers.

In this chapter, we engineered the crystal structure of two types of gold seeds to epitaxially grow symmetric and asymmetric gold-copper multicomponent nanostructures and used these structures to enhance and localize the electromagnetic field on particle surface. Copper-based nanostructures are especially promising as a next-generation metal nanostructure with respect to abundance, price, optical property and conductivity, but the synthesis of copper-based nanostructures that often requires harsh conditions is neither well understood nor controllable. This work shows that seed crystallinity can dictate the adopted dislocation mode of the growth material, and further affect their optical and catalytic properties.

## **2.2 Experimental section**

### **2.2.1 Materials and instruments**

All chemical reagents were purchased from Sigma-Aldrich except PEI (branched, MW=1,800, Polysciences) and used without further purification. The transmission electron microscopic (TEM) and Cs-corrected high resolution transmission electron microscopic (HRTEM) characterizations were performed with a JEM-2100F (JEOL) electron microscope and a JEM-ARM200F (JEOL) electron microscope, respectively. The energy-dispersive X-ray spectroscopy (EDX) mapping measurements were performed with a JEM-2100F electron microscope. The TEM and HRTEM specimens were prepared by dropping a few microliters of concentrated nanoparticle solution on a carbon-coated copper grid or a carbon-coated nickel grid (for EDX mapping) followed by drying in vacuum. Zeta-potential measurement was performed on a Zetasizer 3500 (Malvern Instruments) equipped with a He-Ne ion laser at a wavelength of 633 nm.

### **2.2.2 Synthesis of GSS**

Gold clusters (brown-colored solution) were made by rapidly adding a fresh ice-cold aqueous  $\text{NaBH}_4$  solution (10 mM , 0.6 mL) to a thoroughly mixed 10 mL aqueous solution containing  $\text{HAuCl}_4$  (0.25 mM) and CTAB (100 mM) under vigorous stirring (500 rpm) for 2 min. For the synthesis of ~9.5 nm nanoparticles, CTAC solution (200 mM , 2 mL), freshly-prepared ascorbic acid (AA) solution (100 mM , 1.5 mL) and the above CTAB-capped gold clusters (50  $\mu\text{L}$ ) were mixed in a 25 mL glass flask under mild stirring (80 rpm), followed by one-shot injection of an aqueous  $\text{HAuCl}_4$  solution (0.5 mM , 2 mL). The reaction was allowed to continue at 27 °C for 15 min before washing and centrifugation under 15,000 rpm (this procedure was repeated 3 times). The final particle concentration was diluted to 10 nM with 0.2 mM CTAC solution before use.

### **2.2.3 Synthesis of GTS**

Gold clusters (orange-colored solution) was made by rapidly adding a fresh ice-cold aqueous  $\text{NaBH}_4$  solution (100 mM, 0.6 mL) into a thoroughly mixed 20 mL aqueous solution containing  $\text{HAuCl}_4$  (0.25 mM) and trisodium citrate (0.25 mM) under vigorous stirring (500 rpm) for 2 min. To synthesize  $\sim 9.5$  nm nanoparticles, CTAB solution (200 mM, 4.5 mL),  $\text{HAuCl}_4$  solution (0.5 mM, 4.5 mL) and fresh prepared AA solution (100 mM, 50  $\mu\text{L}$ ) were mixed in a 25 mL glass flask under mild stirring (80 rpm), followed by one-shot injection of 1 mL of citrate-capped gold clusters. The reaction was allowed to continue at 25 °C for 15 min before washing and centrifugation under 15000 rpm (this procedure was repeated 3 times). The final particle concentration was diluted to 10 nM with 0.2 mM CTAC solution before use.

#### **2.2.4 Synthesis of 4-ABT-modified NPs**

Freshly synthesized GSSs or GTSs were redispersed in 20 mM CTAB solution to obtain a final concentration of 10 nM particle solutions. Freshly prepared 4-ABT solution (1 mM, 25  $\mu\text{L}$ ) was then added to 5 mL of GSS or GTS solution while stirring. The mixture was kept at 40°C for 3 h followed by washing and centrifugation. The final product was redispersed in 5 mL of 0.2 mM CTAC solution before use.

#### **2.2.5 Synthesis of GCCS and GCTT NPs**

In a typical synthesis, two identical growth solution compose of  $\text{CuCl}_2$  (0.1 M, 40  $\mu\text{L}$ ), PEI (1%, 80  $\mu\text{L}$ ) and AA (0.1 M, 500  $\mu\text{L}$ ) were mixed thoroughly. For GCCS NPs, 100  $\mu\text{L}$  of 10 nM GSS was one-shot injected into one of the growth solution and allowed to continue for 15 min at 40°C. For GCTT NPs, 100  $\mu\text{L}$  of 10 nM GTS was one-shot injected into another growth solution and allowed to continue for 15 min at 40°C.



## 2.3 Results and Discussion

### 2.3.1 Characterization of gold-copper nanoparticles

As shown in **Figure 2.1**, gold single-crystalline seeds (GSS) and gold icosahedral twin seeds (GTS) were used to generate spherical gold-copper core-shell (GCCS) and gold-copper tip-taper (GCTT) nanoparticles, respectively. Due to the presence of gold seeds as nucleation sites, the energy barrier for copper reduction was largely decreased. The reaction only takes 15 min under a mild temperature of 40 °C. Due to the slow kinetics and restrained reducing power, self-nucleation of copper is inhibited. Polyethyleneimine (PEI) coordinates to copper ions and gold seeds limit the free diffusion of copper precursors, which promotes the site specific reduction and deposition of copper atoms.

Cs-corrected high-resolution transmission electron microscopy (HRTEM) was used to investigate the atomic structure of nanoparticles. As shown in **Figure 2.2a**, single crystallinity was observed for GSS (**Figure 2.2a**) and the synthetic yields of GSSs was estimated to be >95 % (>200 particles were analyzed for each case). We then further investigate the lattice configurations of gold-copper multicomponent nanoparticles. **Figures 2.2b** and **c** show the GCCS NPs from GSS, displaying spherical core-shell structures. Fast Fourier-transform (FFT) converted HRTEM into reciprocal lattice pattern to extract lattice configuration with reduced background. In **Figures 2.2b** and **c**, the Cu shell of GCCS NPs shows consistent lattice structure and FFT pattern, exhibiting a face-centered cubic (fcc) structure enclosed by {200} facets. The FFT pattern of the core area (FFT c1) is consistent with the patterns from Cu shell regions (FFT b1, b2 and b3), indicating Cu shell grew epitaxially from the GSS with high lattice consistency. In addition, distinguishable slip planes were observed in the right part of the particle (**Figure**

**2.2c).** It should be noted that Au and Cu has a large lattice mismatch of 11.4 %, but GCS NPs showed only one or two dislocation defects in the Cu shell per particle. The high crystallinity of GCCS NPs should be attributed to the epitaxial growth from single crystalline gold seed and the mild reduction condition in synthetic protocol.

Importantly, twin-directed Cu nanostructure growth was observed in the GTS case and GCTT NPs exhibit anisotropic Au tip-Cu taper structures (**Figure 2.3**). The face-centered cubic (fcc) structured metallic nanocrystals usually have five-fold  $\langle 111 \rangle$  twins.<sup>3</sup> Starting from an fcc-structured tetrahedron, an icosahedron is assembled from 20 tetrahedrals with 6 axes (as shown in **Figure 2.3a**). An icosahedron has 12 twin vertices on the surface, which can be considered as 20 single-crystalline tetrahedral grains sharing their  $\langle 111 \rangle$  facets as twin boundaries (Figure S3a). In the case of a complete cyclic five-fold twin, the angle is  $2\pi/5=72^\circ$  while the theoretical angle between two  $\langle 111 \rangle$  planes is  $70.5^\circ$ , indicating a gap of  $7.5^\circ$  exists. This discrepancy leads to additional lattice strains at the grain boundaries, which results in a higher surface energy at the grain vertices and boundaries. The angle between two adjacent  $\langle 200 \rangle$  planes is  $108^\circ$ , and that between two non-adjacent  $\langle 200 \rangle$  planes is  $120^\circ$ .

As shown in **Figure 2.3a**, the presence of twin was clearly observed in two representative icosahedral twin gold nanoparticles, and the synthetic yields of GTSs was estimated to be  $>91\%$  ( $>200$  particles were analyzed for each case). The presence of twin on GTSs was found to effectively break the symmetric of gold-copper NPs. As described in **Figure 2.3b**, the copper domain selectively grew from one of the five-fold twin vertices and the diameter of copper body gradually increased to form a taper shape. Sharp boundaries in the growing end of the copper

body were observed under HRTEM (**Figure 2.3c, d**). **Figure 2.3d** shows a side view of a GCTT particle. The FFT (**inset of Figure 2.3c**) that corresponds to the selected tip area indicates a polycrystalline lattice structure. The magnified TEM image shows a copper body grew epitaxially from the one side of a GTS. Several regions with distinct contrast and lattice were observed within a copper body. FFT 2 shows three sets of  $\{220\}$  planes that correspond to a  $[111]$  zone axis, indicating the grain is perpendicular to the electron beam. FFT 1 and 3 show two sets of symmetric patterns, characteristic of a twin structure. The angle between  $\{200\}$  planes is  $120^\circ$ , and there is no shared  $\langle 111 \rangle$  facts, which strongly indicates that FFT 1 and 3 correspond to two nonadjacent grains in a five-fold twin.

We further confirmed the five-fold twin structure of GCTT NPs by HRTEM tilting. When electron beam was applied to the five-fold twin axis in parallel (**Figure 2.4a**), a decahedral twin end with five distinct domains were observed (**Figure 2.4b**). The corresponding FFT in **Figure 2.4c** shows an overlaid pattern from five symmetric grain domains with a shared zone axis of  $[110]$ , which indicates the growth direction along  $[110]$  direction. As described in **Figure 2.4d**, when the electron beam was tilted to have a small angle with the five-fold twin axis, multiple twin boundaries inside the copper body were observed by HRTEM in **Figure 2.4e**. It should be noted that the twin boundaries possess a different lattice phase<sup>82</sup> from the face-centered cubic (fcc) grains. The overlaid lattice of twin boundaries and the grains produced strong Moiré patterns along the twin structure. **Figure 2.4f** shows a magnified image at the twin edges. The twin boundaries exist throughout the copper body, and the copper body size gradually increases as it gets farther from the gold tip part. From the above analysis, we can conclude that a five-fold twin copper body in GCTT NP epitaxially grew from one side of a GTS.

The yields of GSSs, GTs, GCCS and GCTT were evaluated by TEM with >200 NPs for each sample. **Figure 2.2** shows the statistical analysis of crystal structure compositions of GTs and GSSs. The yield of GSSs was around 95.5 percent with minimum among of twin crystals. Regarding GCCS NPs, a core-shell cubic structure is an overwhelmingly major product (~95%) while core-shell rod and Janus structures were minor products (<5%). The yield of GTs was around 91 percent with 6.5 percent single-crystalline crystals and 2.5 percent singly-twinned crystals. Regarding GCTT NPs, the yield of a tip-taper structure was very high (>90 %), and core-shell cube and core-shell rod structures were found to be minor products. In addition, , it was experimentally found that poorly controlled seeds result in a mixture of different MAP structures. Such statistical and experimental results support that the yield of gold-copper NPs is highly related to the crystallinity of the initial seeds.

### **2.3.2 Mechanisms**

This crystal structure-mediated growth could be driven by the difference in gold-copper interfacial energies for gold single-crystalline seeds and gold twin seeds. Regarding gold single-crystalline seeds, copper grew under an epitaxial overcoating manner, which is known as the Frank-van der Merwe (FM) mode, resulting in atomically smooth, fully formed shells in GCCS NPs. In contrast, the epitaxial growth under the FM mode on gold twin seeds introduced multiple defective twin boundaries and unfavored interfacial energy, thus shifting to the Volmer-Weber (VW) mode.<sup>83</sup> In the VW mode, the interactions between the overgrowth atoms and the substrate surface atoms are lessened by the reduction of heterointerface. Copper alternatively grew from one edge of the gold twin seeds in an epitaxial twin fashion and led to a GCTT structure. Basically, the gold-copper

interface expands with the growth of the copper domain, but the formation of a heterointerface is restricted by the unfavored interfacial energy.<sup>84</sup> An anisotropic five-fold twinned copper taper body minimizes the gold-copper interface and the number of twin boundaries. As a result, the symmetry is broken for the inhibition of copper domain, and alternatively it results in the growth of an anisotropic five-fold twin copper structure.

### **2.3.3 Plasmonic and SERS properties**

Next, we used the gold-copper NPs to concentrate and enhance the electromagnetic field on a nanostructure. In particular, a taper-type structure can be a highly efficient plasmonic concentrator that guides and confines the localized surface plasmon resonance waves towards its tip<sup>45, 85</sup>. To study the electromagnetic field distribution, 3D finite-element method (3D FEM) (COMSOL, Stockholm, Sweden) was used. Both GCCS and GCTT NPs were modeled with a 10-nm gold spherical seed coupled with a copper shell (GCCS) or a copper taper (GCTT) (**Table 2.1**). The exposure ratio of gold seed in the GCTT was set to be 50 %. The incident wave used for plasmon excitation is linearly polarized along the x-axis.

The calculation result (**Figure 2.6**) shows that strong electromagnetic field was observed on the surface of a GCCS structure (7.8-fold stronger intensity than that of the incident light) was observed. Importantly, a highly localized, amplified electromagnetic field was found at the Au tip of a GCTT structure. The tip area exhibits a largely enhanced electromagnetic field (~32 -fold larger than that of the incident light). The surface area of the Au tip accounts for 13.6 % of the whole tip-taper structure, but the Au tip is responsible for 94.3 % of the SERS signal of the particle. The SERS enhancement of the Au tip is estimated to be ~8900-fold stronger than an Au NP without a Cu taper body. The surface integral of

electromagnetic field for the Au tip was calculated to be  $2.43 \times 10^{-15}$  V·m, which represented only 13.6 % of the overall surface integral. However, it represented 94.3 % of the SERS enhancement of the overall particle as calculated by E4-approximation.

Finally, we show that these particles can be used to facilitate and monitor chemical reactions with strong, controllable SERS properties of these particles. We modified Raman-active 4-aminobenzenethiol (4-ABT) to particles by Au-S bonds. **Figure 2.7** shows the TEM and UV spectra of GSSs, GTS, GCCS and GCTT before and after 4-ABT modification, respectively. The results indicated that these NPs remained stable in morphology and optical properties after the attachment of 4-ABT.

We then use the 4-ATP as probe to monitor the chemical reactions on these structures. As reported,<sup>86</sup> 4,4'-Dimercaptoazobenzene (4,4'-DMAB) can be photocatalytically generated from 4-ABT on gold surface and give rise to strong b2 peaks (ca. 1140, 1390 and 1432  $\text{cm}^{-1}$ ) in the SERS spectra upon completion of the reaction. Importantly, it was reported that this catalytic reaction is occurred specifically on Au surface (**Figure 2.8c**) but inhibited on Cu surface (**Figure 2.8a**).

<sup>87</sup> It should be noted that some of thiol molecules on Au surface can move to the growing Cu surface.<sup>88</sup> **Figure 2.8b** show the SERS spectra of 4-ABT-modified GSSs (black line) and 4-ABT-modified GCCS (red line), where large enhancement in SERS signal (~35-fold enhancement over 4-ABT on GSSs) was observed from 4-ABT-modified GCCS NPs. The SERS signals from 4-ABT-modified GSSs were remarkably weaker, and the characteristic b2 peaks were not found in the SERS spectrum, indicating the formation of copper shell can largely amplify the SERS signal. In **Figure 2.8d**, importantly, in the case of 4-ABT-modified GCTT

structure (red line), not only more than 60 times of SERS enhancement over the 4-ABT-modified GTSs (black line) was found, the characteristic Raman peaks of photosynthesized 4,4'-DMAB also occurs. The appearance of the 4,4'-DMAB peaks indicates the photo-oxidative coupling reactions of 4-ABT molecules was activated on the Au tip surface. The result confirms that Cu taper structure can be an efficient antenna structure that localizes and enhances the electromagnetic field on the Au tip of a GCTT structure. The addition of Cu taper part increases light scattering from particles and concentrated electromagnetic field on the Au tip activates the photochemical catalytic reaction and generates highly enhanced SERS signal.

## **2.4 Conclusion**

In summary, we showed that crystal structure engineering can be used in seed-mediated multicomponent synthesis of large lattice mismatched metal pairs, to correct the crystal structure in overgrowth materials, achieve symmetric breaking and new properties. We also show that these nanostructures can localize and enhance the electromagnetic field, and chemical species and reactions can be efficiently detected and photocatalyzed on gold-copper tip-taper nanostructures by the chemical and optical facilitation of the copper taper body for the gold tip. The strategies and results reported herein open revenues for crystal structure-based syntheses of multi-metal component nanostructures (in particular, earth-abundant, inexpensive Cu-based structures), SERS sensors and photocatalytic reactions on plasmonic nanostructures.

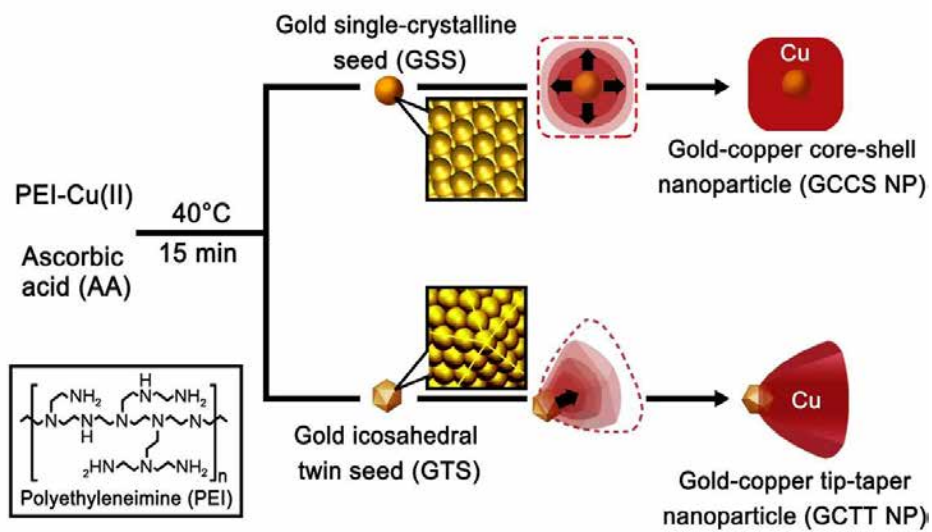


**Figure 2.1.** Schematic illustration of crystal structure-engineered gold seeds for symmetric breaking of gold-copper nanoparticles.



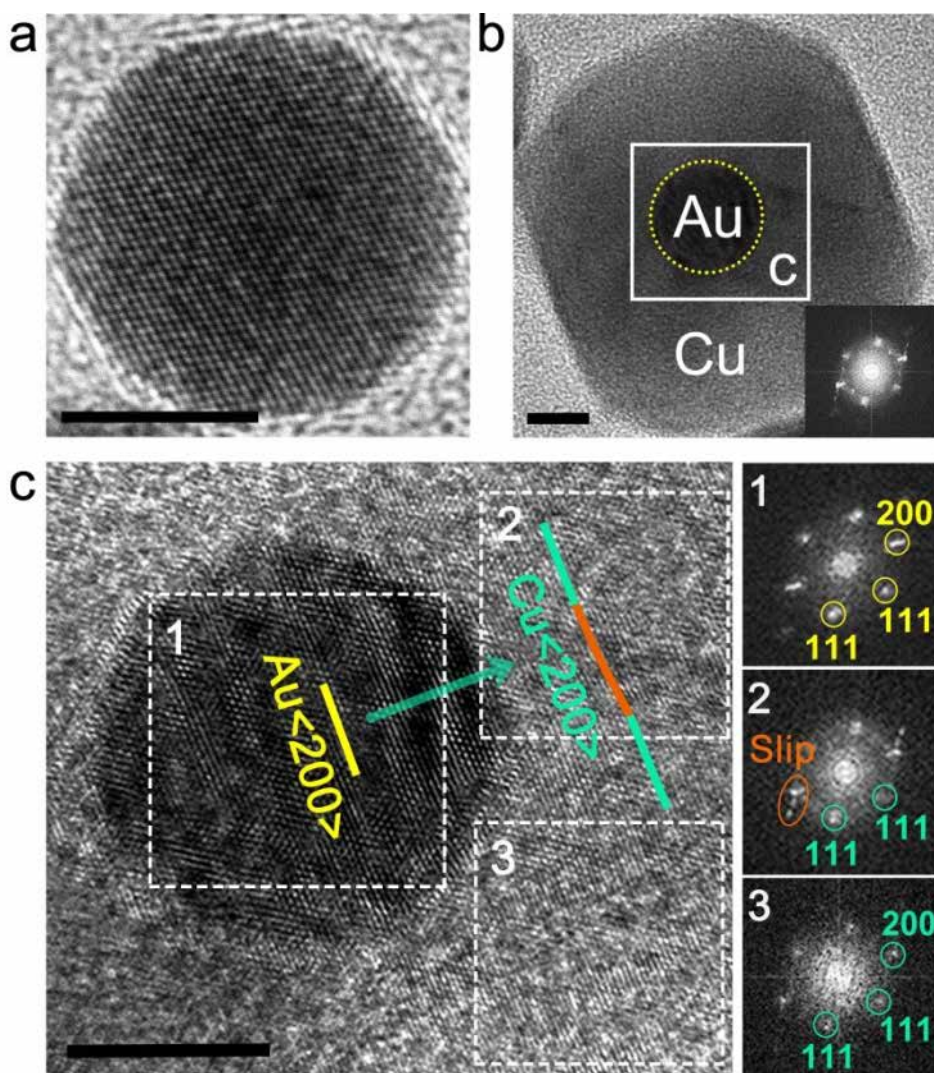


**Figure 2.2.** Cs-corrected high-resolution transmission electron microscopy (HRTEM) images of (a) a gold single-crystalline seed (GSS), (b, c) a gold-copper core-shell (GCCS) NP. Scale bars are 5 nm.

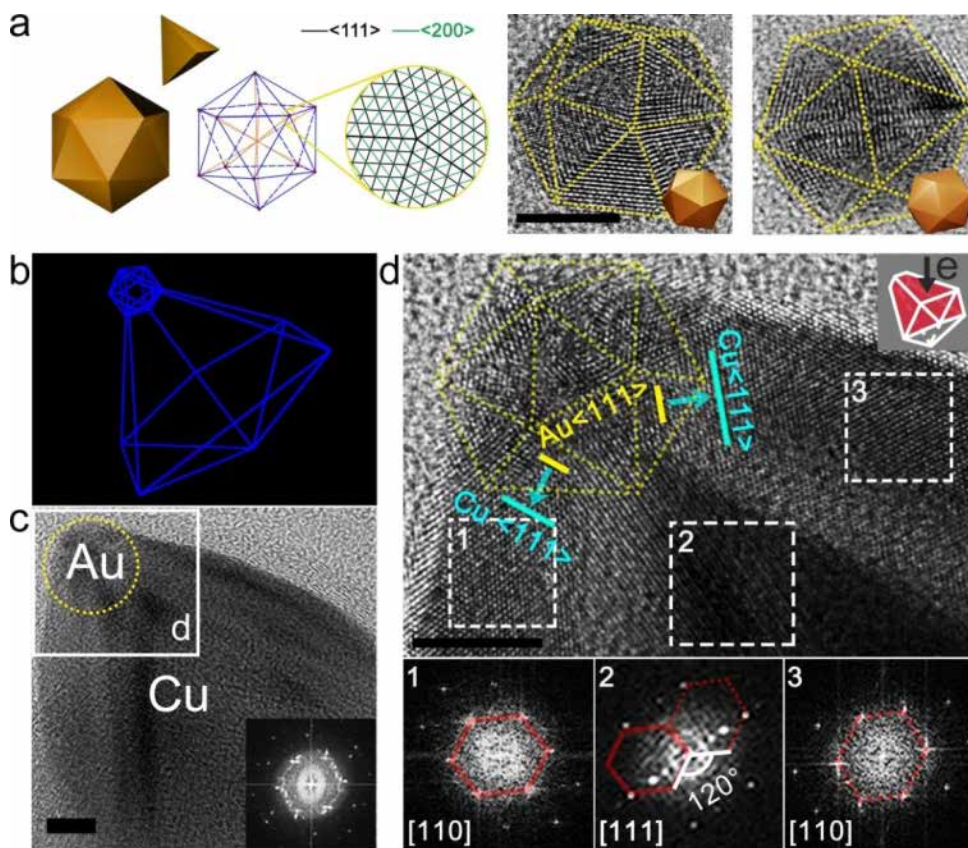


**Figure 2.3.** (a) Schematic illustration of icosahedral twin and HRTEM images of two representative gold icosahedral twin seeds (GTSS). (b) Schematic illustration of the twin structure in gold-copper tip-taper (GCTT) NP and (c, d) HRTEM characterization of a typical GCTT NP. For both GCCS and GCTT, identical growth conditions were used except the difference of gold seeds. Scale bars are 5 nm.

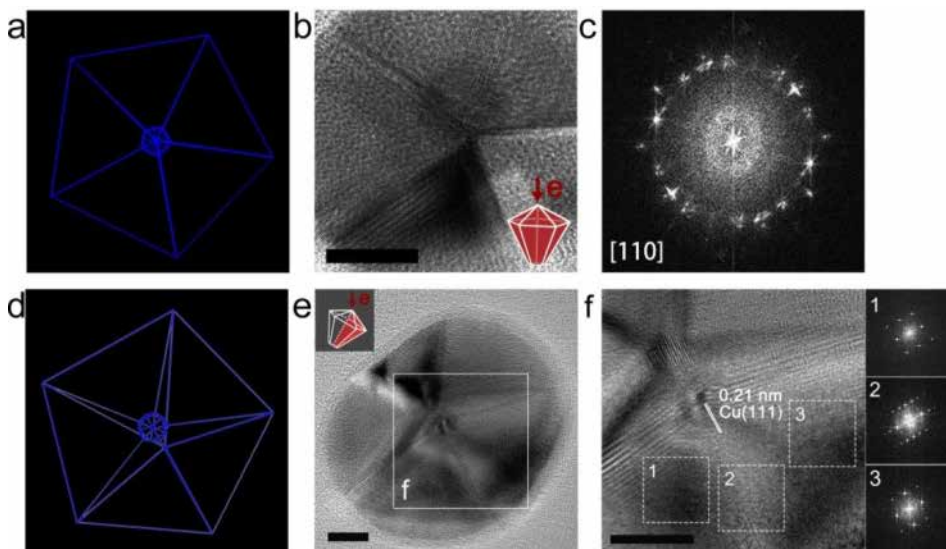


**Figure 2.4.** Schematic illustrations of icosahedral twin seed (a) and GCTT (b, c and f) structures at different orientations. Schemes b, c and f correspond to Figure 1g, S3d and S3g, respectively. (d) HRTEM and (e) corresponding FFT images of a GCTT NP when the electron beam was applied in parallel to the five-fold twin axis. (g, h) HRTEM images of a GCTT NP when the electron beam was applied with a small angle to the five-fold twin axis. Scale bars are 10 nm.

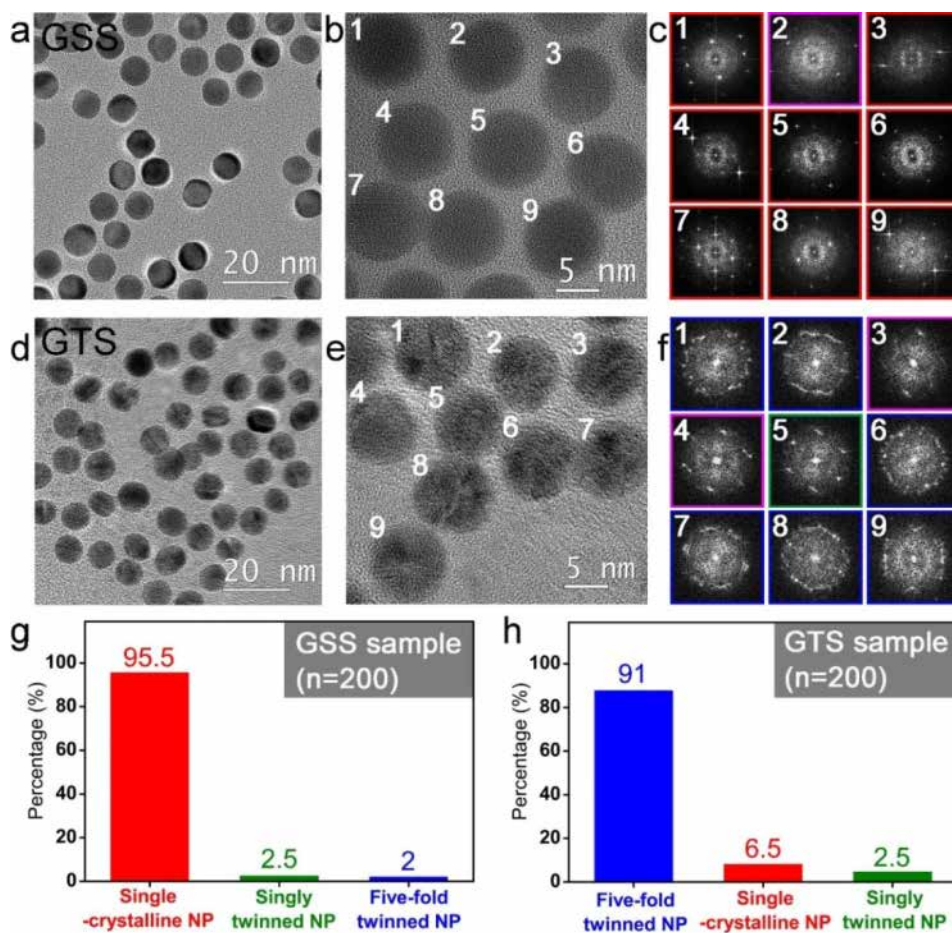


**Figure 2.5.** HRTEM analysis of the crystallinities in GSS (a-c) and GTS (d-f) particles. Examples in crystallinity identification by HRTEM and FFT analysis are given in both GSS (b and c) and GTS (e and f) cases. In each case, 200 particles were analyzed by Cs-corrected HRTEM and FFT. The identification of five-fold twinned NPs was referred to previous experimental and theoretical studies.<sup>3-5</sup> The cases with unidentifiable crystallinity, marked with pink boxes in c and f, were excluded in the data analysis, and other cases correspond to the different types of crystallinity as indicated in g and h. The percentage of single-crystalline NPs, five-fold twinned NPs and single-twinned NPs for GSS (g) and GTS (h) samples are also shown.



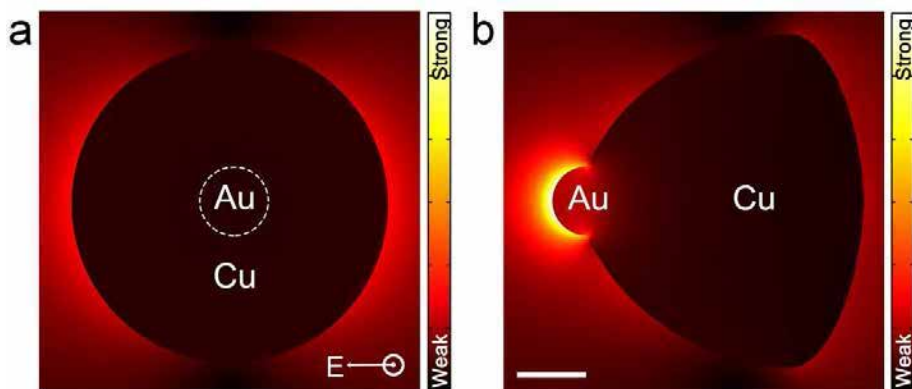


**Figure 2.6.** The calculated electromagnetic field distributions of (a) GCCS and (b) GCTT NPs. Scare bar: 10 nm.

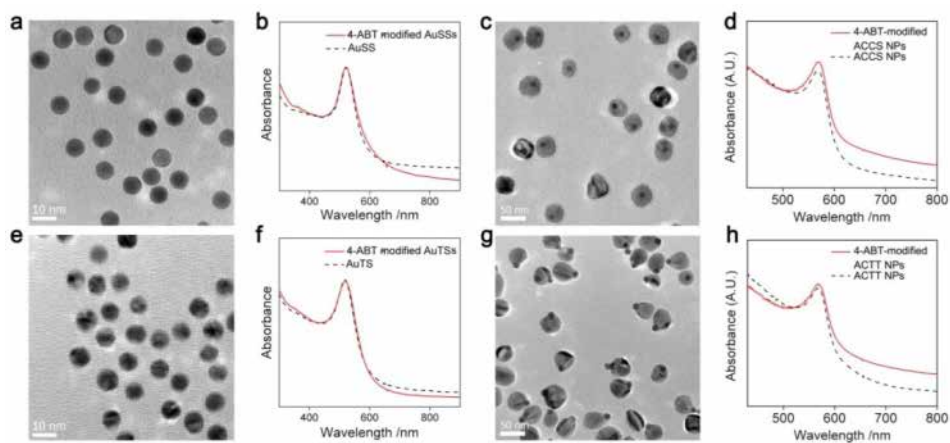


**Figure 2.7.** The TEM images and UV spectra of 4-ATP-modified GSSs (a, b) and 4-ATP-modified GTSs (e, f). The TEM images and UV spectra of GACS NPs using 4-ATP-modified GSSs as seeds (c, d) and GACTT NPs using 4-ATP-modified GTS NPs as seeds (g, h), respectively.

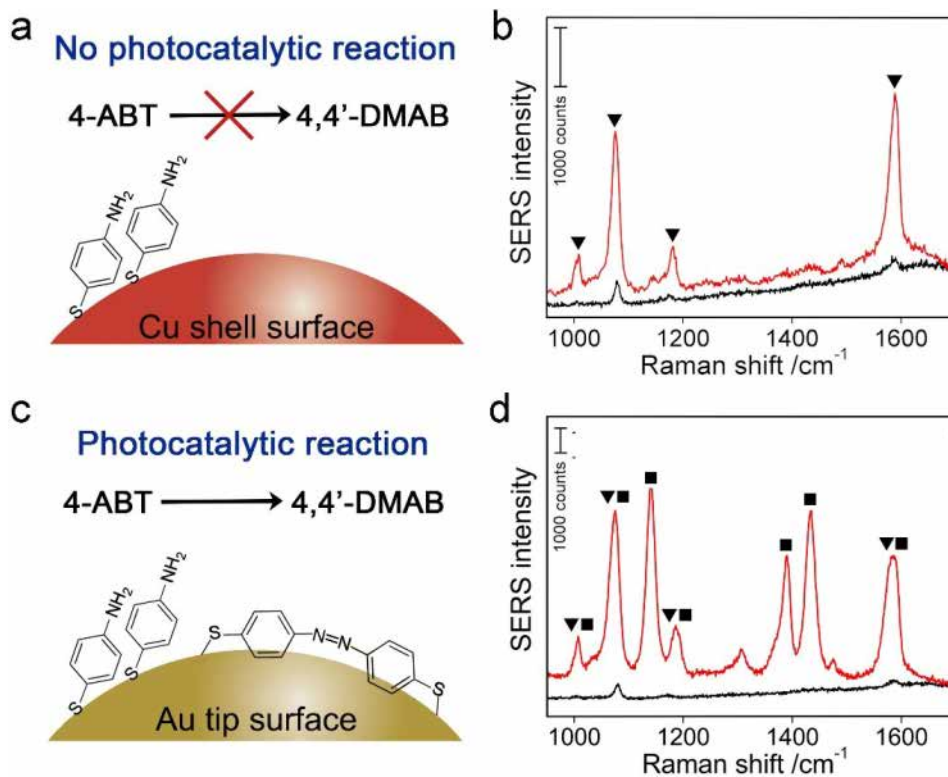


**Figure 2.8.** Schematic illustrations of the photocatalytic reactions on (a) GCCS and (c) GCTT surfaces. The SERS spectra of (b, black line) 4-ABT-modified GSSs, (b, red line) 4-ABT-modified GCCS NPs, (d, black line) 4-ABT-modified GTSs and (d, red line) 4-ABT-modified GCTT NPs ( $\blacktriangledown$ : 4-ABT;  $\blacksquare$ : 4,4'-DMAB).

**Table 2.1.** The geometric parameters of Au seed, GCCS and GCTT.

	<b>10 nm Au seed</b>	<b>GCCS</b>	<b>GCTT</b>
<b>Au shape/diameter(nm)</b>	Spherical/10	Spherical/10	Spherical/10
<b>Cu shape/diameter(nm)</b>	No	Spherical/22.5	Taper/-
<b>Surface area (nm<sup>2</sup>)</b>	314	6358	6471
<b>Volume(nm<sup>3</sup>)</b>	523.3	47712	46333



# Chapter 3: Precise Compositional Engineering and Optical Tuning in Multi-metallic Nanoantenna

## 3.1 Introduction

Controlled synthesis of colloidal multi-component nanoparticles<sup>8, 36-37, 84, 89-90</sup> is beneficial in that these particles can utilize the advantageous physicochemical properties of all the nanoscale components within one particle, and more tuned and complicated structures<sup>19, 37, 91</sup> can be designed in this manner that underpin future advances in materials. Stepwise synthesis of colloidal multi-component nanoparticles via wet chemistry can overcome the difficulties associated with composition, shape, size and crystal structure in a way that all components are optimized for creating an ideal heterostructure. Due to surface plasmon propagation, such synergistic effects resulting from the electronic and magnetic communication at the solid-state heterojunction are especially significant in multi-metallic NPs. Not only integration of characteristic plasmonic absorption of individual metal components is enabled, desired new properties can also be explored by spatially organizing subunits into multi-metallic anisotropic nanoparticles (MAPs). The plasmonic effect is one of the most promising technologies that have been explored to solve the low light manipulation efficiency in various light harvesting, transportation and conversion processes. The remarkably high plasmonic tunability in MAPs render it an excellent candidate of metallic structures<sup>42, 45, 85</sup> that facilitate diverse plasmonic enhancement in solar cell,<sup>92</sup> catalysis,<sup>93</sup> sensing,<sup>94</sup> photochemistry<sup>95</sup> and nanoantenna.<sup>96-98</sup> However, the

methodologies for precisely-controlled syntheses of either MAPs or other multi-component nanostructures have been seriously limited. Going beyond binary hybrids, high-order and junction-defined growth of MAPs or other MCPs would enable arbitrary structural manipulation towards tailored nanodevices.

Galvanic replacement reaction driven by the reduction potential difference between two metals is a powerful reaction for the synthesis of hollow nanostructures at room temperature. Due to the electrochemical nature of Galvanic replacement reaction, the sacrificial template serves as an electrode when reaction occurs at the heterointerface. As a result, atom deposition is highly sensitive and selective to the template surface, which gives advantages for Galvanic replacement reaction to create some unique structures. One of the most famous galvanic replacement products is the well-defined nanocages first reported by Xia's group, taking advantage of the faster Au deposition rate on Ag<sup>99</sup> facets. Recently, they further examined with the Pd/Pt combination and successfully fabricate subnanometer-thick Pt nanocages with well-defined and controllable facets. Ag/Au (0.17 %) and Pd/Pt (0.84 %) are the two of very rare cases that metal pairs have a lattice mismatch that is smaller than 1 %, which makes the reaction very specific. Given the unique merits of Galvanic replacement reaction, it would be a more useful and versatile tool if we can further extend it to multi-metallic nanostructures with large lattice mismatch. The unique specificity of galvanic replacement reaction comes from its nature that the surface of sacrificial templates meanwhile supplying the galvanic reduction current, working as "nano-electrodes".

Besides Galvanic replacement reaction, the challenge and complexity of large lattice-mismatched MCNPs is general in all wet chemistry approaches, laying in the emerging of overstressed heterojunctions<sup>5</sup> which induce atom dislocations that

disorder the crystallographic orientation with random defects. Most of the highly controllable structures are based on epitaxial growth inside a clear crystal structure. By minimizing random defects, we show that Galvanic replacement reaction can be used for designing and synthesizing a series of highly ordered, well-defined and tunable trimetallic plasmonic nanostructure in a way that all components have uniform shape and size with tunable junction structure. In contrast with other MCNPs, our strategy is maintaining heteroepitaxial growth inside an understandable crystal structure to enable various thermodynamic versus kinetic controlling as in single-component systems.

In this chapter, we developed a transformative heterointerface evolution (THE) method for the controlled synthesis of gold@copper-silver (G@CS) and copper-gold-silver (CGS) MAPs with the aid of polyethylenimine (PEI), polyvinylpyrrolidone (PVP) and galvanic replacement reaction, and show that the heterojunctions and plasmonic properties of two series of well-defined MAPs can be tuned in a highly controlled manner (**Figures 3.1**). We demonstrated the critical role of crystal structure in multi-metallic hybrid structure growth, and importantly, the size, composition order and morphology of a heterojunction can be tuned precisely in these MAPs, giving rise to the exceptional designability of structure and property.

## **3.2 Experimental section**

### **3.2.1 Materials and instruments**

All chemical reagents were purchased from Sigma-Aldrich except PEI (branched, MW=1,800, Polysciences) and used without further purification. The transmission electron microscopic (TEM) and Cs-corrected high resolution transmission electron microscopic (HRTEM) characterizations were performed with a

JEM-2100F (JEOL) electron microscope and a JEM-ARM200F (JEOL) electron microscope. The energy-dispersive X-ray spectroscopy (EDX) mapping measurements were performed with a JEM-2100F electron microscope. The TEM and HRTEM specimens were prepared by dropping a few microliters of concentrated nanoparticle solution on a carbon-coated copper grid or a carbon-coated nickel grid (for EDX mapping) followed by drying in vacuum. Zeta-potential measurement was performed on a Zetasizer 3500 (Malvern Instruments) equipped with a He-Ne ion laser at a wavelength of 633 nm.

### **3.2.2 Synthesis of G@CS series MAPs**

GSSs and GCCS NPs were prepared according to the protocols described in Chapter 2.2. In a typical synthesis, certain amount of freshly prepared  $\text{AgNO}_3$  solution was mixed with freshly-prepared 2.5 mM PVP (molecule weight 40000) and deionized water (DIW) to a final volume of 250  $\mu\text{L}$  with PVP concentration of 0.25 mM. From G@CS-1 to G@CS-2, G@CS-3 and G@CS-4, the [PVP] is varied from 0.1 mM to 0.2 mM, 0.3 mM and 0.4 mM, respectively. Meanwhile, freshly-prepared GCCS NPs were first washed two times with 1 mL of DIW by centrifugation at 8000 rpm for 4 min, and then redispersed in 1 mL of DIW, respectively. A portion of 250  $\mu\text{L}$  of the above GCCS NPs was one-shot injected into the above mixture of  $\text{AgNO}_3$  and PVP. The solution was kept undisturbed for 15 min at room temperature. The products were then washed twice by 0.125 mM PVP and stored in 500  $\mu\text{L}$  of 0.125 mM PVP.

### **3.2.3 Synthesis of CGS series MAPs**

GTSS and GCTT NPs were prepared according to the protocols described in Chapter 2.2. In a typical synthesis, certain amount of freshly prepared  $\text{AgNO}_3$  solution was mixed with freshly-prepared 2.5 mM PVP (molecule weight 40000)

and deionized water (DIW) to a final volume of 250  $\mu$ L with PVP concentration of 0.25 mM. From CGS-1 to CGS-2, CGS-3 and CGS-4, the [PVP] is varied from 0.1 mM to 0.2 mM, 0.3 mM and 0.4 mM, respectively. Meanwhile, freshly-prepared GCTT NPs were first washed two times with 1 mL of DIW by centrifugation at 8000 rpm for 4 min, and then redispersed in 1 mL of DIW, respectively. A portion of 250  $\mu$ L of the above GCTT NPs solution was one-shot injected into the above mixture of AgNO<sub>3</sub> and PVP. The solution was kept undisturbed for 15 min at room temperature. The products were then washed twice by 0.125 mM PVP and stored in 500  $\mu$ L of 0.125 mM PVP.

### **3.2.4 Synthesis of junction-engineered MAPs**

Various junction-engineered G@CS and CGS MAPs were synthesized under the conditions listed in **Table 3.1**. Note that **Table 3.1** only lists the reaction conditions for G@CS-1 and CGS-1 series MAPs, however, various MAPs with precisely engineered compositional size, structural order and junction morphology can be synthesized according to this method, simply by varying the concentration of copper precursor, silver precursor and PVP. In our method, ascorbic acid was used as a reducing agent, and the low pH value (pH 3 in our case) successfully inhibited the formation of oxides. Moreover, the amine-rich carbon backbone of PEI is known to be a good capping ligand for stabilizing copper NPs. In a sealed vial, GCCS and GCTT NPs can be stable for >one month. When trimetallic NPs were synthesized and kept in 0.5 % PVP solution, they are stable for >one month.

## **3.3 Results and Discussion**

### **3.3.1 Precise compositional control in MAPs**

For the strategic synthesis of multi-metallic structures with transformative heterointerface, the galvanic replacement reactions were performed by mixing an

aqueous solution of  $\text{AgNO}_3$  and PVP with GCCS or GCTT templates described in Chapter 2 at room temperature for 15 min, respectively. The replacement of copper by silver is a two-electron reaction, in which two portions of silver will be deposited when one portion of copper is consumed. Therefore, the sizes of copper and silver components can be tuned simultaneously through altering the concentration of  $\text{AgNO}_3$  ( $[\text{Ag}^+]$ ) to control the extent of galvanic replacement reaction. **Figures 3.2a** and **3.3a** show two series of MAPs synthesized with different  $[\text{Ag}^+]$ . Structural order of the three components was well defined and controlled in G@CS and CGS MAP series. As shown in **Figure 3.2a**, silver NP grew on GCCS NP surface during galvanic replacement reaction, resulting to a gold-copper-silver structural order. In contrast, silver NP selectively grew from the gold tip on GCCS NP, forming a copper-gold-silver structural order. The spatial distributions of gold, copper and silver in MAPs were characterized by energy-dispersive X-ray spectroscopy (EDX) mapping. As  $[\text{Ag}^+]$  increased, the size of copper domain gradually decreased before finally disappearing and instead, a newly emerged silver domain was observed. The reaction was also monitored by UV-Vis extinction spectrum and solution color (**Figures 3.2b, 3.3b**). The results clearly suggest that the optical properties of these nanostructures are tunable and solution color change was clearly visible. As reaction proceeded, the copper SPR peaks ( $\sim 570$  nm) decreased with increasing  $[\text{Ag}^+]$ , and only the silver SPR peak ( $\sim 410$  nm) was remained after the completion of galvanic replacement reaction.

The mechanism of template dissolution and silver nucleation can be deduced from the shape of bimetallic template and the position of gold seed at different extent of galvanic replacement reaction. As copper domain becomes smaller, its shape gradually transforms from round corner cube to thermodynamically-favored sphere

(**Figure 3.2a**). Meanwhile, the distance of GSS to the silver domain shortens (from G@CS-1 to G@CS-3), and finally directly in contact with Ag upon complete replacement of copper (G@CS-4). It indicates that the dissolution kinetic of Cu shell is mild enough to allow layer-by-layer peeling of copper atoms. Besides, the electrochemical nature of galvanic replacement reaction facilitates a highly surface-sensitive Ag nucleation and deposition. After Ag's first nucleation on GCCS template, the subsequent atom deposition specifically occurs on the fresh silver surface (schematically illustrated in **Figure 3.2a**). Comparing with the non-specific nucleation of silver on the GCCS template surface, the exposed gold tip in GCTT templates serves as a "nano-electrodes" (schematically illustrated in **Figure 3.3a**) for Ag's under potential deposition (UPD). Multiple nucleation was not observed because the fresh silver nuclei becomes an advantageous electrode surface comparing with other PEI-capped template surface, resulting the high-order and well-crystallized structure.

### **3.32 Precise structural and optical engineering in MAPs**

We further studied the roles of PVP and PEI in the precise engineering of MAP morphology and heterointerface. The zeta-potentials of GCCS and GCTT templates dispersed in water were  $27.0\pm 0.7$  mV and  $22.4\pm 0.9$  mV, respectively, and the values dropped to  $14.6\pm 0.4$  mV and  $14.9\pm 0.5$  mV, respectively, after the addition of PVP. Since PVP has a nearly neutral charge, the large zeta-potential decrease upon PVP addition suggests that PVP may partially exchange with PEI during the galvanic replacement reaction. As shown in **Figure 3.4**, without the presence of PVP, the high surface energy of silver sub-NP lead to a spherical shape, and a large distance between copper and silver sub-NPs was found with GTS as a bridge. It indicates that such polymer exchange process can be used to tune the

junction morphology of MAPs. When [PVP] is low, while the copper surface is well protected with PEI along with minimal replacement of PEI with PVP, resulting in a narrow junction between copper surface and silver sub-NPs (**Figure 3.5a**). As [PVP] increases, the surface energy of the silver sub-NP is reduced, and the exchange between PEI and PVP promotes the expansion of the heterojunction. Regarding the G@CS MAP series (**Figure 3.5b**), the heterojunction expansion direction is tangent to the particle longitudinal axis. The junction width expands with increase in [PVP] while the configuration of sub-NPs remains similar. As a result, its structure gradually shifts from a small-junction dimer (G@CS-1-1) to a thick-junction dimer structure (G@CS-1-4). In contrast, regarding the CGS MAP series (**Figure 3.5c**), the heterojunction expansion direction moves along the longitudinal axis of the particle due to the presence of a gold sub-NP at the junction. Interestingly, a dumbbell-like trimer structure (CGS-1-1) was formed at low [PVP], in which the GTS serves as a “bridge” between copper and silver sub-NPs. As [PVP] increased, the “bridge” length shortened accordingly, and the gold was eventually buried by silver (CGS-1-4).

Besides of the well-controlled compositional shape and size, uniform junction morphology and heterointerface were also achieved. This was also demonstrated by the extinction spectra of these MAPs due to the unique charge transfer plasmon (CTP) mode of such nanoantenna structures. The CTP mode is highly sensitive to the tiny changes at the junction, which results in huge difference in the SPR wavelength and intensity. **Figure 3.6** shows the extinction spectra of G@CS-1 (a) and CGS-1 (b) series NPs, respectively. As [PVP] increases, the corresponding NIR peaks gradually blue shift, indicating a junction-dependent CTP, which well matches with the previous theoretical and experimental results of a CTP.<sup>100-101</sup>



From CGS-1-1 to CGS-1-4, their SPR peak rapidly shifts from ~945 nm to ~710 nm, indicating the high sensitivity of SPR to the junction morphology. Nevertheless, in both CGS and G@CS cases, the NIR peak wavelength (black spots) and intensity (hollow red spots) exhibit a near-perfect linearity ( $R^2 > 0.98$ ) with [PVP], indicating the junction morphology can be tuned quantitatively by PVP. Note that the precise control over junction morphology is extremely challenging, no matter via stepwise synthesis or monomer assembly. Our results demonstrated that crystal structure-engineering of start building blocks can largely improve the controllability at the sticky heterojunction, even when three different components are involved simultaneously. This should be attributed to the successful suppression of random defects on the NP surface, which guarantees the site-specific growth in multi-step fabrications.

### 3.33 Optical properties of MAPs

The junction controllability in MAPs is of particular importance due to the strong antenna effect supported by these structures, and their high sensitivity to the geometry alternations at the junction.<sup>42, 102</sup> The junction controllability in MAPs is of particular importance due to the strong antenna effect in these structures and their high sensitivity to heterojunction geometry.<sup>42, 102</sup> We found that the far-field and near-field properties of these antennas can be finely tuned in MAP structures, and large part of the sun spectrum, especially in the NIR region, can be covered by these structures. To understand the junction-dependency and the electromagnetic interaction between sub-NPs inside MAPs, three-dimensional finite-element method (3D-FEM) simulations were conducted. As shown in **Table 3.2**, our initial G@CS models consist of a 40-nm GCCS cube with a 25 nm silver NP, while the contacted junction between them was varied from 5 nm (M1), 7 nm (M2), 10 nm

(M3) to 14 nm (M4) in diameter. As junction width increases, the SPR peak sensitively blue shift from 1280 nm (M1) to 700 nm (M4), which is consistent with our experimental data (**Figure 3.6a**). This result well matches with the previous theoretical and experimental results, which implied that such low-frequency SPR is corresponding to a charge transfer plasmon (CTP).<sup>100-101</sup> The CTP mode is highly sensitive to the tiny changes at the junction, which results in huge difference in the SPR wavelength and intensity. As a result of CTP, intense EM-fields are localized at the junction area (**Figure 3.8**), which is up to 217 times higher than the incident light for a 5 nm-junction G@CS NP (M1). This light focusing effect is inversely proportional to the junction width. As the junction narrows down, the corresponding peak width rapidly broadens both in experimental (**Figure 3.6a**) and theoretical (**Figure 3.7a**). This is because the volume of junction supporting CTP decreases due to the decrease of junction width and length simultaneously (from M4 to M1). This junction width-dependent SPR shift has been experimentally proposed for plasmonic nanosnowmen with a conductive junction<sup>42</sup> and nanowire-bridged dimer<sup>101</sup>, and theoretically studied in plasmonic cavities with a conductive junction<sup>103</sup> and rod antenna with a conductive filament.<sup>104</sup> As junction narrows down, the peak intensity rapidly decreases and the peak width largely broadens, which is a result of energy dissipation due to the poor conductivity at the junction.<sup>103</sup> Regarding models M5 to M8 (**Figure 3.7b**), the silver sub-NP was positioned from 4-nm apart (M5) to 2-nm apart (M6), in contact with the copper sub-NP (M7) and overlapped with copper sub-NP (M8). Other than M4 (the thick junction case) and M8 (the overlapped case), the electromagnetic field was strongly localized within the junction area (**Figure 3.8 and 3.9**).

The optical energy, namely, the power stored with the antenna is proportional to the integral of square of the local electric field ( $E^2$ ). Quantitative analysis was performed by volume integral of  $E^2$  on these antenna structures. The junction area and 2-nm peripheral area were defined respectively in G@CS and CGS models, which were used to calculate the corresponding volume integral of  $E^2$ . As shown in **Figure 3.10**, the gray bars ( $\int E_{periphery}^2$ ) display the volume integral of  $E^2$  over the 2-nm peripheral area of models M1 to M8, and the black bars ( $\int E_{junction}^2$ ) represent the  $E^2$  contribution from their junction regions (junction field). The  $\int E_{junction}^2$  to  $\int E_{periphery}^2$  ratio describes the electric field localization efficiency of an antenna. Overall, the highly localized field in the small junction area was much stronger than the overall field intensity on particle surface for 80-nm gold nanoparticle and 80-nm gold NR. From M4 to M1, the  $\int E_{junction}^2$  to  $\int E_{periphery}^2$  ratio rapidly increases from 24% (M4) to 63% (M1), indicative of the importance of the junction size in inducing stronger localized field around the junction. Among M5 to M8, the M7, in which silver and copper sub-NPs are in contact, displayed the strongest field intensity around the junction area. In contrast, the electric field was remarkably decreased when the junction area was buried with silver. It should be also noted that M1 shows the strongest localization efficiency in the near-field, but its  $\int E_{periphery}^2$  value (**Figure 3.10**) and far-field peak intensity (**Figure 3.6a** and **3.7a**) are the lowest. This phenomenon was also experimentally observed in the plasmonic nanosnowmen with a conductive nanojunction<sup>42</sup> and a nanowire-bridged dimer,<sup>101</sup> and was theoretically studied in the plasmonic cavities with a conductive junction<sup>103</sup> and the rod antenna with a conductive filament.<sup>104</sup> As junction narrows down, the SPR peak intensity rapidly damps and the peak width largely broadens,

which are due to the energy dissipation at the junction.<sup>103</sup> As a result, the near-field properties of these antenna structures are inversely correlated with their far-field properties, which largely limit their applications.

### **3.34 Possible application of MAPs**

The ultrahigh controllability in MAPs offers an unprecedented tunability in plasmonic antennas and various plasmonic enhanced applications. First, MAPs can utilize the characteristic SPR peak of multiple metal components, and the ratio of different wavelength region can be tuned by altering the size of individual nanocomponents. Second, an additional SPR peak can be generated at the NIR region through the coupling of sub-NPs, and the intensity of this NIR peak can be largely enhanced by junction engineering. The promising plasmonic enhancement in solar cell,<sup>105</sup> hydrogen generation<sup>12, 18</sup> and various plasmon-enhanced applications<sup>106</sup> only occurs at the narrow SPR wavelength of the metal NPs,<sup>12, 68-69</sup> which largely limits their light utilization efficiency. Therefore, the customization of metal SPR absorption is extremely important. As shown in **Figure 3.6b**, the SPR spectra of junction-engineered MAPs broadly cover the sunlight spectrum from UV to NIR, indicating extension of metal SPR to a large range in the optical wavelength, or even covering the whole sunlight spectrum is possible through proper design of MAPs. Third, the nanoscale manipulation and transportation of light is an important function in many devices. The highly tunable MAPs can serve as a versatile antenna model for the study of energy harvest, transfer and dissipation between multiple metals. Supported by junction engineering, MAPs can efficiently focus light into nanoscale “hotspots” and even isolate such “hotspot” to a sub-10 nm Au NP. These new improvements will prompt new theoretical and

experimental investigations in future nano-plasmonic device engineering and photochemistry.

### **3.4 Conclusion**

In summary, we developed new material designing and synthetic approaches in forming and tuning trimetallic nanostructures via finely engineering galvanic replacement, PEI and PVP on crystal structure-engineered bimetallic templates. We showed that two series of well-defined MAPs (transformative gold@copper-silver MAP and copper-gold-silver MAP) can be synthesized in a high yield, and their structures and plasmonic properties are highly controllable. Our approach allows for efficient integration and coupling of characteristic SPR properties of sub-nanocomponents within a single MAP, showing high potential for extending plasmonic enhancement in various plasmon-enhanced applications. Moreover, nm-scale heterojunction engineering capability with three different components, the tunability over the ‘confined-neck junction’ to ‘open-neck junction’ and the fine balancing of far-field and near-field properties in copper-gold-silver MAPs offer opportunity for plasmonic control and enhancement in various metal and semiconductor-based energy applications or diffusion-based catalytic applications. These capabilities can provide new insights and prompt new theoretical and experimental investigations in plasmonics and photochemistry. The strategies and results herein open revenues for the design, synthesis, optical tunability, and plasmonic applications of anisotropic multi-component metal nanostructures.

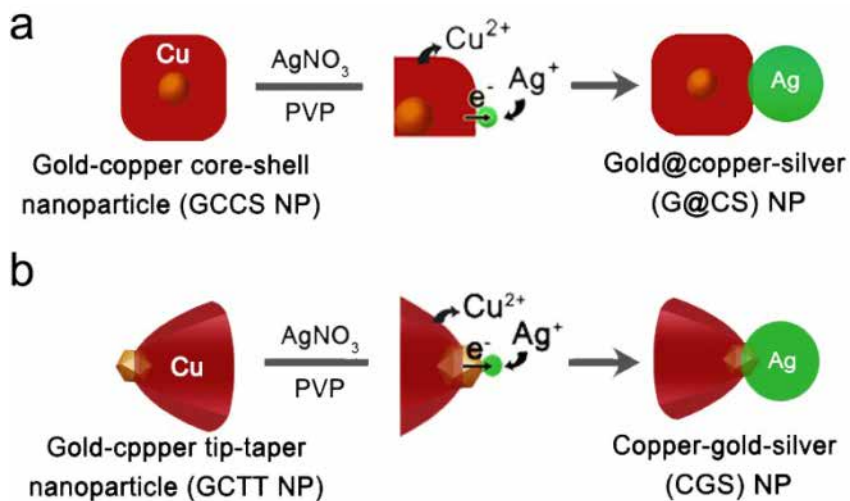


**Figure 3.1.** Schematic illustration of galvanic replacement reaction using GCCS NP (a) and GCTT NP (b) as templates. The electrochemical nature of galvanic replacement reaction provides enhanced site specificity for GCTT structure while the gold tip serves as a “nano-electrode” to conduct the galvanic current.

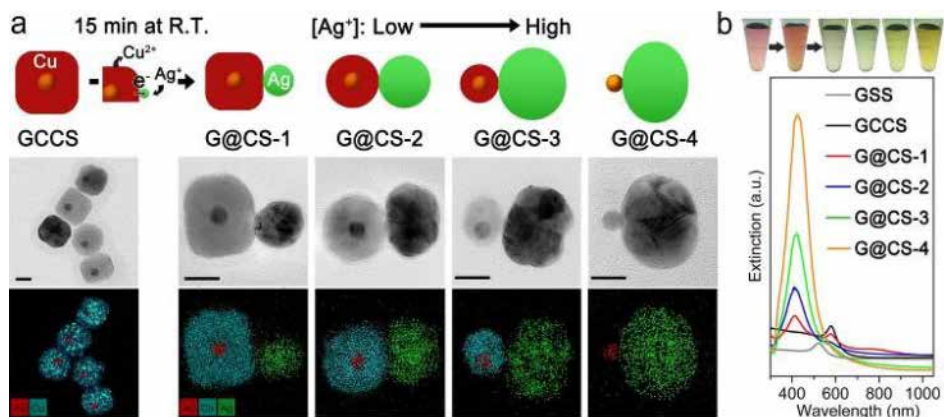


**Figure 3.2.** (a) Tuning of gold@copper-silver (G@CS) multicomponent anisotropic nanoparticles (MAPs) from GCCS NPs by altering the reaction extent of galvanic replacement reaction. HRTEM images and corresponding EDX mapping images of GCCS NPs and the corresponding galvanic replacement products. (b) Corresponding digital image and extinction spectra of GSS, GCCS NP and G@CS series MAPs. Scale bars are 20 nm.

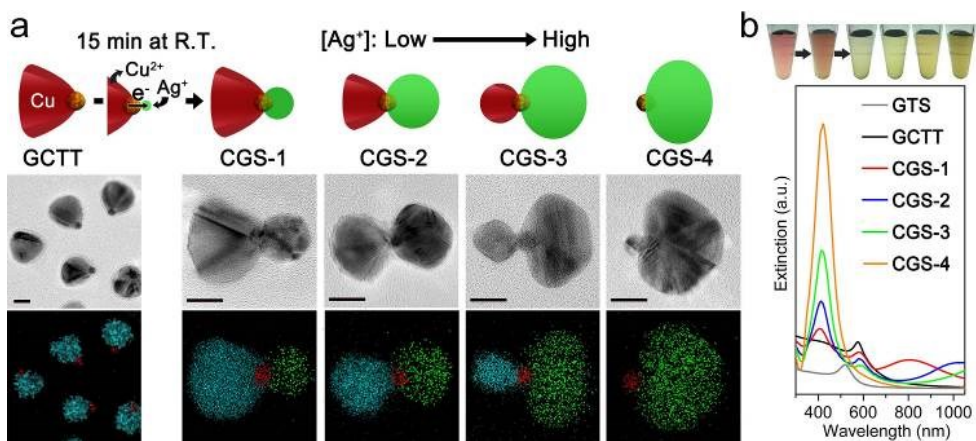


**Figure 3.3.** (a) Tuning of copper-gold-silver (CGS) MAPs from GCTT NPs by altering the reaction extent of galvanic replacement reaction. HRTEM images and corresponding EDX mapping images of GCTT NPs and the corresponding galvanic replacement products. (b) Corresponding digital image and extinction spectra of GTS, GCTT NP and CGS series MAPs. Scale bars are 20 nm.



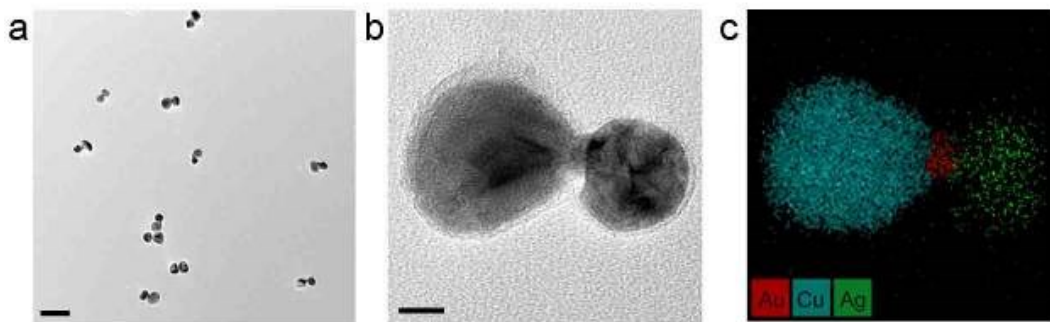


**Figure 3.4.** (a) TEM image of CGS-1-0 MAPs synthesized without the addition of PVP. (b) Magnified image of a CGS-1-0 MAP showing an elongated gold junction, and (c) the corresponding EDX mapping pattern. Scale bars are 100 nm and 10 nm in a and b respectively.

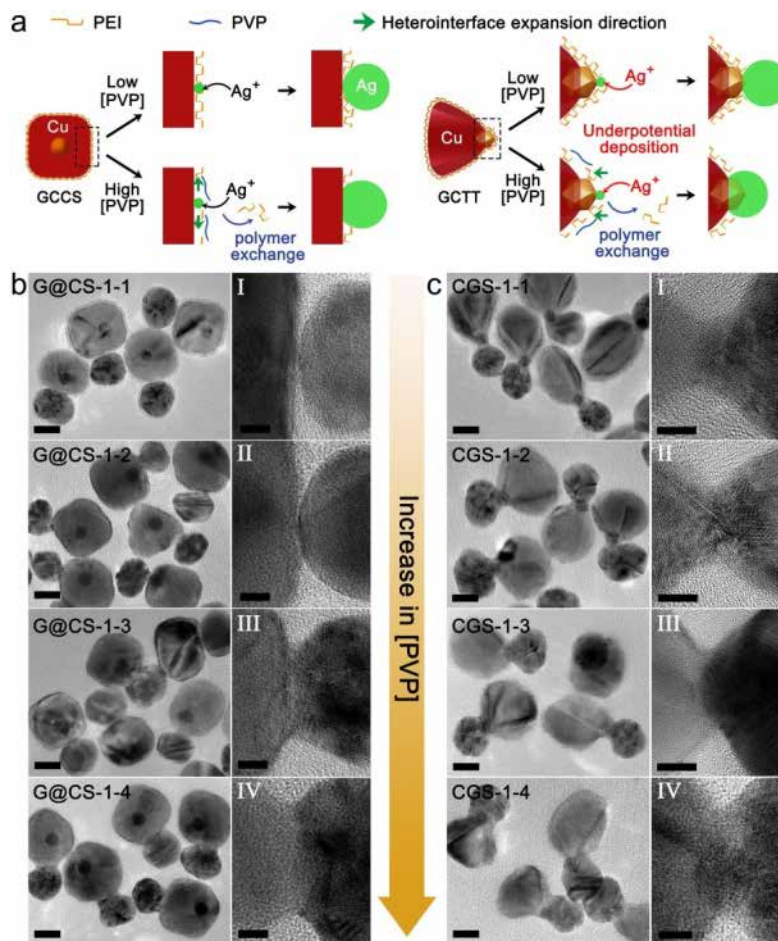


**Figure 3.5.** (a) Schematic illustration of the heterointerface evolutions mechanism in MAPs. GCCS and GCTT NPs were initially capped with PEI (a good ligand for copper), and then partially replaced by PVP (a bad ligand for copper and a good ligand for silver) during the galvanic replacement reaction. Due to PEI protection, multiple nucleation of silver is inhibited, and the polymer exchange mechanism allows us to fine tune the junction properties through the exchange rate. (b, c) TEM images of junction-engineered (b) G@CS MAP series and (c) CGS MAP series, as well as corresponding high-magnification HRTEM images showing four junction morphologies (I to IV), respectively. Scale bars are 20 nm and 5 nm in low-magnification and high-magnification images, respectively.

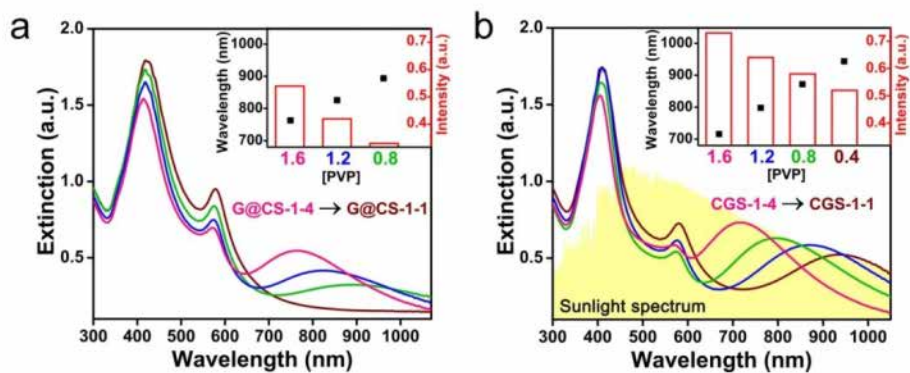


**Figure 3.6.** Extinction spectra of (a) G@CS-1 and (b) CGS-1 series MAPs synthesized by varying PVP concentrations. Insets show the effect of PVP concentration on NIR peak wavelength (solid black dots) or peak intensity (hollow red bars).

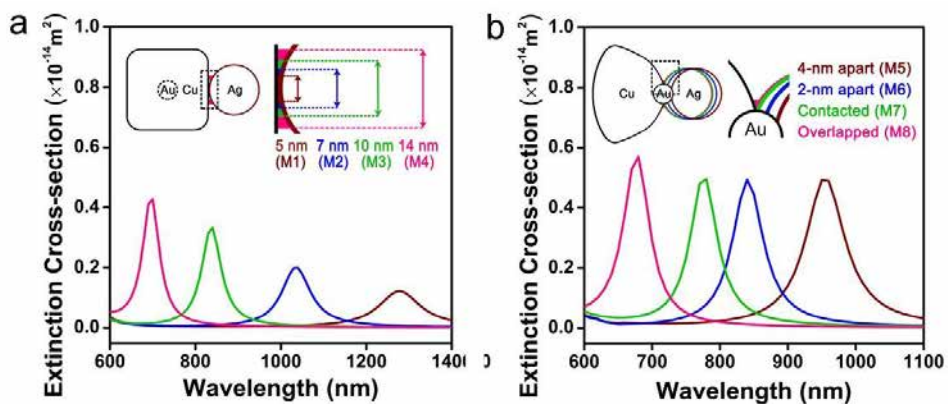


**Figure 3.7.** The extinction cross-sections of (a) the junction-engineered G@CS (models M1 to M4) and (b) CGS (models M5 to M8) MAPs in the NIR region.

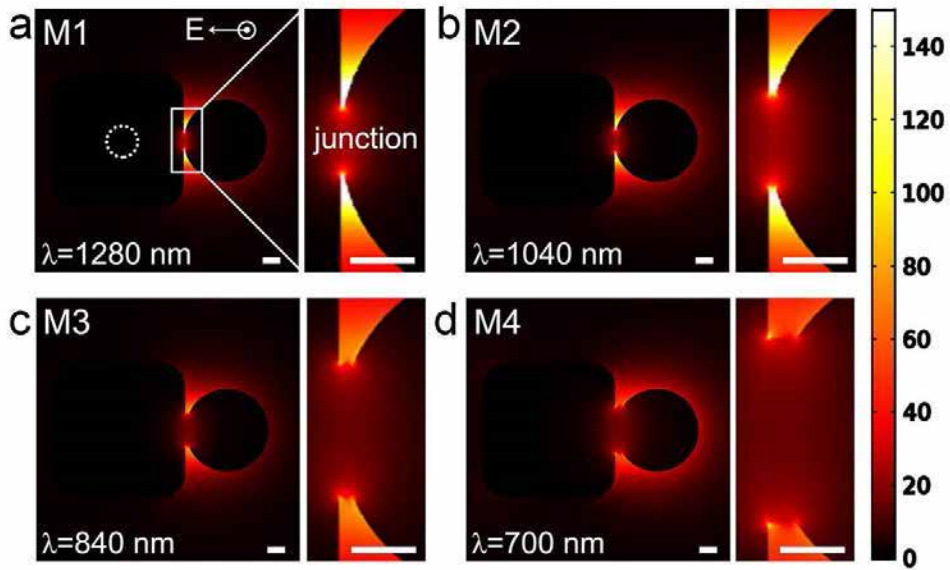


**Figure 3.8.** The electric field distributions (left) and magnified junction areas (right) of (a) M1, (b) M2, (c) M3 and (d) M4, respectively, at their respective charge transfer plasmon (CTP) peak wavelengths. Scale bars are 5 nm.

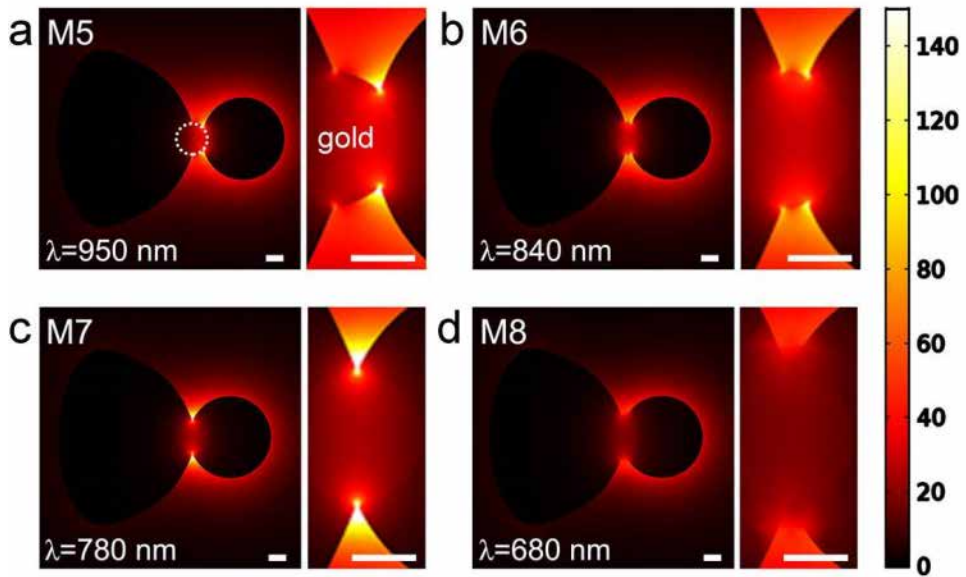


**Figure 3.9.** The electric field distributions (left) and magnified junction areas (right) of (a) M5, (b) M6, (c) M7 and (d) M8, respectively, at their respective charge transfer plasmon (CTP) peak wavelengths. Scale bars are 5 nm.

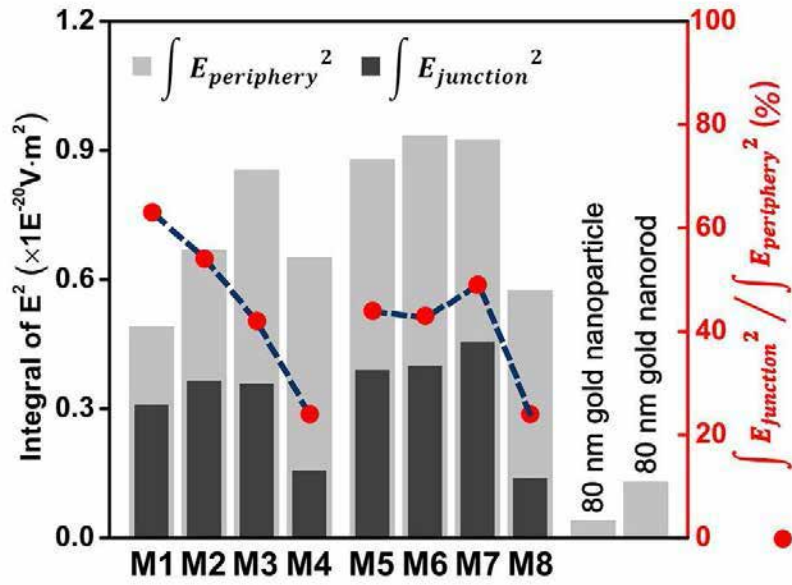


**Figure 3.10.** The volume integral of square of electric field ( $E^2$ ) from the 2-nm-periphery of each structure ( $\int E_{periphery}^2$ , gray bars) and the defined junction area ( $\int E_{junction}^2$ , black bars).

**Table 3.1.** Summary of reaction conditions for synthesis of G@CS and CGS MAPs.

<b>Sample No.</b>	<b>Volume of AgNO<sub>3</sub> (μL)</b>	<b>Volume of PVP (μL)</b>	<b>Volume of DIW (μL)</b>	<b>Volume of template (μL)</b>
<b>G@CS-1</b>	10	25	215	250 of GCCS NP
<b>G@CS-2</b>	20	25	205	250 of GCCS NP
<b>G@CS-3</b>	40	25	185	250 of GCCS NP
<b>G@CS-4</b>	80	25	145	250 of GCCS NP
<b>G@CS-1-1</b>	10	10	230	250 of GCCS NP
<b>G@CS-1-2</b>	10	20	220	250 of GCCS NP
<b>G@CS-1-3</b>	10	30	210	250 of GCCS NP
<b>G@CS-1-4</b>	10	40	200	250 of GCCS NP
<b>CGS-1</b>	10	25	215	250 of GCTT NP
<b>CGS-2</b>	20	25	205	250 of GCTT NP
<b>CGS-3</b>	40	25	185	250 of GCTT NP
<b>CGS-4</b>	80	25	145	250 of GCTT NP
<b>CGS-1-0</b>	10	0	240	250 of GCTT NP
<b>CGS-1-1</b>	10	10	230	250 of GCTT NP
<b>CGS-1-2</b>	10	20	220	250 of GCTT NP
<b>CGS-1-3</b>	10	30	210	250 of GCTT NP
<b>CGS-1-4</b>	10	40	200	250 of GCTT NP



**Table 3.2.** The geometric parameters for gold, copper and silver components in simulation models of various MAPs structures.

	<b>Gold</b>	<b>Copper</b>		<b>Silver</b>
		<b>G@CS</b>	<b>CGS</b>	
<b>Diameter (nm)/Shape</b>	10	Cube	Taper	25
<b>Calculated volume (nm<sup>3</sup>)*</b>	523.3	59265	58732	~8180

\*Noted that the surface area and volume were calculated based on the simulation model by software.

# Chapter 4: Synthesis of Monodisperse Ag-Ag<sub>2</sub>S NPs as Platform for Metal-Semiconductor Nanostructures

## 4.1 Introduction

The rational combination of multiple crystalline components into nanoscale heterostructures is featured by the enhanced chemical and physical properties and new synergistic effects.<sup>9, 107-109</sup> Among them, metal-semiconductor heterostructures have attracted particular attentions due to their unique photoelectric and catalytic properties for various optoelectronic nanodevices and nanosystems.<sup>110-111</sup> Metal-semiconductor nanostructures in diverse shapes have been prepared by seed-mediated methods, including core/shells-structured Au@CdS, Au@Ag<sub>2</sub>S, Au@ZnS NPs and TiO<sub>2</sub>-Au NRs.<sup>112-116</sup> However, there are few synthetic tools available for well-defined metal-semiconductor nanostructures.<sup>117-119</sup> As a result, it is in urgent need to develop new strategies to fabricate metal-semiconductor nanostructures.

Heteroepitaxial growth is one of the most effective methods in the fabrication of precisely controlled multicomponent nanostructures,<sup>120</sup> Until recently, most of the heterostructures were fabricated in this manner.<sup>115-116, 121</sup> Typically, heteroepitaxy occurs at the interface between metal/metal, sulfide/sulfide, oxide/sulfide or oxide/oxide when they have an identical or quasi-identical crystalline structure and similar lattice spacing. In seed-mediated methods, lattice strain is established upon the formation of heterointerface, inducing lattice expansion or lattice contraction in the core and shell of the hybrid.<sup>21</sup> The restoring force of the lattice-contracted

shell exerts the strain in the radial direction, while the lattice of the seed NPs expands until the restoring forces from the shell and the seed are at equilibrium.<sup>21</sup> Such strain establish-strain release-strain equilibrium mode enables the rational design of multicomponent nanostructures with core-shell or head-body structure. However, the lack of flexibility in strain release patterns largely limits the chance of unique structures and the exploration of new synergistic effects.

Alternatively, if multiple components can simultaneously nucleate and grow, the driving forces of strain equilibrium readily guide the deposition and transformation of each component. Unconventional growth patterns that beyond crystal structure engineering and facet control can be explored. Heterointerfacial strain equilibrium (HSE) was achieved not only by the directional growth in overgrowth shell phase (as in seed-mediated methods), but also through the extension and transformation of heterointerface, enabling the phase transition and phase segregation during the process. To establish a HSE growth pattern, several criteria should be fulfilled: i) simultaneous nucleation and growth; ii) slow kinetic (low precursor concentration) to allow thermodynamic driven growth; iii) proper surfactant with low facet preference. The atomization of lattice strain may facilitate the exploration of new crystal growth pattern, material phase and unique synergistic effects.

In this chapter, we demonstrated a HSE strategy for the one-pot synthesis of Ag-Ag<sub>2</sub>S metal-semiconductor NPs, where self-responsive and self-limiting growth was found in the nanocomponents. As shown in **Figure 4.1a**, the chemical reaction between AgNO<sub>3</sub> and Na<sub>2</sub>S<sub>2</sub>O<sub>4</sub> generate Ag<sub>2</sub>S<sub>2</sub>O<sub>4</sub>, which further decomposes to Ag<sub>2</sub>S and H<sub>2</sub>SO<sub>4</sub>. The kinetic of the reaction was controlled by another chemical equilibrium between Ag<sup>+</sup> and AgCl (s), while AgCl was readily

dissolved at 95°C. Thus silver ions were gradually released to react with  $\text{Na}_2\text{S}_2\text{O}_4$ , allowing the diffusion-controlled growth. At room temperature, the crystal structure of  $\text{Ag}_2\text{S}$  is described in **Figure 4.1b**, known as monoclinic  $\alpha\text{-Ag}_2\text{S}$ . The heterointerface transformation was schematically illustrated in **Figure 4.1c**. The HSE-corrected Ag- $\text{Ag}_2\text{S}$  NP showed extraordinarily high thermodynamic stability against various etchants and long-term storage. Moreover, it facilitated the enhanced site selectivity in the galvanic replacement reactions between Ag and other noble metals, leading to the uniform synthesis of various metal-semiconductor nanostructures.

## **4.2 Experimental section**

### **4.2.1 Materials and instruments**

All chemical reagents were purchased from Sigma-Aldrich and used without further purification. The field emission-scanning electron microscopic (FE-SEM) measurements were conducted on a MERLIN Compact (ZEISS) electron microscope. Powder XRD measurements were performed by a SmartLab (Rigaku, Japan) powder X-ray Diffractometer. The transmission electron microscopic (TEM) and Cs-corrected high resolution transmission electron microscopic (HRTEM) characterizations were performed with a JEM-2100F (JEOL) electron microscope and a JEM-ARM200F (JEOL) electron microscope in the National Center for Inter-University Facilities (NCIRF), respectively. The energy-dispersive X-ray spectroscopy (EDX) mapping measurements were performed with a JEM-2100F electron microscope. The TEM and HRTEM specimens were prepared by dropping a few microliters of concentrated nanoparticle solution on a carbon-coated copper grid followed by drying in vacuum.

### **4.2.2 Synthesis of colloidal Ag- $\text{Ag}_2\text{S}$ NPs**

In a typical synthesis of Ag-Ag<sub>2</sub>S NPs with a diameter of 25 nm, Na<sub>2</sub>S<sub>2</sub>O<sub>3</sub> (0.1 M, 60 μL) and AgNO<sub>3</sub> (0.1 M, 150 μL) were added into a well-dissolved solution of cetyltrimethylammonium chloride (CTAC, 0.1 M, 10 mL) under stirring (200 rpm) at 95 °C. The solution color gradually changed from transparent to yellowish brown. The reaction was allowed to continue at 95 °C for 90 min, before washing with 1 mM CTAC solution and centrifugation under 12,000 rpm (this procedure was repeated 3 times). The final products were redispersed and stored in 1 mL of 1 mM CTAC solution before use.

#### **4.2.3 Synthesis of colloidal Au-Ag<sub>2</sub>S NPs**

The synthesis of Au-Ag<sub>2</sub>S NPs were achieved by galvanic replacement reaction using the above 25 nm Ag-Ag<sub>2</sub>S NPs as template and HAuCl<sub>4</sub> as gold precursor. In a typical synthesis, 1 mL of the above Ag-Ag<sub>2</sub>S NPs was centrifuged and redispersed in CTAC solution (50 mM, 10 mL) and stirred under 200 rpm for 15 min. Another CTAC solution (50 mM, 10 mL) was mixed with HAuCl<sub>4</sub> solution (5 mM, 200 μL), and added to the first CTAC solution. The mixture was stirred overnight and washed with 1 mM CTAC solution and centrifugation under 10,000 rpm (this procedure was repeated 3 times), and finally stored in 1 mL of 1 mM CTAC solution.

#### **4.2.4 Synthesis of colloidal Ag-Ag<sub>2</sub>S@Pt NPs**

The synthetic protocol of Ag-Ag<sub>2</sub>S@Pt NPs was similar to that of Au-Ag<sub>2</sub>S NPs, except using K<sub>2</sub>PtCl<sub>4</sub> as precursor. Typically, K<sub>2</sub>PtCl<sub>4</sub> solution (5 mM, 200 μL) was used in the reaction. It should be noted that the amount of K<sub>2</sub>PtCl<sub>4</sub> is excessive to the amount of Ag on Ag-Ag<sub>2</sub>S NPs, but Ag was not fully replaced even with a higher K<sub>2</sub>PtCl<sub>4</sub> concentration (5 mM, 500 μL) in this experiment.

#### **4.2.5 Synthesis of colloidal Ag<sub>2</sub>S@Pd NPs**

The synthetic protocol of Ag-Ag<sub>2</sub>S@Pt NPs was similar to that of Au-Ag<sub>2</sub>S NPs, except using Na<sub>2</sub>PdCl<sub>6</sub> (5 mM, 200 μL) as precursor.

### 4.3 Results and Discussions

#### 4.3.1 One-pot synthesis of Ag-Ag<sub>2</sub>S NPs

In our method, the synthesis of Ag-Ag<sub>2</sub>S NP was achieved in cetyltrimethylammonium chloride (CTAC) solution at 95° C, while AgNO<sub>3</sub> and Na<sub>2</sub>S<sub>2</sub>O<sub>4</sub> were used as silver and sulfur source, respectively. Interestingly, as shown in **Figure 4.2a**, monodisperse multicomponent NPs were formed in 120 min, which composed of a larger cubic component and a relatively smaller component at one corner of the cube. Large scale SEM images demonstrated the high uniformity of the product. The synthetic yield was estimated to be nearly 100% by analyzing more than 500 particles. TEM image in **Figure 4.2b** further shows the Janus structures of hybrid NPs and their uniformity in size and shape. Interestingly, these NPs can self-assembly into NP super lattice on the TEM grid (**Figure 4.2c**), further indicating a monodisperse nature. In EDX mapping results (**Figure 4.2d**), the signal from Ag element existed in both larger cubic sub-NP and smaller sub-NP while the signal from S element only existed in larger cubic sub-NP, indicating that such a dimer NP consists of Ag<sub>2</sub>S NP and Ag NP.

#### 4.3.2 Time-dependent structure characterization

Cs-corrected high-resolution transmission electron microscopy (HRTEM) was used to investigate the time-dependent atomic structure evolution of the Ag-Ag<sub>2</sub>S NP. **Figure 4.3** shows the time-dependent HRTEM images of Ag-Ag<sub>2</sub>S NP from 20 min (S1, a), 40 min (S2, b) to 120 min (S3, c). A Janus nuclei composed of a multi-twinned Ag head and a stoichiometric Ag<sub>2</sub>S body was formed within 20 min (**Figure 4.3a**). The decahedral structure of Ag sub-NPs was further revealed by

FFT, showing 5 sets of symmetric  $\{200\}$  spots. At stage S1, the Ag and Ag<sub>2</sub>S nanocomponents exhibited a similar diameter of ~8 nm, and the five-fold twin axis was perpendicular to the Ag/Ag<sub>2</sub>S heterointerface. Subsequently, the two components simultaneously grew larger following their initial crystal structure. At stage S2, the diameter of Ag<sub>2</sub>S (~21 nm) obviously exceeded that of Ag (~14 nm). Interestingly, the shape of Ag<sub>2</sub>S gradually evolved into an isotropic round-corner cubic shape, while Ag favored the growth along the five-fold twin boundaries instead of the five-fold twin axis (**Figure 4.3b**). After 120 min of reaction (stage S3), the cubic shape of Ag<sub>2</sub>S further sharpened and the increase of heterointerface was achieved by the extension of twinned Ag. Further extension of reaction time does not change the shape and size of the products. As shown in **Figure 4.3c**, eventually the Ag component is considerably smaller than the Ag<sub>2</sub>S part, showing an interesting bowl-like shape covering one corner of the cubic Ag<sub>2</sub>S nanocomponent. The heterointerface evolution during the growth was monitored in dark-field mode and corrected by EDX line profile. From S1 to S2, the curvature of heterointerface dramatically decreased, and then dramatically increased in reverse direction from S2 to S3, which strongly evidenced the heterointerface evolution during the growth. The atomic ratio was estimated to be 74.04: 25.95 (Ag: S) in S3 by EDX spectrum, further evidencing the presence of metallic Ag. As shown in the insets of **Figure 4.3b and c**, the primitive unit of lattice matrix shifts from a rhomboid corresponding to the monoclinic structure (C<sub>2h</sub> group) to a square corresponding to a tetragonal (D<sub>4h</sub> group) or cubic structure (O<sub>h</sub> group), indicating lattice reorganization during the structure evolution. Compared with a 30-nm Ag<sub>2</sub>S NP (**Figure 4.3j**), the primitive unit of the lattice matrix typically showed a rhomboid shape, due to the monoclinic structure.

We then further employed the X-ray powder diffraction (XRD) measurements (**Figure 4.3k**) to study the time-dependent structure evolution of Ag-Ag<sub>2</sub>S NPs. Due to the small size of Ag sub-NP and the overlaying with Ag<sub>2</sub>S patterns, diffraction patterns of Ag cannot be identified. As comparison, the XRD pattern of a 30-nm Ag<sub>2</sub>S was measured, which matched well with standard  $\alpha$ -Ag<sub>2</sub>S (PDF#14-0072). From stage S1 to S3, the hybrid NP went through several structure evolutions. In contrast to the  $\langle -121 \rangle$  as strongest diffraction peak (marked with stars) in the 30-nm Ag<sub>2</sub>S sphere, the strongest and second strongest diffraction peaks were  $\langle -112 \rangle$  and  $\langle 022 \rangle$  in various stages of Ag-Ag<sub>2</sub>S NPs. It indicated that preferential growth may occur since stage S1 due to the existence of heterointerface. As NPs grow larger (stage S2), most diffraction peaks can be indexed to  $\alpha$ -Ag<sub>2</sub>S except a new diffraction peak at 35.7° (labeled by the red dot line), suggesting a structure adjustment. In contrast, some of the  $\alpha$ -Ag<sub>2</sub>S diffraction peaks were obviously weakened or disappeared in the final structure (stage S3), while the new diffraction peak further strengthened, indicating a phase transition. Moreover, shifting of diffraction peaks was found during the structure adjustments (as indicated by green dot lines), further suggesting the expansion or contraction of certain lattice planes in phase transition.

#### **4.3.3 Behavior of HSE-directed NP**

Upon the formation of heterointerface in seed-mediated methods, lattice strain readily breaks the strain equilibrium in both core and shell components, leading to a strain-governed growth until the restoring forces from core and shell at equilibrium. In HSE-directed growth, the “core” and “shell” co-nucleate and atom depositions occur on both sides simultaneously, allowing the transformative evolution of heterointerface and both components for recovering of strain



equilibrium. Both time-dependent HRTEM and XRD measurements suggested that our Ag-Ag<sub>2</sub>S NPs are formed by HSE-directed growth. The transformative evolution of heterointerface and the self-limiting growth of Ag indicated the thermodynamic-driven atom deposition. The phase transition in Ag and Ag<sub>2</sub>S further suggested that new crystal structure may be stabilized in HSE process, due to the equilibrium of lattice strain from heterointerface.

Size-controlling behavior in HSE-directed NP was found to be unique. Simple increase of the precursor concentration does not show any influence to the NP size. Alternatively, it turned out that NP size was determined by the concentration of CTAC surfactant. Due to the chemical equilibrium between Ag<sup>+</sup> and AgCl enabled by CTAC, the equilibrium concentration of Ag<sup>+</sup> can be controlled by tuning the CTAC concentration. A relatively lower CTAC concentration resulted in the higher equilibrium concentration of Ag<sup>+</sup> at the initial growth stage, leading to a higher number of nuclei and a smaller diameter of final structure. As shown in **Figure 4.2** and **Figure 4.4**, when CTAC concentration was increased from 100 mM, 120 mM, 140 mM to 160 mM, the diameter of Ag-Ag<sub>2</sub>S NPs can be tuned from 32.5 ± 2.3 nm, 45.7 ± 3.5 nm, 63.5 ± 5.2 nm to 75.8 ± 8.3 nm, respectively. Interestingly, the Ag versus Ag<sub>2</sub>S diameter ratio only slightly changed from 1.54 to 1.75, while the shape and structure configurations of differently sized Ag-Ag<sub>2</sub>S NPs remain similar. The high uniformity in various growth stages and in the wide diameter range indicates that each of the nanocomponents independently respond to the strain equilibrium during the growth, further evidencing a HSE-directed growth mode.

#### **4.3.4 HSE-induced thermodynamic stability**

To further investigate the growth mechanism, a series of experiments were conducted to test the chemical stability of Ag-Ag<sub>2</sub>S NPs. Oxidative etching of the Ag component was firstly conducted with iron nitride,<sup>122</sup> ammonium hydroxide/hydrogen peroxide<sup>123</sup> and nitric acid.<sup>124</sup> Iron nitride, which has been widely used as Ag etching reagent at a concentration below 15 mM, didn't show any detrimental effect to the Ag-Ag<sub>2</sub>S NPs even at a high concentration of 50 mM. Moreover, ammonium hydroxide/hydrogen peroxide etching solution according to reference<sup>123</sup> does not etch the Ag component on Ag-Ag<sub>2</sub>S NPs. Regarding nitric acid, the Ag-Ag<sub>2</sub>S NPs remain stable when nitric acid concentration is below 100 mM, while higher concentration of etchant dissolves both Ag and Ag<sub>2</sub>S. As shown in **Figure 4.5**, successful etching of Ag was achieved by changing the ligands from CTAC to polymers; however, it results in the aggregation and merging of Ag<sub>2</sub>S NPs into nanoparticle chains. These results indicate that a high energy barrier may exist to etch Ag from Ag-Ag<sub>2</sub>S NP.

We then evaluated the long-term stability of Ag-Ag<sub>2</sub>S NPs by TEM, XRD, UV-vis spectrum, and SERS. Note that Ag NPs were usually suffering from oxidation in applications, especially in aqueous media.<sup>125</sup> Interestingly, our Ag-Ag<sub>2</sub>S NPs showed surprisingly high chemical stability. As shown in **Figure 4.6**, we compared the chemical structure and optical properties of Ag-Ag<sub>2</sub>S NPs during 3 months. Under TEM observation (**Figure 4.6a**), the shape and size of Ag-Ag<sub>2</sub>S NPs remained unchanged, showing distinct contrast and clear boundaries. XRD measurements (**Figure 4.6b**) demonstrated that the unchanged crystal structure of Ag-Ag<sub>2</sub>S NPs. During three months observation, we also measured the UV-vis spectra (**Figure 4.6c**) of Ag-Ag<sub>2</sub>S NPs every week, which showed that their extinction remained unchanged.

#### 4.3.5 HSE-induced site specificity

To further explore the application of HSE-corrected Ag-Ag<sub>2</sub>S nanostructures, galvanic replacement reactions were designed to replace Ag with noble metals such as Au, Pt and Pd. The electrochemical nature of galvanic replacement reaction is believed to promote site specificity in nanosynthesis.<sup>126-128</sup> Besides, the Ag-Ag<sub>2</sub>S nanostructure showed high resistance of Ag oxidation (etching) due to the energy barrier of decreasing Ag/Ag<sub>2</sub>S heterointerface, which can be utilized as a thermodynamic driving force to promote site-specific formation of new metal/Ag<sub>2</sub>S heterointerface. As shown in **Table 1**, the standard reduction potential difference between two metal pairs drove the galvanic replacement reaction towards the oxidative dissolution of metal with lower reduction potential (the less noble one), and the reductive deposition of metal with higher reduction potential. During the redox reaction, electron should be transferred to the metal precursor (the one with higher reduction potential) for its reduction reaction. As shown in **Figure 4.7a**, the galvanic replacement reactions between Ag and various noble metals showed distinguished atom deposition behaviors. In general, Ag has the highest electron conductivity among natural materials and there is a smaller lattice mismatch between metals than that between metal and semiconductor. Therefore, the noble metals should favor nucleation on Ag surface or self-nucleation in the close surface of Ag, and with least preference in the nucleation on Ag<sub>2</sub>S surface. However, experimental results (as indicated in **Figure 4.7b**) revealed that the deposition of Au atoms preferred a Janus configuration with Ag<sub>2</sub>S, leading to an Au-Ag<sub>2</sub>S NP. In contrast, Pd deposition promoted a core-shell configuration with Ag<sub>2</sub>S to generate an Ag<sub>2</sub>S@Pd NP.

HRTEM images and the EDX mapping results of Au-Ag<sub>2</sub>S NPs were shown in **Figure 4.8**. The Au-Ag<sub>2</sub>S NPs showed a high uniformity in structure configurations and NP morphology, where the Au sub-NP showed a unique taper shape. EDX mapping (**Figure 4.8c**) demonstrated the existence of Au as a taper shape, and Ag signal was also found in the metal part, indicating some Ag may remain in the Au sub-NP. EDX line profile in **Figure 4.8c** agrees well with mapping results, further suggesting some amount of Ag may remain in the Au region. **Figure 4.9** shows the HRTEM images and the EDX mapping results of Ag<sub>2</sub>S@Pd NPs. As shown in **Figure 4.9a and b**, the particles show a uniform cubic structure with relatively sharp edges. Ag showed a much darker contrast than Ag<sub>2</sub>S under TEM, which was not observed in the product. EDX mapping showed that a layer of Pd was existed on the Ag<sub>2</sub>S surface, indicating the deposition of Pd in a core-shell mode. EDX Line profile indicates that Pd well-distributes on the Ag<sub>2</sub>S surface without special preference.

Most interestingly, the deposition of Pt showed a self-limiting behavior, in which Ag cannot be fully replaced in spite of a large excess amount of Pt precursor was used. As shown in **Figure 4.10**, the diameter of Ag decreased from  $17.3 \pm 1.5$  nm to  $13.6 \pm 1.2$  nm, while shape and diameter of Ag<sub>2</sub>S remain unchanged. EDX mapping and line profile both demonstrated the existence of Ag NP and Pt layer on the Ag<sub>2</sub>S surface. The self-limiting dissolution of Ag further indicated that the exchange of heterointerface is strongly governed by the HSE effect.

#### **4.4 Conclusion**

In this work, we successfully developed a one-pot method for the synthesis of uniform Ag-Ag<sub>2</sub>S NPs by a HSE method. The growth mechanism of Ag-Ag<sub>2</sub>S NPs

was studied by time-dependent HRTEM and XRD, supporting the HSE mechanism. It was found that the as-synthesized Ag-Ag<sub>2</sub>S NPs exhibit a high thermodynamic stability against Ag etching and oxidation, which was attributed to the high energy barrier for structure reorganization. It was further demonstrated to promote site-specificity in galvanic replacement reactions, giving rise to the formation of uniform Au-Ag<sub>2</sub>S, Ag<sub>2</sub>S@Pd and Ag-Ag<sub>2</sub>S@Pt NPs. In contrast to the strain establish-strain release-strain equilibrium mode, the HSE method here is a powerful, though preliminary, demonstration of unique multicomponent synthetic designs.

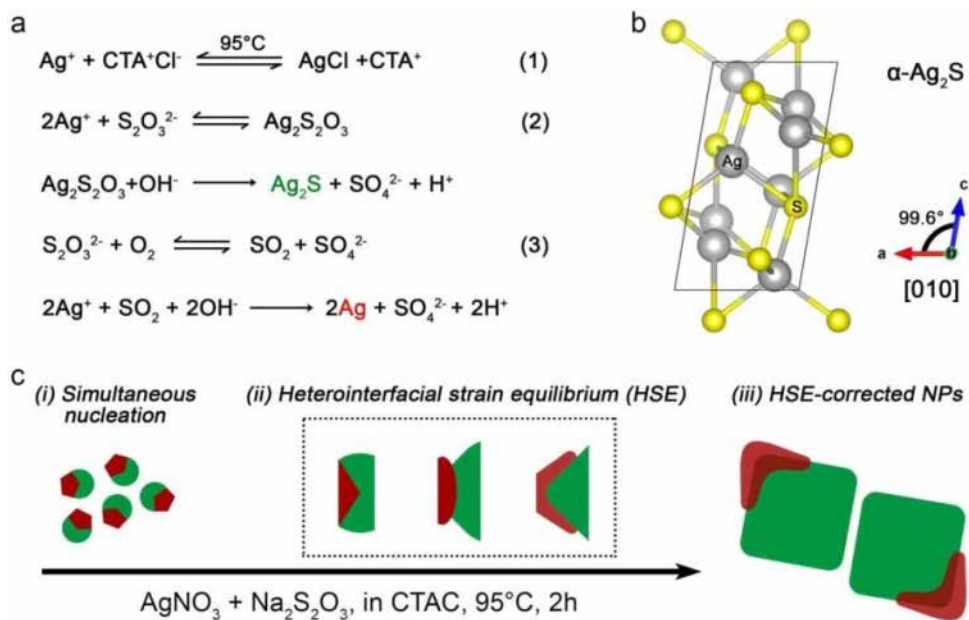


**Figure 4.1.** (a) Chemical reactions under the reaction conditions. (b) Crystal structure illustration of monoclinic  $\alpha\text{-Ag}_2\text{S}$ . (c) Schematic illustration of the heterointerfacial strain equilibrium (HSE) process during Ag-Ag<sub>2</sub>S formation.

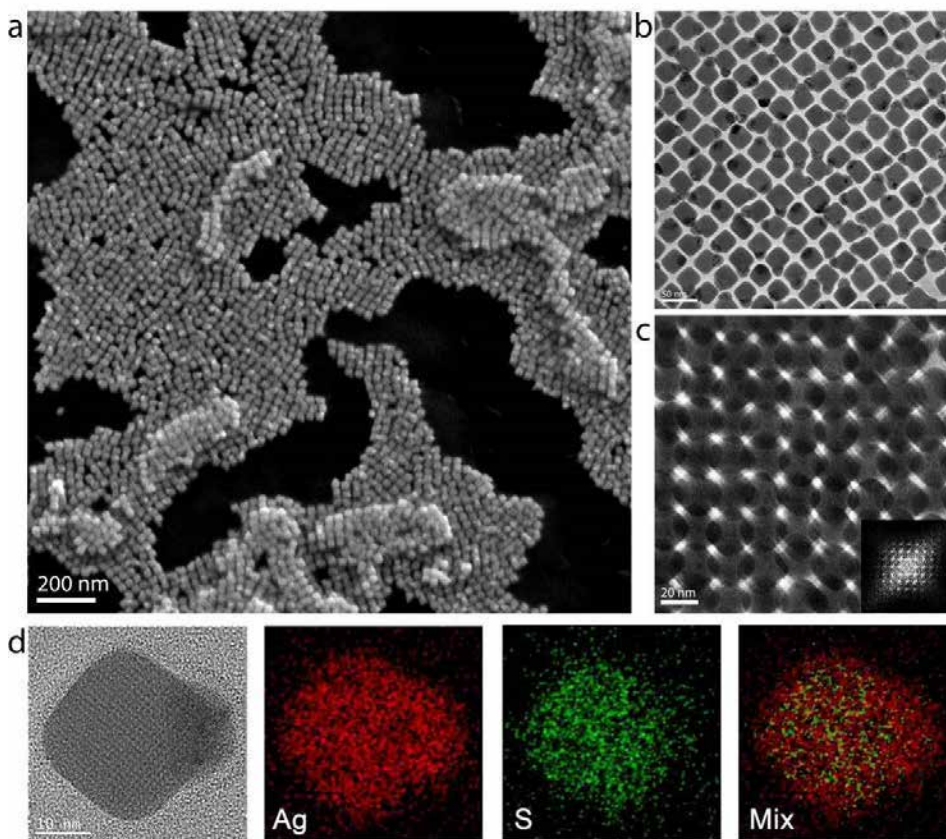


**Figure 4.2.** (a) SEM and (b) TEM images of Ag-Ag<sub>2</sub>S NPs. (c) TEM image showing Ag-Ag<sub>2</sub>S NPs super lattice. (d) EDS mapping result of an Ag-Ag<sub>2</sub>S NPs.

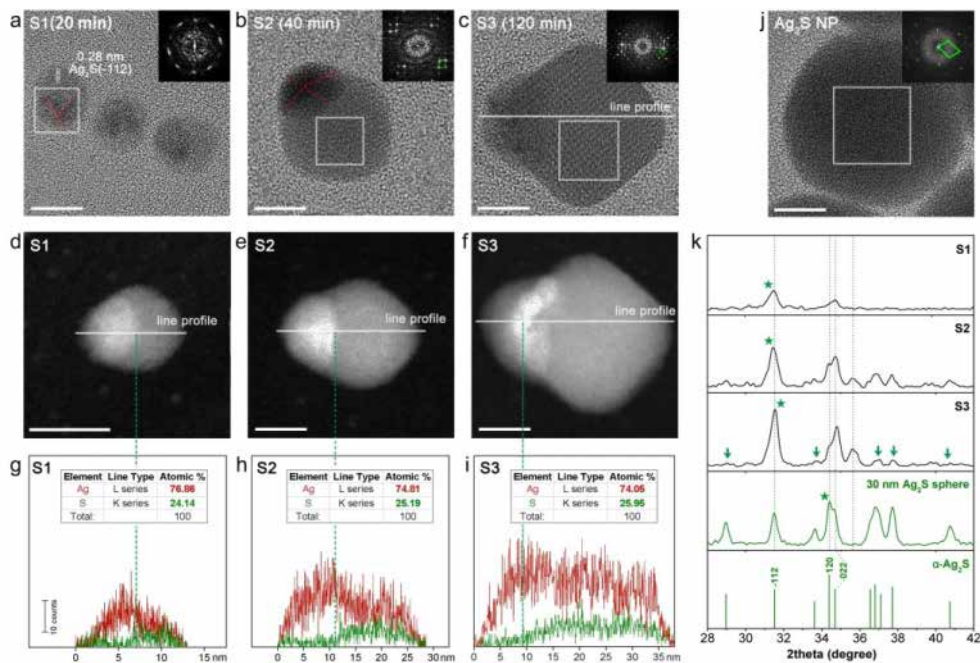


**Figure 4.3.** Time-dependent (a-c) bright-field HRTEM image, (b-d) dark-field HRTEM images and (g-i) EDX line profiles corresponding to Ag-Ag<sub>2</sub>S NPs at various growth stages, ranging from 20 min (S1), 40 min (S2) to 120 min (S3), respectively. (j) HRTEM image of a 30-nm Ag<sub>2</sub>S NP. Scale bars are 10 nm. Insets in a, b, c and h are FFT patterns corresponding to the highlighted square regions in each images, respectively. (k) Time dependent XRD patterns showing various growth stages of Ag-Ag<sub>2</sub>S NPs and the 30-nm Ag<sub>2</sub>S NP.



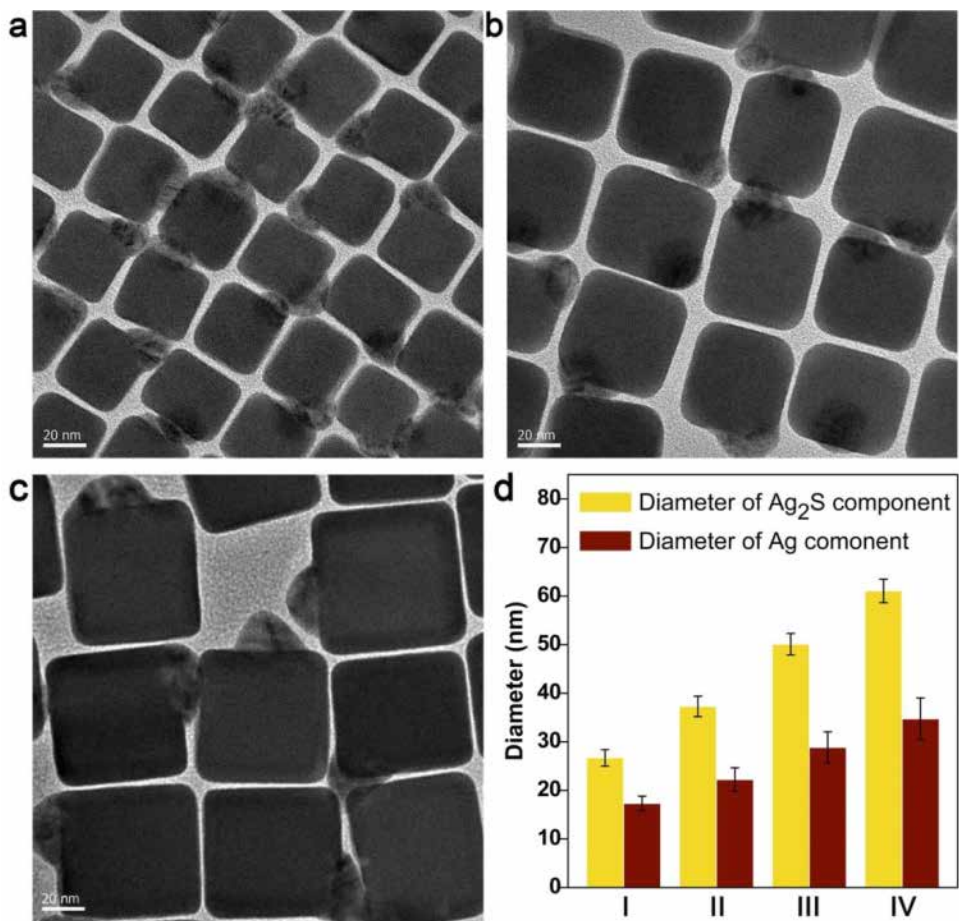


**Figure 4.4.** The effect of CTAC concentration to the size and shape of Ag-Ag<sub>2</sub>S NPs. (a-c) TEM images show the Ag-Ag<sub>2</sub>S NPs as CTAC concentration increased from 100 mM (Figure 4.1a), 120 mM (a), 140 mM (b) to 160 mM (c). (d) Summary of Ag and Ag<sub>2</sub>S nanocomponent size synthesized at various CTAC concentration: 100 mM (I), 120 mM (II), 140 mM (III) to 160 mM (IV), indicating a self-limiting growth behavior.

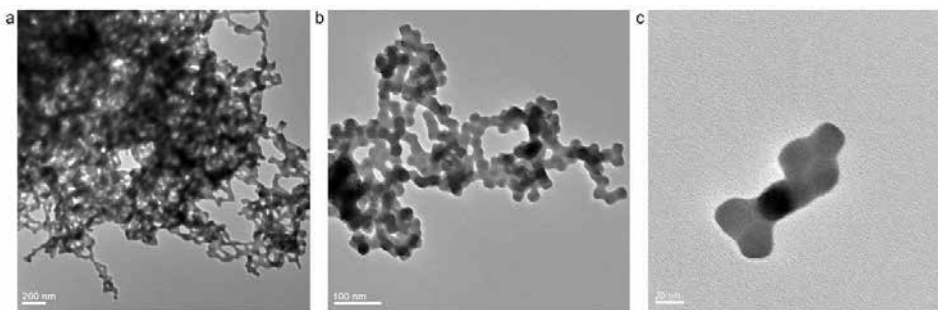


**Figure 4.5.** Etching of Ag from Ag-Ag<sub>2</sub>S NPs in 1% PVP using Fe(NO<sub>3</sub>)<sub>3</sub> solution as etching reagent at a concentration of 10 mM.

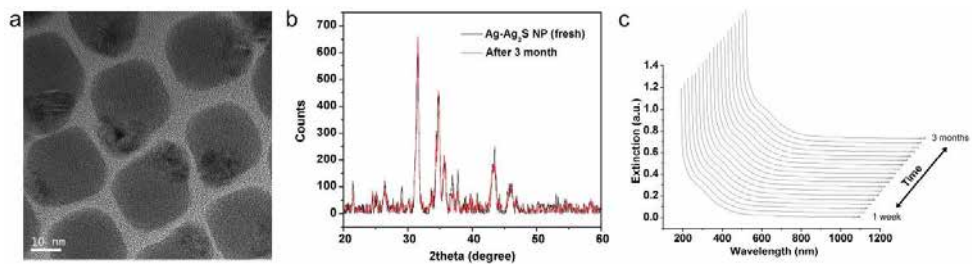


**Figure 4.6.** (a) HRTEM, (b) XRD patterns and (c) UV-vis spectra of Ag-Ag<sub>2</sub>S NPs after 3 months of synthesis.

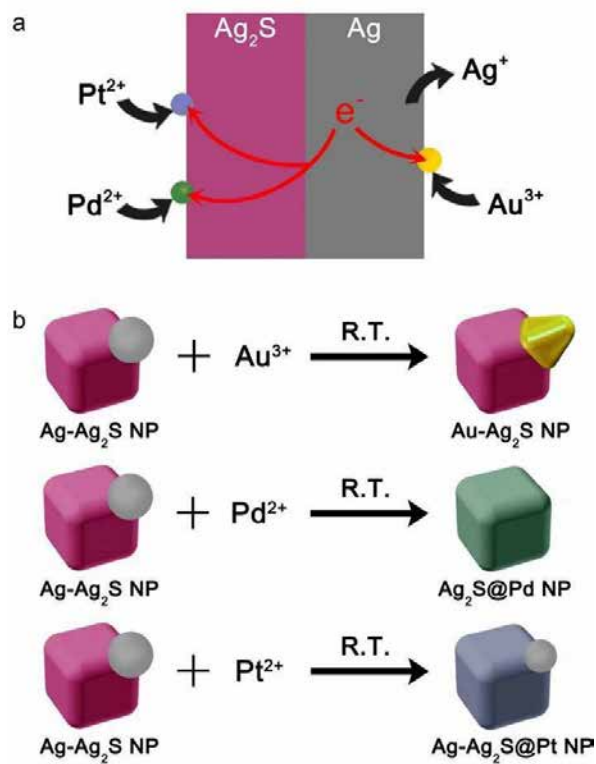


**Figure 4.7.** (a) Schematic illustration of the site-selective heterointerface evolution between Ag and various noble metals. (b) Schematic illustrations of the galvanic replacement reactions and the corresponding multi-component NPs.

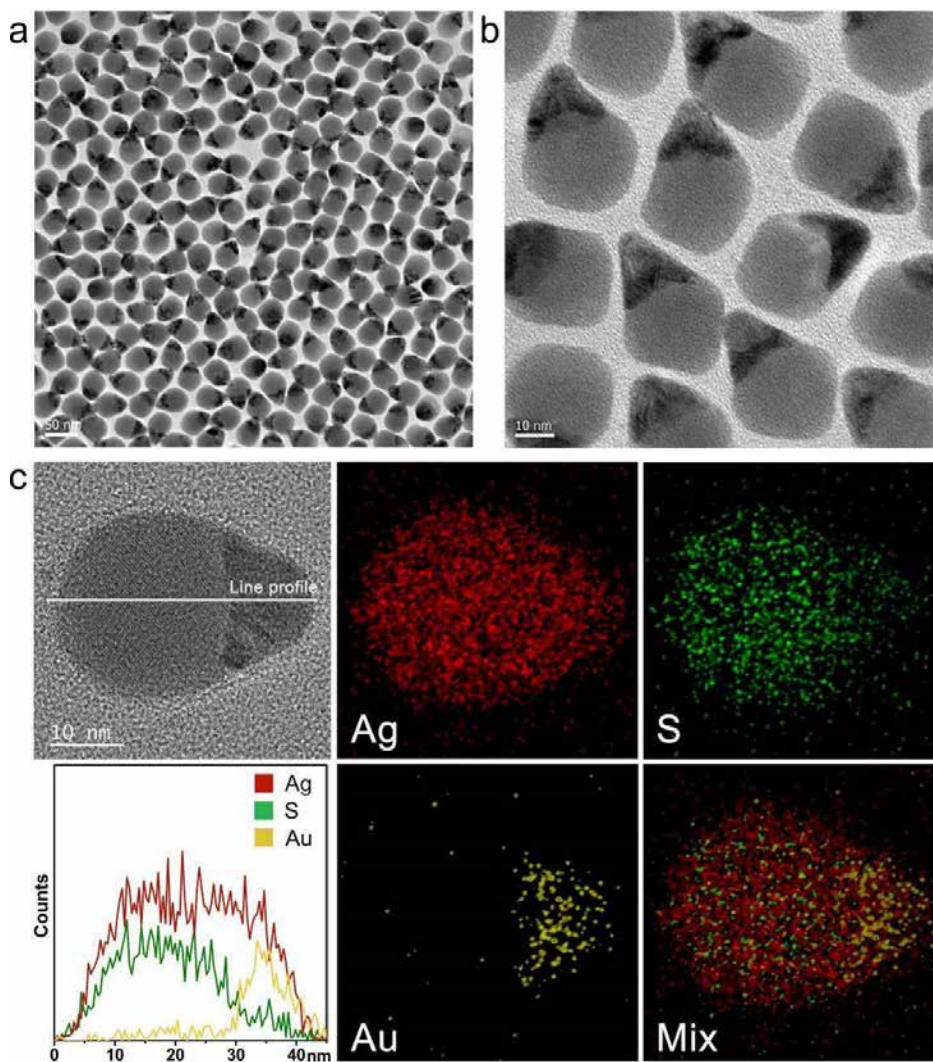


**Figure 4.8.** (a,b) HRTEM images, (c) EDX mapping and line profile results of Au-Ag<sub>2</sub>S NPs.

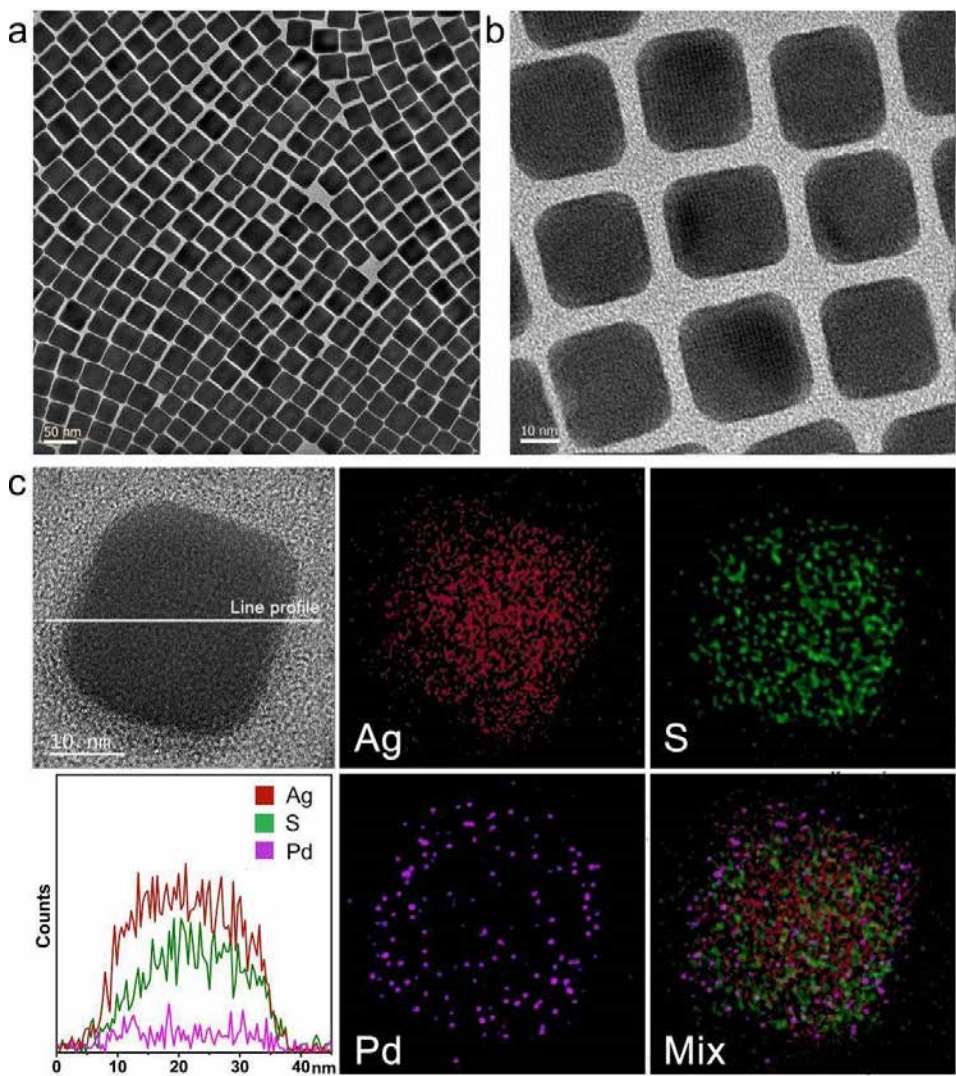


**Figure 4.9.** (a,b) HRTEM images, (c) EDX mapping and line profile results of  $\text{Ag}_2\text{S}@\text{Pd}$  NPs.



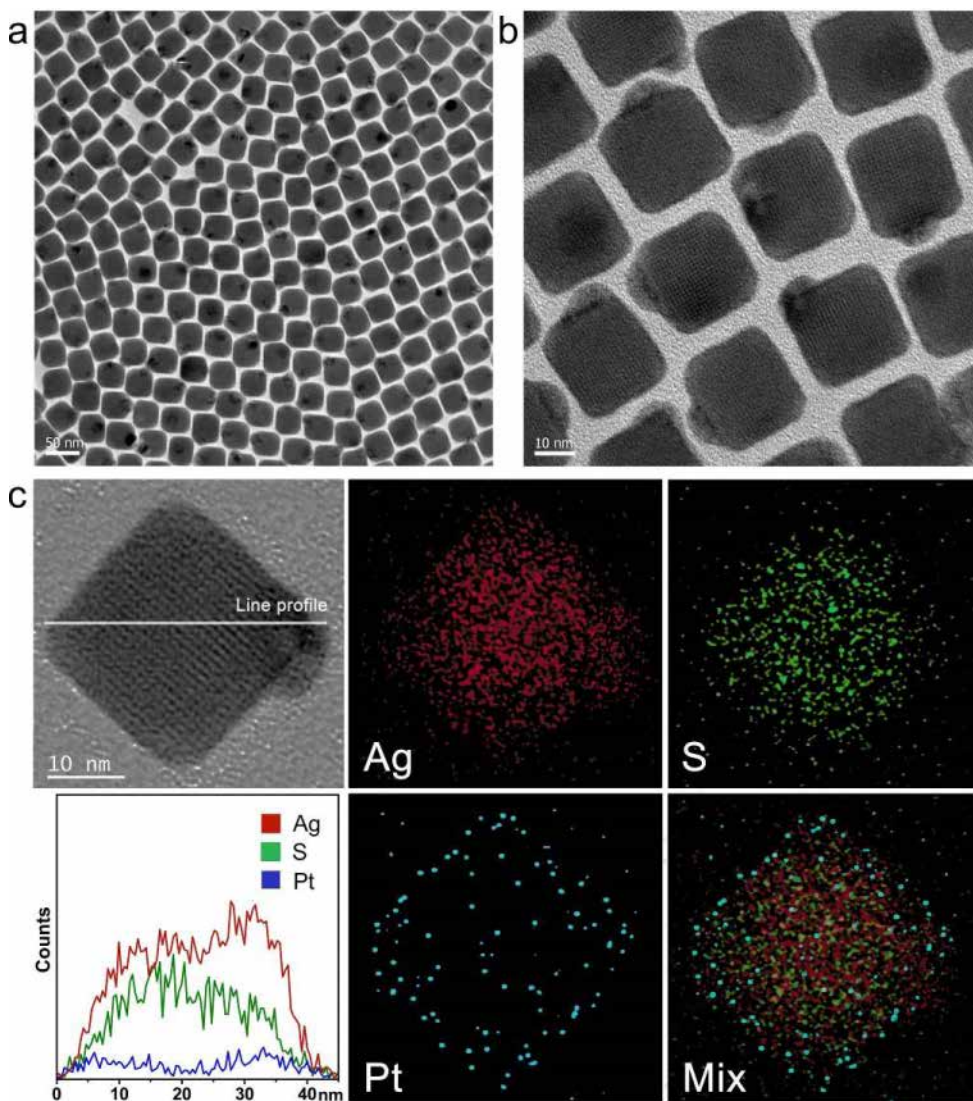


**Figure 4.10.** (a,b) HRTEM images, (c) EDX mapping and line profile results of Ag-Ag<sub>2</sub>S@Pt NPs.

**Table 4.1.** Standard potentials of half-cell reactions involving some metals participating in galvanic replacement/deposition reactions.

<b>Reaction</b>	<b>E<sub>0</sub> vs. SHE (V)</b>
$\text{PdCl}_4^{2-} + 2\text{e}^- \leftrightarrow \text{Pd} + 4\text{Cl}^-$	+0.620
$\text{PtCl}_6^{2-} + 4\text{e}^- \leftrightarrow \text{Pt} + 6\text{Cl}^-$	+0.744
$\text{PtCl}_4^{2-} + 2\text{e}^- \leftrightarrow \text{Pt} + 4\text{Cl}^-$	+0.730
$\text{Ag}^+ + \text{e}^- \leftrightarrow \text{Ag}$	+0.799
$\text{AuCl}_4^- + 3\text{e}^- \leftrightarrow \text{Au} + 4\text{Cl}^-$	+1.002



# Chapter 5: Synthesis and Structure Engineering of

## Cubic Metal-Semiconductor Nanoframes

### 5.1 Introduction

Among various nanomaterials, metal and semiconductor are prominent in electronic, optical and catalytic properties.<sup>42, 45</sup> Metal nanocomponents are featured with high electron mobility, strong EM-field localization capability and high photocatalytic activities,<sup>93, 129</sup> while semiconductor nanocomposites possess unique photoelectronic properties such as temperature-dependent conductivity, photo-induced charge separation and dopability.<sup>130</sup> As a result, metal-semiconductor (M-S) heterojunctions are widely used in many microelectronic and photoelectronic devices, including Schottky diodes,<sup>131</sup> metal-oxide-semiconductor field-effect transistor<sup>132</sup> and gas sensors.<sup>133</sup> With the development of nanotechnology, increasingly stringent boundaries have been placed on composition, dimensionality, symmetry and functionality of metal-semiconductor nanostructures, thus precise engineering of complex heterostructures at the nanoscale is highly desired.

Nanocages and nanoframes have long been of broad interest due to their well-defined primary and secondary structure at the nanoscale, which brings together multiple synergistic effects, such as high surface-to-volume ratio, into one nanostructure.<sup>127-128, 134-139</sup> Precisely controlled nanoframe structures such as Au nanocages, CuS nanocages and Pt-Ni nanoframes have been developed,<sup>127, 140-141</sup> which offers unique physiochemical properties in various energy, catalysis and biological application. However, the synthetic methodologies for such

nanostructures are relatively limited. One important approach is galvanic replacement reaction that deposits noble metal atoms (such as Au and Pt) onto faces of sacrificial metal polyhedrons (such as Ag and Pd), giving rise to a hollow noble metal nanocage.<sup>128, 142</sup> Although most metal pairs with different standard reduction potential can adopt this method, only metal pairs with sufficient low lattice mismatch result in well-defined single-crystalline nanocages. Besides metallic structure, metal oxide<sup>143</sup> and sulfide<sup>144</sup> nanocages can also be synthesized by galvanic replacement reactions and cation exchange reactions.

Another important method is based on the selective etching of metastable components in metallic alloys or other multicomponent structures, resulting in the formation of hollow nanoframes.<sup>134-138, 145-150</sup> For example, metal nanoframes can be fabricated by the co-reduction of multiple metals into a polyhedron, followed by phase segregation and selective etching. One key challenge in the process is the controlled phase segregation to create nanostructures with the desired atoms in the desired positions such as the facet center, edge, or vertex locations of facet-controlled alloy nanoparticles.<sup>151</sup> A successful demonstration of this method is the Pt-Ni alloy system generating a well-defined Pt-Ni nanoframe. To understand the phase segregation process, Oh et al. introduced CO as both reducing agent and surface stabilization agent for the nanoparticle morphological generation.<sup>151</sup> CO selectively protects the <111> of Ni, promoting the Pt segregation along <110> edges, and etching of Ni-rich phase exposed the Pt-rich nanoframes. Recently, Niu et al. further revealed the directional growth and anisotropic phase segregation of Pt by selective chemical etching in various intermediate stages. These synthetic and mechanism studies greatly promoted the development of nanoframe structures and their applications in various catalytic reactions, especially oxygen reduction

reactions.<sup>134-138, 145-150</sup> Although great efforts have been devoted into this field, new synthetic strategies are still highly desired in most material species, especially semiconductor-based nanoframes.

Semiconductors with small bandgap and low biotoxicity are of particular research interest in biology due to the NIR responsive photoelectronic properties.<sup>152</sup> Among them, metal sulfides such as copper sulfide and silver sulfide have been widely used in biological therapies due to their high biocompatibility.<sup>153-155</sup> Silver sulfide is found amongst the most important chalcogenides due to its unique optoelectronic applications, such as infrared detectors,<sup>156</sup> fuel cells<sup>157</sup> and gas sensors.<sup>158</sup> In particular, silver sulfide has a large absorption and a direct band gap of 0.9 to 1.05 eV, which is highly suitable for deep penetration biotherapy in the second NIR window. Moreover, bulk  $\alpha$ -Ag<sub>2</sub>S has been recently found to be ductile under room-temperature, the favorable bandgap and the relatively large carrier mobility make it potentially useful in flexible or wearable devices.<sup>159</sup>

In this chapter, we synthesized Ag-Pt/Ag<sub>2</sub>S metal-semiconductor nanoframes (MSF) with uniform cubic morphology and size (60.2±3.9 nm) in CTAC solution. The introduction of Pt/Ag<sub>2</sub>S heterointerface provided an additional strain source which transformed the Ag-Ag<sub>2</sub>S dimer NP into a more complicated 3D MSF structure. During the one-pot growth, a metal-semiconductor concave nanocube (MSC) was first formed under 95°C, followed by self-etching evolution into a hollow MSF structure. Phase segregation of Pt during the transformation was evidenced by EDX elemental measurements. Moreover, the MSF structure can be tuned from tetrahedron frames to cubic frames with different edge-to-body diameter ratios, simply by altering the Pt/S precursor ratio, indicating high structure tunability.

## **5.2 Experimental section**

### **5.2.1 Materials and instruments**

All chemical reagents were purchased from Sigma-Aldrich and used without further purification. The field emission-scanning electron microscopic (FE-SEM) measurements were conducted on a MERLIN Compact (ZEISS) electron microscope. The transmission electron microscopic (TEM) and Cs-corrected high resolution transmission electron microscopic (HRTEM) characterizations were performed with a JEM-2100F (JEOL) electron microscope and a JEM-ARM200F (JEOL) electron microscope in the National Center for Inter-University Facilities (NCIRF), respectively. The energy-dispersive X-ray spectroscopy (EDX) mapping measurements were performed with a JEM-2100F electron microscope. Powder XRD measurements were performed by a SmartLab (Rigaku, Japan) powder X-ray Diffractometer. The TEM and HRTEM specimens were prepared by dropping a few microliters of concentrated nanoparticle solution on a carbon-coated copper grid followed by drying in vacuum.

### **5.2.2 Synthesis of colloidal Pt/Ag<sub>2</sub>S-Ag nanoframes**

In a typical synthesis, K<sub>2</sub>PtCl<sub>4</sub> (5 mM, 1500 μL) and Na<sub>2</sub>S<sub>2</sub>O<sub>3</sub> (0.1 M, 200 μL) were added into a CTAC solution (80 mM, 25 mL) under gentle stirring (80 rpm). Meanwhile, AgNO<sub>3</sub> (0.1 M, 750 μL) was added to another CTAC solution (80 mM, 25 mL) for 1 min, and then gently poured into the first CTAC mixture. The vial was sealed and kept at 95 °C for 120 min before washing with 1 mM CTAC solution and centrifugating at 5,000 rpm (this procedure was repeated 3 times). The final products were stored in 1 mL of 1 mM CTAC solution before use.

### **5.2.3 Synthesis of Ag<sub>2</sub>S@Pt NPs**

In order to promote the galvanic replace reaction between Ag and Pt, the reaction was conducted at 95°C for 120 min. Typically, 1 mL of the 25 nm Ag-Ag<sub>2</sub>S NPs was centrifuged and redispersed in CTAC solution (50 mM, 10 mL) and stirred under 200 rpm for 15 min. Another CTAC solution (50 mM, 10 mL) was mixed with K<sub>2</sub>PtCl<sub>4</sub> solution (5 mM, 200 μL), and added to the first CTAC solution. The mixture was heated at 95°C for 120 min under 200 rpm stirring. The product was washed with 1 mM CTAC solution by centrifugation under 10,000 rpm (this procedure was repeated 3 times).

### 5.3 Results and Discussions

#### 5.3.1 Structure characterization of MSFs

As shown in **Figure 5.1a**, a well-dispersed colloidal cubic nanoframe structure with a diameter of ~60 nm was obtained via a one-pot aqueous method under mild reaction conditions. The EDX mapping results clearly revealed the presence of Ag, S and Pt in the MSFs (**Figure 5.1c**). All of these elements were distributed over the whole MSF as inferred, indicating a hybrid structure. Interestingly, the MSFs showed a well-defined cubic shape, with an additional sub-NP attached on one corner of the MSF, which has a distinguished contrast in comparison with the MSF edges. High resolution EDX mapping (**Figure 5.1f**) revealed that the sub-NP mainly contains Ag with minimum S and Pt, indicating a metallic Ag sub-NP. Further Cs-HRTEM characterization (**Figure 5.2**) found some characteristic  $\langle 100/004 \rangle$  facets of 4H-Ag, indicating a Ag-Pt/Ag<sub>2</sub>S nanostructure.

Typical  $\langle 022 \rangle$  planes of Ag<sub>2</sub>S was found at the corner of MSF, which is similar to that appeared in cubic structures. More interestingly, cubic phase is not the favorable structure of Ag<sub>2</sub>S because of the low symmetry in its  $\{200\}$  planes. These results indicated that a phase transition of Ag<sub>2</sub>S may be involved in the

growth process. To demonstrate the 3D structure, FE-SEM and TEM titling were employed (**Figure 5.3**). As shown in **Figure 5.3a** and **b**, MSFs under multiple orientations were observed under SEM, clearly displaying the 3D morphologies. It clear showed that one single MSF is composed of eight cube corners and 12 cube edges while the cube body and six faces are hollow. TEM titling images in **Figure 5.3c** matched well with the SEM results, showing a highly crystallized frame structure. The high contrast of the four corners under TEM is resulted from the four vertically standing edges.

To further confirm the 3D structure of MSF and the spatial distribution of Pt, HADDF-STEM measurement was performed (**Figure 5.4a** and **b**). The single-crystalline structure of the nanoframes was clearly observed in **Figure 5.4b**, and some bright spots on the nanoframe surface were found. Quantitative EDX line profile measurement (**Figure 5.4d**) revealed that the highest distribution of Pt was found to be on the outer surface of nanoframe, while the distribution on the inner surface was relatively low. Estimated atomic percentage from EDX spectra showed that the atomic ratio of Ag: S was 64.09: 32.04, which indicated the nanoframe body was  $\text{Ag}_2\text{S}$ . Although Pt only showed a small atomic percentage of 3.87, characteristic Pt peaks were found on EDX spectrum. The chemical states of Pt in the MSFs were further investigated by the X-ray photoelectron spectroscopy (XPS), as shown in **Figure 5.4f**. The XPS Pt 4f spectra of the MSFs can be deconvoluted into two pairs of doublets, in which the doublet at 69.8 eV and 73.2 eV corresponded to zero valent Pt, while the other doublet, corresponded to Pt(II) that may bind to S or O. The high percentage of Pt(II) as indicated by XPS should be attributed to the small size of Pt NPs on the MSF, giving rise to the high ratio of Pt/ $\text{Ag}_2\text{S}$  heterointerface.

### 5.3.2 Structure evolution from MSCs to MSFs

The multi-level complex 3D nanostructure of MSFs indicates that the formation mechanism of MSF cannot be simply explained by either galvanic replacement-induced hollowing or ligand-directed facet selectivity. To investigate the underlying mechanism, we quenched the reaction at 45 min by ice bath to find a metal-semiconductor concave nanocube (MSC). As showed in **Figure 5.5a**, MSCs displayed uniform cubic shape with highly concave faces under SEM. As shown in **Figure 5.5b**, the 3D structure of MSC cannot be easily observed under HRTEM, but the MSC faces showed a lower contrast than its corners due to the difference in structure thickness. Selected area electron diffraction (SAED) showed that the MSC has a single crystalline cubic structure (**Figure 5.5c**), which is very similar to that of the Ag-Ag<sub>2</sub>S NPs as described in Chapter 4. To understand the elemental distribution in MSC, EDX line profile measurement was performed (**Figure 5.5d**). The distribution of Ag and S matched well with the concave structure, showing a lower distribution in the center. Importantly, comparing with the Pt distribution in MSF (**Figure 5.4d**), it was found that Pt has the highest distribution in the concave faces rather than the edges. It indicates that Pt may go through phase segregation during the transformation from MSC to MSF.

In order to investigate the possible transformation mechanism from MSC to MSF, air-based in-situ HRTEM measurements were carried out (**Figure 5.5e**). Under TEM observation, the MSC went through five stages to become a MSF. In the stage I, MSC does not show observable change which can be attributed to the necessary period for temperature increase. Next, the contrast in the MSC face started to transform in the stage II, in which a phase with high contrast began to segregate from the face center to the edges, leaving a lower contrast in the face

center. In stage III, MSC started to become hollow by the formation of a small hole in the concave face, indicating a self-etching process. After that (stage IV), the size of the hole further expanded, showing an accumulation of high contrast phase at the hole boundaries. Such boundary-driven segregation further expanded, approaching a fully opened face (stage V). In the final stage (stage VI), the nanostructure went through structure reorganization and a sub-NP was found to be formed on one of the corner, matching perfectly with the Ag sub-NP in the MSF structure. It is reasonable to deduce that the higher distribution of Pt on the outer surface of MSFs (**Figure 5.4d**) was a result of phase segregation and structure reorganization.

To figure out the role of Pt in the self-etching transformation from MSC to MSF, we performed the galvanic replacement reaction between Pt and Ag-Ag<sub>2</sub>S at 95°C. As shown in **Figure 5.6a**, the deposition of Pt induced the self-etching effect in Ag<sub>2</sub>S under 95°C. Within 30 min, etching of Ag<sub>2</sub>S NP began to occur on the surface (**Figure 5.6b, c**), and a shift of the diffraction peaks to higher values of the diffraction angle was found (**Figure 5.6h**). The center of the Ag<sub>2</sub>S NP became hollow after 60 min (**Figure 5.6d, e**) and the hollow region expanded further after 180 min (**Figure 5.6f, g**). Meanwhile, the diffraction peaks shifted to lower values of the diffraction angle, gradually recovered to a similar angle with Ag-Ag<sub>2</sub>S NP (**Figure 5.6h**). Further prolonging of reaction time cannot fully etch all the Ag<sub>2</sub>S in the structure, indicating a self-limiting process. The shifting of diffraction peaks during the reaction suggested that such self-etching effect may be driven by the change of lattice stress, which was a result of heterointerface evolution. Similarly, the phase segregation of Pt in MSC may be responsible for the self-etching process in the transformation from MSC to MSF.



### 5.3.3 Structure tunability of MSFs

The unique synthetic strategy of MSFs offers relatively high structure tunability on the nanoframe structure. By tuning the Pt/S precursor ratio, we successfully altered the nanoframe shape and edge thickness as shown in **Figure 5.7**. As Pt/S precursor ratio increased, the shape of MSF changed from a tetrahedron with one  $\langle 200 \rangle$  face (**Figure 5.7a**) to a cubic shape with four  $\langle 200 \rangle$  faces (**Figure 5.7b**). The cubic shape remained unchanged upon further increase of Pt/S precursor ratio, but the edge-to-body diameter ratio gradually decrease, leading to a MSF with ultrathin edges (**Figure 5.7d**).

### 5.4 Conclusion

In this work, a one-pot synthetic approach for cubic Ag-Pt/Ag<sub>2</sub>S metal-semiconductor nanoframe (MSF) was developed by introducing the Pt/Ag<sub>2</sub>S heterointerface as an additional strain source in the HSE strategy. It led to the formation of highly concave Pt/Ag/Ag<sub>2</sub>S metal-semiconductor nanocube (MSC), which further transformed into a hollow MSF by self-etching effect. Phase segregation of Pt during the transformation was evidenced by comparing the elemental distribution of MSC and MSF in EDX line profile, suggesting the self-etching effect may be a result of HSE process induced by the Pt segregation. Moreover, the MSF structure can be tuned from tetrahedron frames to cubic frames with different edge-to-body diameter ratios, simply by altering the Pt/S precursor ratio, indicating high structure tunability. The high surface-to-volume ratio of nanoframe structures, the unique photoelectronic, biocompatibility and second NIR absorption of Ag<sub>2</sub>S, and the wide application of metal-semiconductor heterointerface indicate the great potential for these MSF nanostructures in

catalysis, sensing and biomedical applications, especially deep penetration biotherapies.

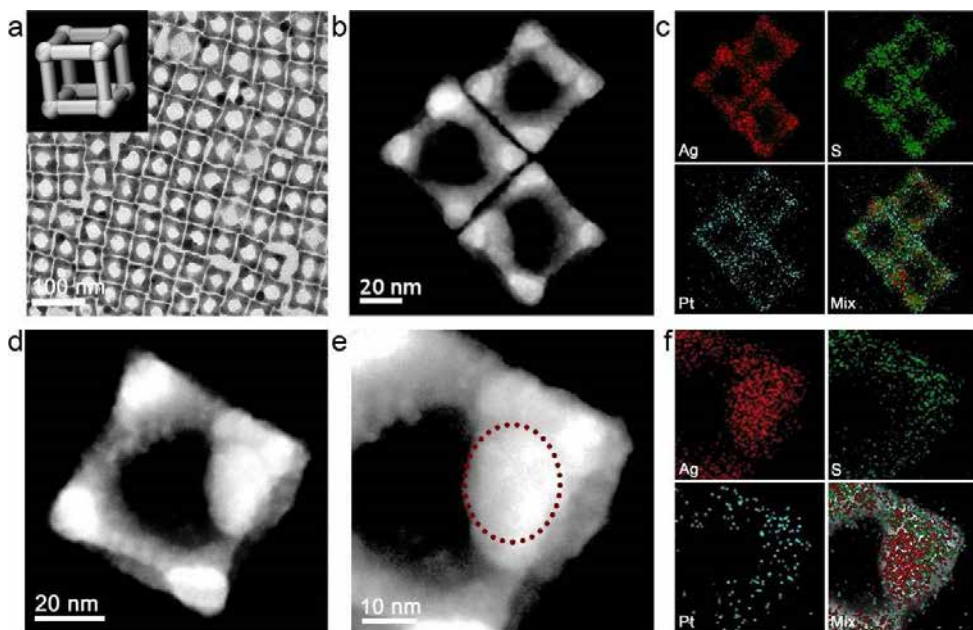


**Figure 5.1.** (a) TEM image, (b) HADDF image and (c) EDX mapping images of the MSFs. (d) Low magnification and (e, f) high magnification Cs-HRTEM images of MSFs.

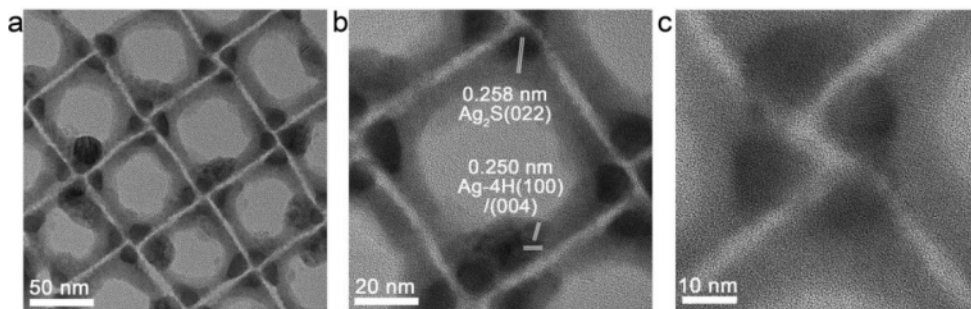


**Figure 5.2.** (a) Cs-HRTEM images of MSFs. High magnification images showing lattice structures of (b) a single MSF and (c) the featured corners.

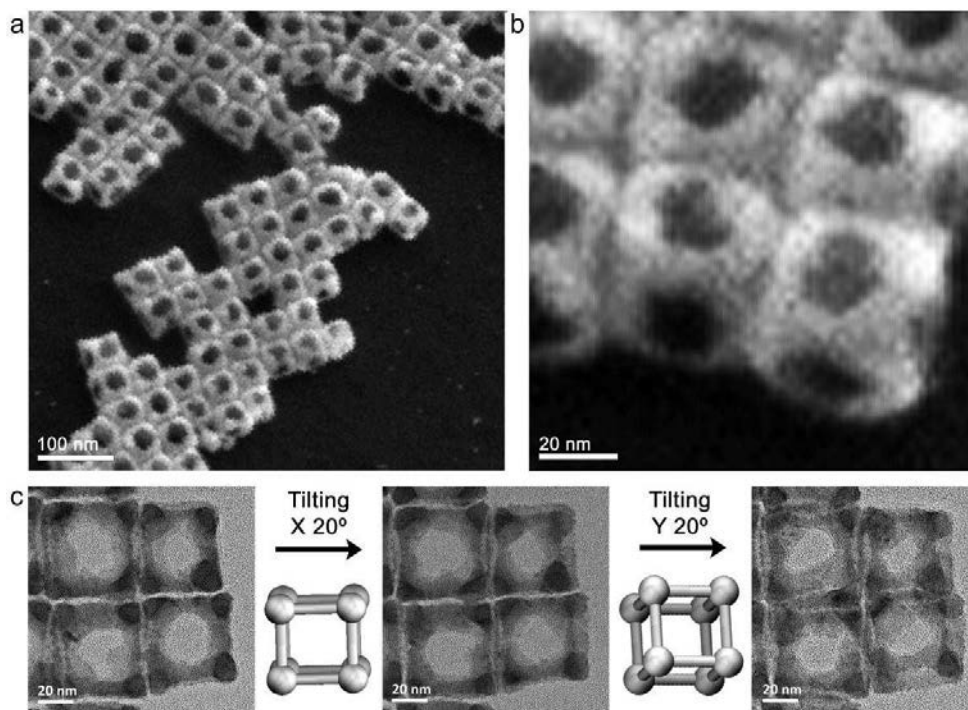


**Figure 5.3.** (a) Low magnification and (b) high magnification SEM images showing the 3D structure of MSFs. (c) Tilted TEM images showing the 3D geometry of MSFs at different orientations.

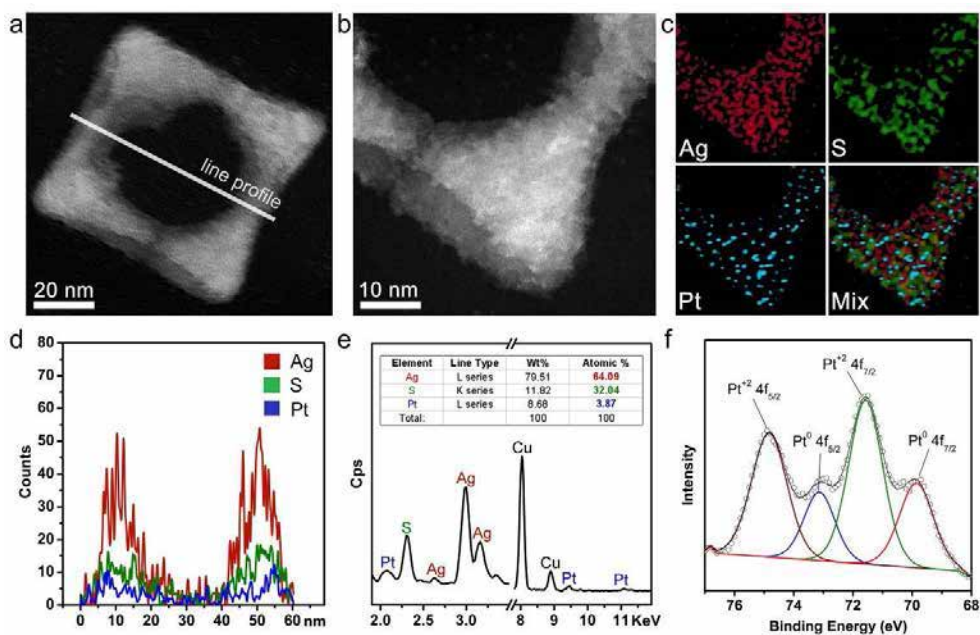


**Figure 5.4.** (a, b) A single MSF under HAADF-STEM mode, as well as (c) the EDX mapping images, (d) EDX line profile and (e) EDX spectrum showing elemental compositions. (f) XPS spectrum of Pt<sub>4f</sub> in MSFs.

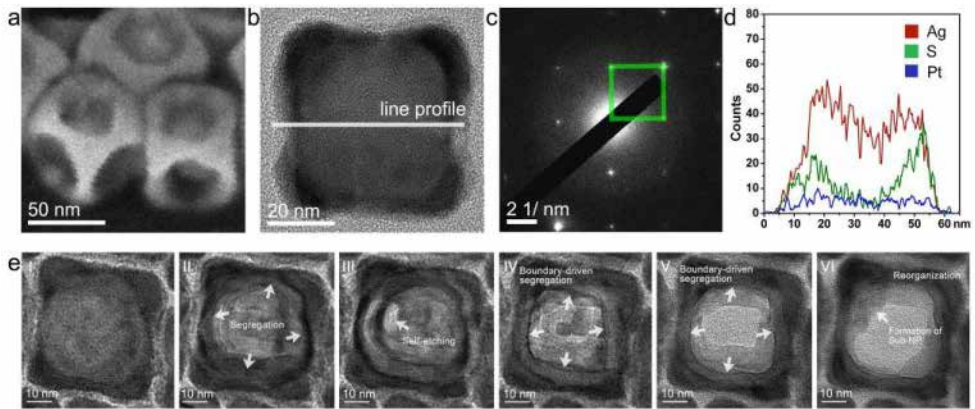


**Figure 5.5.** (a) High resolution SEM image of MSCs. (b) HRTEM image and (c) corresponding SAED pattern and (d) EDX line profile results of a single MSC. (e) Air-based in-situ TEM observations of the transformation from a MSC to a MSF.

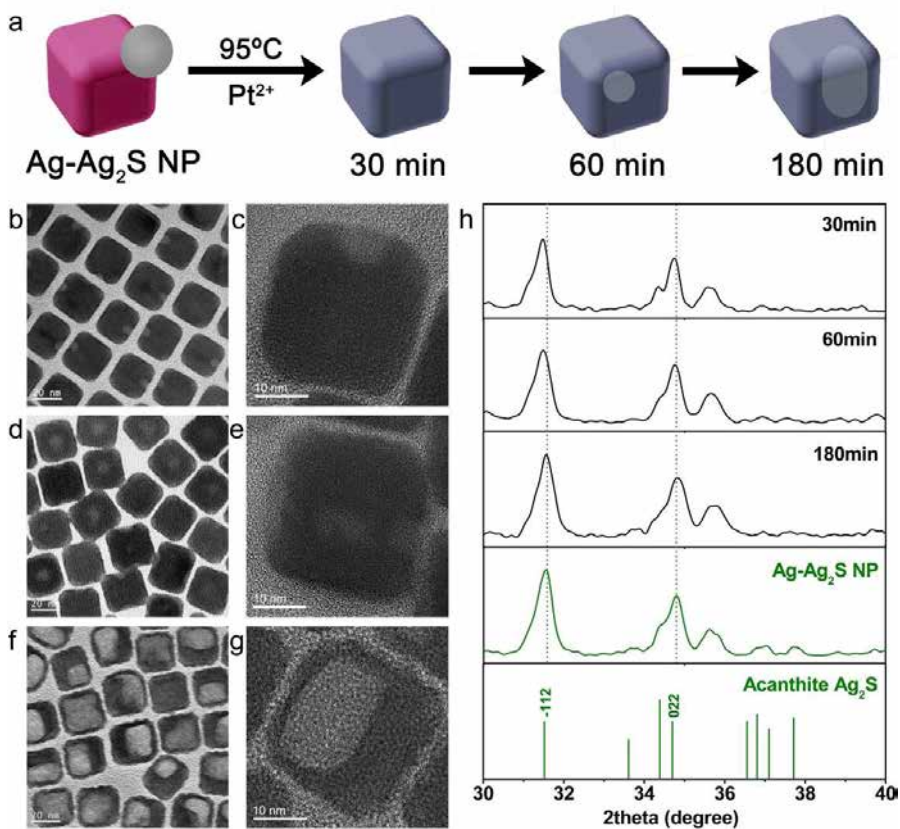


**Figure 5.6.** (a) Schematic illustration of the evolution of  $\text{Ag}_2\text{S}@\text{Pt}$  NPs from stepwise galvanic replacement reaction between Ag on  $\text{Ag-Ag}_2\text{S}$  NP and Pt under  $95^\circ\text{C}$ . TEM and Cs-HRTEM of 30 min (b, c), 60 min (d, e) and 180 min (f, g) products. (h) XRD patterns of the  $\text{Ag}_2\text{S}@\text{Pt}$  NPs under various reaction time.



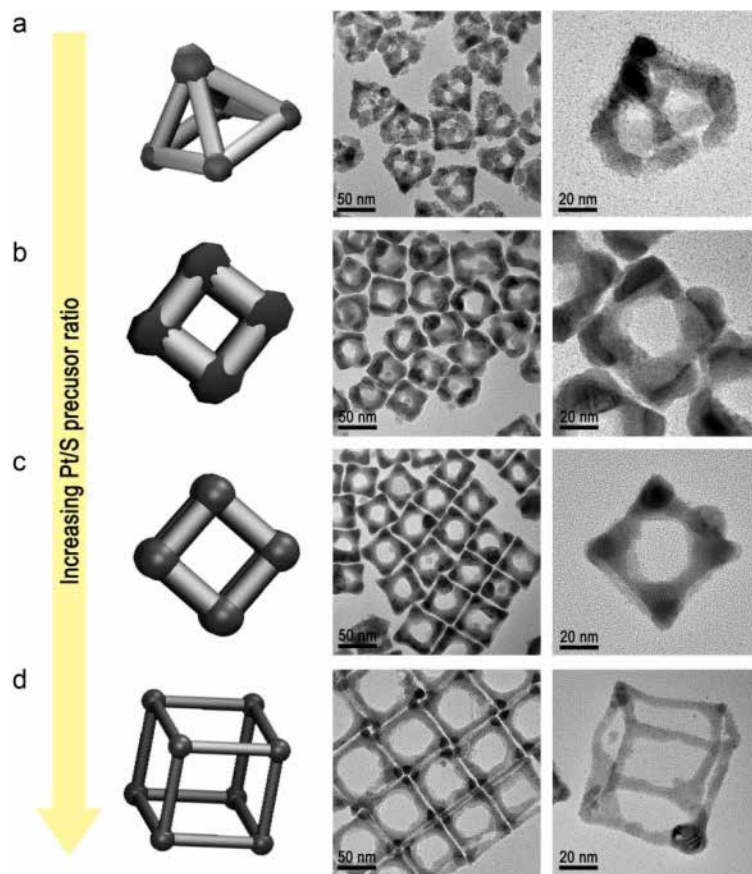


**Figure 5.7.** Schematic illustration and TEM images of precisely-engineered MSFs by increasing the ratio of  $\text{K}_2\text{PtCl}_4$  to  $\text{Na}_2\text{S}_2\text{O}_3$ .

## Bibliography

1. Wang, Y.; He, J.; Liu, C.; Chong, W. H.; Chen, H., Thermodynamics versus kinetics in nanosynthesis. *Angewandte Chemie* **2015**, *54* (7), 2022-51.
2. Xia, Y.; Xia, X.; Peng, H.-C., Shape-Controlled Synthesis of Colloidal Metal Nanocrystals: Thermodynamic versus Kinetic Products. *J Am Chem Soc* **2015**, *137* (25), 7947-7966.
3. O'Brien, M. N.; Jones, M. R.; Brown, K. A.; Mirkin, C. A., Universal Noble Metal Nanoparticle Seeds Realized Through Iterative Reductive Growth and Oxidative Dissolution Reactions. *J Am Chem Soc* **2014**, *136* (21), 7603-7606.
4. Sanchez-Iglesias, A.; Winckelmans, N.; Altantzis, T.; Bals, S.; Grzelczak, M.; Liz-Marzan, L. M., High-Yield Seeded Growth of Monodisperse Pentatwinned Gold Nanoparticles through Thermally Induced Seed Twinning. *J Am Chem Soc* **2017**, *139* (1), 107-110.
5. Kwon, S. G.; Krylova, G.; Phillips, P. J.; Klie, R. F.; Chattopadhyay, S.; Shibata, T.; Bunel, E. E.; Liu, Y. Z.; Prakapenka, V. B.; Lee, B.; Shevchenko, E. V., Heterogeneous nucleation and shape transformation of multicomponent metallic nanostructures. *Nat Mater* **2015**, *14* (2), 215-223.
6. Chen, P. C.; Liu, X. L.; Hedrick, J. L.; Xie, Z.; Wang, S. Z.; Lin, Q. Y.; Hersam, M. C.; Dravid, V. P.; Mirkin, C. A., Polyelemental nanoparticle libraries. *Science* **2016**, *352* (6293), 1565-1569.
7. Zhang, J.; Tang, Y.; Lee, K.; Ouyang, M., Nonepitaxial growth of hybrid core-shell nanostructures with large lattice mismatches. *Science* **2010**, *327* (5973), 1634-8.

8. Buck, M. R.; Bondi, J. F.; Schaak, R. E., A total-synthesis framework for the construction of high-order colloidal hybrid nanoparticles. *Nat Chem* **2012**, *4* (1), 37-44.
9. Hodges, J. M.; Biacchi, A. J.; Schaak, R. E., Ternary hybrid nanoparticle isomers: directing the nucleation of Ag on Pt-Fe<sub>3</sub>O<sub>4</sub> using a solid-state protecting group. *ACS nano* **2014**, *8* (1), 1047-55.
10. Lee, J. H.; Kim, G. H.; Nam, J. M., Directional Synthesis and Assembly of Bimetallic Nanosnowmen with DNA. *J Am Chem Soc* **2012**, *134* (12), 5456-5459.
11. Wang, Z. X.; He, B. W.; Xu, G. F.; Wang, G. J.; Wang, J. Y.; Feng, Y. H.; Su, D. M.; Chen, B.; Li, H.; Wu, Z. H.; Zhang, H.; Shao, L.; Chen, H. Y., Transformable masks for colloidal nanosynthesis. *Nat Commun* **2018**, *9*.
12. Mubeen, S.; Lee, J.; Singh, N.; Kramer, S.; Stucky, G. D.; Moskovits, M., An autonomous photosynthetic device in which all charge carriers derive from surface plasmons. *Nat Nanotechnol* **2013**, *8* (4), 247-251.
13. Kumarasinghe, C. S.; Premaratne, M.; Bao, Q.; Agrawal, G. P., Theoretical analysis of hot electron dynamics in nanorods. *Sci. Rep.* **2015**, *5*, 12140.
14. Giugni, A.; Torre, B.; Toma, A.; Francardi, M.; Malerba, M.; Alabastri, A.; Zaccaria, R. P.; Stockman, M. I.; Di Fabrizio, E., Hot-electron nanoscopy using adiabatic compression of surface plasmons. *Nat Nanotechnol* **2013**, *8* (11), 845-852.
15. Fang, Y.; Li, Y.; Xu, H.; Sun, M., Ascertaining p,p'-Dimercaptoazobenzene Produced from p-Aminothiophenol by Selective Catalytic Coupling Reaction on Silver Nanoparticles. *Langmuir* **2010**, *26* (11), 7737-7746.
16. Zhao, L.-B.; Huang, Y.-F.; Liu, X.-M.; Anema, J. R.; Wu, D.-Y.; Ren, B.; Tian, Z.-Q., A DFT study on photoinduced surface catalytic coupling reactions on

nanostructured silver: selective formation of azobenzene derivatives from para-substituted nitrobenzene and aniline. *Phys. Chem. Chem. Phys.* **2012**, *14* (37), 12919-12929.

17. Xu, P.; Kang, L.; Mack, N. H.; Schanze, K. S.; Han, X.; Wang, H.-L., Mechanistic understanding of surface plasmon assisted catalysis on a single particle: cyclic redox of 4-aminothiophenol. *Sci. Rep.* **2013**, *3*, 2997.

18. Wu, B.; Liu, D.; Mubeen, S.; Chuong, T. T.; Moskovits, M.; Stucky, G. D., Anisotropic Growth of TiO<sub>2</sub> onto Gold Nanorods for Plasmon-Enhanced Hydrogen Production from Water Reduction. *J. Am. Chem. Soc.* **2016**, *138* (4), 1114-1117.

19. Buck, M. R.; Schaak, R. E., Emerging Strategies for the Total Synthesis of Inorganic Nanostructures. *Angew Chem Int Edit* **2013**, *52* (24), 6154-6178.

20. Tiwari, J. N.; Sultan, S.; Myung, C. W.; Yoon, T.; Li, N.; Ha, M.; Harzandi, A. M.; Park, H. J.; Kim, D. Y.; Chandrasekaran, S. S.; Lee, W. G.; Vij, V.; Kang, H.; Shin, T. J.; Shin, H. S.; Lee, G.; Lee, Z.; Kim, K. S., Multicomponent electrocatalyst with ultralow Pt loading and high hydrogen evolution activity. *Nature Energy* **2018**.

21. Kwon, S. G.; Krylova, G.; Phillips, P. J.; Klie, R. F.; Chattopadhyay, S.; Shibata, T.; Bunel, E. E.; Liu, Y.; Prakapenka, V. B.; Lee, B.; Shevchenko, E. V., Heterogeneous nucleation and shape transformation of multicomponent metallic nanostructures. *Nat Mater* **2014**, *14*, 215.

22. Xia, Y. N.; Xia, X. H.; Peng, H. C., Shape-Controlled Synthesis of Colloidal Metal Nanocrystals: Thermodynamic versus Kinetic Products. *J Am Chem Soc* **2015**, *137* (25), 7947-7966.

23. Xia, Y. N.; Gilroy, K. D.; Peng, H. C.; Xia, X. H., Seed-Mediated Growth of Colloidal Metal Nanocrystals. *Angew Chem Int Edit* **2017**, *56* (1), 60-95.
24. Hofmeister, H., Shape variations and anisotropic growth of multiply twinned nanoparticles. *Z Kristallogr* **2009**, *224* (11), 528-538.
25. Wang, Z. L., Transmission electron microscopy of shape-controlled nanocrystals and their assemblies. *J Phy Chem B* **2000**, *104* (6), 1153-1175.
26. Zhang, Q. B.; Xie, J. P.; Yu, Y.; Yang, J. H.; Lee, J. Y., Tuning the Crystallinity of Au Nanoparticles. *Small* **2010**, *6* (4), 523-527.
27. Schlenoff, J. B.; Li, M.; Ly, H., Stability and Self-Exchange in Alkanethiol Monolayers. *J Am Chem Soc* **1995**, *117* (50), 12528-12536.
28. Lamer, V. K.; Dinegar, R. H., Theory, Production and Mechanism of Formation of Monodispersed Hydrosols. *J Am Chem Soc* **1950**, *72* (11), 4847-4854.
29. Murray, C. B.; Norris, D. J.; Bawendi, M. G., Synthesis and Characterization of Nearly Monodisperse Cde (E = S, Se, Te) Semiconductor Nanocrystallites. *J Am Chem Soc* **1993**, *115* (19), 8706-8715.
30. Faraday, M., X. The Bakerian Lecture. —Experimental relations of gold (and other metals) to light. *Philosophical Transactions of the Royal Society of London* **1857**, *147*, 145-181.
31. One-dimensional dislocations. I. Static theory. *Proceedings of the Royal Society of London. Series A. Mathematical and Physical Sciences* **1949**, *198* (1053), 205-216.
32. Eaglesham, D. J.; Cerullo, M., Dislocation-free Stranski-Krastanow growth of Ge on Si(100). *Physical Review Letters* **1990**, *64* (16), 1943-1946.

33. Chen, P. C.; Du, J. S. S.; Meckes, B.; Huang, L. L.; Xie, Z.; Hedrick, J. L.; Dravid, V. P.; Mirkin, C. A., Structural Evolution of Three-Component Nanoparticles in Polymer Nanoreactors. *J Am Chem Soc* **2017**, *139* (29), 9876-9884.
34. Shahjamali, M. M.; Zhou, Y.; Zaraee, N.; Xue, C.; Wu, J. S.; Large, N.; McGuirk, C. M.; Boey, F.; Dravid, V.; Cui, Z. F.; Schatz, G. C.; Mirkin, C. A., Ag-Ag<sub>2</sub>S Hybrid Nanoprisms: Structural versus Plasmonic Evolution. *ACS nano* **2016**, *10* (5), 5362-5373.
35. Van Swygenhoven, H.; Derlet, P. M.; Froseth, A. G., Stacking fault energies and slip in nanocrystalline metals. *Nat Mater* **2004**, *3* (6), 399-403.
36. Lim, B.; Jiang, M. J.; Camargo, P. H. C.; Cho, E. C.; Tao, J.; Lu, X. M.; Zhu, Y. M.; Xia, Y. N., Pd-Pt Bimetallic Nanodendrites with High Activity for Oxygen Reduction. *Science* **2009**, *324* (5932), 1302-1305.
37. Wang, H.; Chen, L.; Feng, Y.; Chen, H., Exploiting Core-Shell Synergy for Nanosynthesis and Mechanistic Investigation. *ACC CHEM RES* **2013**, *46* (7), 1636-1646.
38. Personick, M. L.; Langille, M. R.; Zhang, J.; Mirkin, C. A., Shape Control of Gold Nanoparticles by Silver Underpotential Deposition. *Nano Lett* **2011**, *11* (8), 3394-3398.
39. Ding, K.; Cullen, D. A.; Zhang, L.; Cao, Z.; Roy, A. D.; Ivanov, I. N.; Cao, D., A general synthesis approach for supported bimetallic nanoparticles via surface inorganometallic chemistry. *Science* **2018**, *362* (6414), 560-564.
40. Liu, X.; Zhang, F.; Jing, X.; Pan, M.; Liu, P.; Li, W.; Zhu, B.; Li, J.; Chen, H.; Wang, L.; Lin, J.; Liu, Y.; Zhao, D.; Yan, H.; Fan, C., Complex silica composite nanomaterials templated with DNA origami. *Nature* **2018**, *559* (7715), 593-598.

41. Nicolaou, K. C.; Vourloumis, D.; Winssinger, N.; Baran, P. S., The art and science of total synthesis at the dawn of the twenty-first century. *Angew Chem Int Edit* **2000**, *39* (1), 44-122.
42. Lee, J. H.; You, M. H.; Kim, G. H.; Nam, J. M., Plasmonic Nanosnowmen with a Conductive Junction as Highly Tunable Nanoantenna Structures and Sensitive, Quantitative and Multiplexable Surface-Enhanced Raman Scattering Probes. *Nano Lett* **2014**, *14* (11), 6217-6225.
43. Wang, F.; Li, C. H.; Chen, H. J.; Jiang, R. B.; Sun, L. D.; Li, Q.; Wang, J. F.; Yu, J. C.; Yan, C. H., Plasmonic Harvesting of Light Energy for Suzuki Coupling Reactions. *J Am Chem Soc* **2013**, *135* (15), 5588-5601.
44. Huang, H.; Zhang, L.; Lv, Z. H.; Long, R.; Zhang, C.; Ling, Y.; Wei, K. C.; Wang, C. M.; Chen, L.; Li, Z. Y.; Zhang, Q.; Luo, Y.; Xiong, Y. J., Unraveling Surface Plasmon Decay in Core-Shell Nanostructures toward Broadband Light-Driven Catalytic Organic Synthesis. *J Am Chem Soc* **2016**, *138* (21), 6822-6828.
45. Schuller, J. A.; Barnard, E. S.; Cai, W. S.; Jun, Y. C.; White, J. S.; Brongersma, M. L., Plasmonics for extreme light concentration and manipulation. *Nat Mater* **2010**, *9* (3), 193-204.
46. Kumarasinghe, C. S.; Premaratne, M.; Bao, Q. L.; Agrawal, G. P., Theoretical analysis of hot electron dynamics in nanorods. *Sci Rep-Uk* **2015**, *5*.
47. Osawa, M.; Matsuda, N.; Yoshii, K.; Uchida, I., CHARGE-TRANSFER RESONANCE RAMAN PROCESS IN SURFACE-ENHANCED RAMAN-SCATTERING FROM P-AMINOTHIOPHENOL ADSORBED ON SILVER - HERZBERG-TELLER CONTRIBUTION. *J. Phys. Chem.* **1994**, *98* (48), 12702-12707.

48. Wang, J.; Ando, R. A.; Camargo, P. H. C., Controlling the Selectivity of the Surface Plasmon Resonance Mediated Oxidation of p-Aminothiophenol on Au Nanoparticles by Charge Transfer from UV-excited TiO<sub>2</sub>. *Angew. Chem.-Int. Edit.* **2015**, *54* (23), 6909-6912.
49. Yan, X.; Wang, L.; Tan, X.; Tian, B.; Zhang, J., Surface-Enhanced Raman Spectroscopy Assisted by Radical Capturer for Tracking of Plasmon-Driven Redox Reaction. *Sci. Rep.* **2016**, *6*, 30193.
50. Huang, W.; Jing, Q.; Du, Y.; Zhang, B.; Meng, X.; Sun, M.; Schanze, K. S.; Gao, H.; Xu, P., An in situ SERS study of substrate-dependent surface plasmon induced aromatic nitration. *J. Mater. Chem. C* **2015**, *3* (20), 5285-5291.
51. Kumar, N.; Stephanidis, B.; Zenobi, R.; Wain, A. J.; Roy, D., Nanoscale mapping of catalytic activity using tip-enhanced Raman spectroscopy. *Nanoscale* **2015**, *7* (16), 7133-7137.
52. Ding, Q.; Shi, Y.; Chen, M.; Li, H.; Yang, X.; Qu, Y.; Liang, W.; Sun, M., Ultrafast Dynamics of Plasmon-Exciton Interaction of Ag Nanowire-Graphene Hybrids for Surface Catalytic Reactions. *Sci. Rep.* **2016**, *6*, 32724.
53. Dai, Z.; Xiao, X.; Wu, W.; Zhang, Y.; Liao, L.; Guo, S.; Ying, J.; Shan, C.; Sun, M.; Jiang, C., Plasmon-driven reaction controlled by the number of graphene layers and localized surface plasmon distribution during optical excitation. *Light-Sci. Appl.* **2015**, *4*, e342.
54. Dong, B.; Fang, Y.; Chen, X.; Xu, H.; Sun, M., Substrate-, Wavelength-, and Time-Dependent Plasmon-Assisted Surface Catalysis Reaction of 4-Nitrobenzenethiol Dimerizing to p,p'-Dimercaptoazobenzene on Au, Ag, and Cu Films. *Langmuir* **2011**, *27* (17), 10677-10682.



55. Yang, Y.; Wang, S.; Zhang, Z.; Huang, Y.; Chen, G.; Wei, H.; Wen, W., Selective plasmon driven surface catalysis in metal triangular nanoplate-molecule-film sandwich structure. *Chem. Phys. Lett.* **2015**, *639*, 47-51.
56. Tang, X.; Cai, W.; Yang, L.; Liu, J., Monitoring plasmon-driven surface catalyzed reactions in situ using time-dependent surface-enhanced Raman spectroscopy on single particles of hierarchical peony-like silver microflowers. *Nanoscale* **2014**, *6* (15), 8612-8616.
57. Kang, L.; Han, X.; Chu, J.; Xiong, J.; He, X.; Wang, H.-L.; Xu, P., In Situ Surface-Enhanced Raman Spectroscopy Study of Plasmon-Driven Catalytic Reactions of 4-Nitrothiophenol under a Controlled Atmosphere. *ChemCatChem* **2015**, *7* (6), 1004-1010.
58. Dai, Z.; Xiao, X.; Zhang, Y.; Ren, F.; Wu, W.; Zhang, S.; Zhou, J.; Mei, F.; Jiang, C., In situ Raman scattering study on a controllable plasmon-driven surface catalysis reaction on Ag nanoparticle arrays. *Nanotechnology* **2012**, *23* (33), 335701.
59. van Schrojenstein Lantman, E. M.; Deckert-Gaudig, T.; Mank, A. J. G.; Deckert, V.; Weckhuysen, B. M., Catalytic processes monitored at the nanoscale with tip-enhanced Raman spectroscopy. *Nat. Nanotechnol.* **2012**, *7* (9), 583-586.
60. Sun, M.; Zhang, Z.; Zheng, H.; Xu, H., In-situ plasmon-driven chemical reactions revealed by high vacuum tip-enhanced Raman spectroscopy. *Sci. Rep.* **2012**, *2*, 647.
61. Zhang, Z.; Chen, L.; Sun, M.; Ruan, P.; Zheng, H.; Xu, H., Insights into the nature of plasmon-driven catalytic reactions revealed by HV-TERS. *Nanoscale* **2013**, *5* (8), 3249-3252.

62. Zhang, Z.; Sun, M.; Ruan, P.; Zheng, H.; Xu, H., Electric field gradient quadrupole Raman modes observed in plasmon-driven catalytic reactions revealed by HV-TERS. *Nanoscale* **2013**, *5* (10), 4151-4155.
63. Kang, L.; Xu, P.; Zhang, B.; Tsai, H.; Han, X.; Wang, H.-L., Laser wavelength- and power-dependent plasmon-driven chemical reactions monitored using single particle surface enhanced Raman spectroscopy. *Chem. Commun.* **2013**, *49* (33), 3389-3391.
64. Zhang, X.; Wang, P.; Zhang, Z.; Fang, Y.; Sun, M., Plasmon-driven sequential chemical reactions in an aqueous environment. *Sci. Rep.* **2014**, *4*, 5407.
65. Kim, K.; Choi, J.-Y.; Shin, K. S., Photoreduction of 4-Nitrobenzenethiol on Au by Hot Electrons Plasmonically Generated from Ag Nanoparticles: Gap-Mode Surface-Enhanced Raman Scattering Observation. *J. Phys. Chem. C* **2015**, *119* (9), 5187-5194.
66. Wang, S.; Wang, H.; Liu, T.; Huang, Y.; Chen, G.; Wei, H.; Su, X.; Zeng, X.; Xia, Z.; Wen, W.; Sun, M., Ascertaining Plasmonic Hot Electrons Generation from Plasmon Decay in Hybrid Plasmonic Modes. *Plasmonics* **2016**, *11* (3), 909-915.
67. Zhang, Z.; Deckert-Gaudig, T.; Singh, P.; Deckert, V., Single molecule level plasmonic catalysis - a dilution study of p-nitrothiophenol on gold dimers. *Chem. Commun.* **2015**, *51* (15), 3069-3072.
68. Tian, Y.; Tatsuma, T., Plasmon-induced photoelectrochemistry at metal nanoparticles supported on nanoporous TiO<sub>2</sub>. *Chem. Commun.* **2004**, (16), 1810-1811.
69. Tian, Y.; Tatsuma, T., Mechanisms and applications of plasmon-induced charge separation at TiO<sub>2</sub> films loaded with gold nanoparticles. *J. Am. Chem. Soc.* **2005**, *127* (20), 7632-7637.

70. Fujishima, A.; Honda, K., Electrochemical Photolysis of Water at a Semiconductor Electrode. *Nature* **1972**, *238* (5358), 37-+.
71. Zhang, X. Y.; Zheng, Y. H.; Liu, X.; Lu, W.; Dai, J. Y.; Lei, D. Y.; MacFarlane, D. R., Hierarchical Porous Plasmonic Metamaterials for Reproducible Ultrasensitive Surface-Enhanced Raman Spectroscopy. *Adv Mater* **2015**, *27* (6), 1090-1096.
72. Qian, K.; Sweeny, B. C.; Johnston-Peck, A. C.; Niu, W.; Graham, J. O.; DuChene, J. S.; Qiu, J.; Wang, Y.-C.; Engelhard, M. H.; Su, D.; Stach, E. A.; Wei, W. D., Surface Plasmon-Driven Water Reduction: Gold Nanoparticle Size Matters. *J Am Chem Soc* **2014**, *136* (28), 9842-9845.
73. Sousa-Castillo, A.; Comesana-Hermo, M.; Rodriguez-Gonzalez, B.; Perez-Lorenzo, M.; Wang, Z. M.; Kong, X. T.; Govorov, A. O.; Correa-Duarte, M. A., Boosting Hot Electron-Driven Photocatalysis through Anisotropic Plasmonic Nanoparticles with Hot Spots in Au-TiO<sub>2</sub> Nanoarchitectures. *J Phys Chem C* **2016**, *120* (21), 11690-11699.
74. Long, R.; Rao, Z. L.; Mao, K. K.; Li, Y.; Zhang, C.; Liu, Q. L.; Wang, C. M.; Li, Z. Y.; Wu, X. J.; Xiong, Y. J., Efficient Coupling of Solar Energy to Catalytic Hydrogenation by Using Well-Designed Palladium Nanostructures. *Angew Chem Int Edit* **2015**, *54* (8), 2425-2430.
75. Zhang, J.; Jin, X.; Morales-Guzman, P. I.; Yu, X.; Liu, H.; Zhang, H.; Razzari, L.; Claverie, J. P., Engineering the Absorption and Field Enhancement Properties of Au-TiO<sub>2</sub> Nanohybrids via Whispering Gallery Mode Resonances for Photocatalytic Water Splitting. *ACS nano* **2016**, *10* (4), 4496-4503.
76. Nan, F.; Xie, F. M.; Liang, S.; Ma, L.; Yang, D. J.; Liu, X. L.; Wang, J. H.; Cheng, Z. Q.; Yu, X. F.; Zhou, L.; Wang, Q. Q.; Zeng, J., Growth of

metal-semiconductor core-multishell nanorods with optimized field confinement and nonlinear enhancement. *Nanoscale* **2016**, *8* (23), 11969-11975.

77. Wang, Y. W.; He, J. T.; Liu, C. C.; Chong, W. H.; Chen, H. Y., Thermodynamics versus Kinetics in Nanosynthesis. *Angew Chem Int Edit* **2015**, *54* (7), 2022-2051.

78. Warner, D. H.; Curtin, W. A.; Qu, S., Rate dependence of crack-tip processes predicts twinning trends in f.c.c. metals. *Nat Mater* **2007**, *6* (11), 876-881.

79. Wang, J. W.; Zeng, Z.; Weinberger, C. R.; Zhang, Z.; Zhu, T.; Mao, S. X., In situ atomic-scale observation of twinning-dominated deformation in nanoscale body-centred cubic tungsten. *Nat Mater* **2015**, *14* (6), 594-600.

80. Tao, F.; Tang, Y., HETEROGENEOUS CATALYSIS More than skimming the surface. *Nat. Chem.* **2016**, *8* (10), 902-903.

81. Matsubu, J. C.; Zhang, S.; DeRita, L.; Marinkovic, N. S.; Chen, J. G.; Graham, G. W.; Pan, X.; Christopher, P., Adsorbate-mediated strong metal-support interactions in oxide-supported Rh catalysts. *Nat. Chem.* **2016**, doi:10.1038/nchem.2607.

82. Sun, Y. G.; Ren, Y.; Liu, Y. Z.; Wen, J. G.; Okasinski, J. S.; Miller, D. J., Ambient-stable tetragonal phase in silver nanostructures. *Nat Commun* **2012**, *3*.

83. Feng, Y. H.; He, J. T.; Wang, H.; Tay, Y. Y.; Sun, H.; Zhu, L. F.; Chen, H. Y., An Unconventional Role of Ligand in Continuously Tuning of Metal-Metal Interfacial Strain. *J Am Chem Soc* **2012**, *134* (4), 2004-2007.

84. Feng, Y. H.; Wang, Y. W.; He, J. T.; Song, X. H.; Tay, Y. Y.; Hng, H. H.; Ling, X. Y.; Chen, H. Y., Achieving Site-Specificity in Multistep Colloidal Synthesis. *J Am Chem Soc* **2015**, *137* (24), 7624-7627.

85. Gramotnev, D. K.; Bozhevolnyi, S. I., Plasmonics beyond the diffraction limit. *Nat. Photon.* **2010**, *4* (2), 83-91.
86. Choi, H. K.; Shon, H. K.; Yu, H.; Lee, T. G.; Kim, Z. H., b(2) Peaks in SERS Spectra of 4-Aminobenzenethiol: A Photochemical Artifact or a Real Chemical Enhancement? *J Phys Chem Lett* **2013**, *4* (7), 1079-1086.
87. Dendisova, M.; Havranek, L.; Oncak, M.; Matejka, P., In Situ SERS Study of Azobenzene Derivative Formation from 4-Aminobenzenethiol on Gold, Silver, and Copper Nanostructured Surfaces: What Is the Role of Applied Potential and Used Metal? *J Phys Chem C* **2013**, *117* (41), 21245-21253.
88. Jennings, G. K.; Laibinis, P. E., Self-assembled n-alkanethiolate monolayers on underpotentially deposited adlayers of silver and copper on gold. *J Am Chem Soc* **1997**, *119* (22), 5208-5214.
89. Yin, H.; Zhao, S.; Zhao, K.; Muqsit, A.; Tang, H.; Chang, L.; Zhao, H.; Gao, Y.; Tang, Z., Ultrathin platinum nanowires grown on single-layered nickel hydroxide with high hydrogen evolution activity. *Nat commun* **2015**, *6*.
90. Zhou, B.; Shi, B. Y.; Jin, D. Y.; Liu, X. G., Controlling upconversion nanocrystals for emerging applications. *Nat Nanotechnol* **2015**, *10* (11), 924-936.
91. Mokari, T.; Sztrum, C. G.; Salant, A.; Rabani, E.; Banin, U., Formation of asymmetric one-sided metal-tipped semiconductor nanocrystal dots and rods. *Nat Mater* **2005**, *4* (11), 855-863.
92. Li, J.; Cushing, S. K.; Meng, F.; Senty, T. R.; Bristow, A. D.; Wu, N., Plasmon-induced resonance energy transfer for solar energy conversion. *Nat Photon* **2015**, *9* (9), 601-607.

93. Christopher, P.; Xin, H. L.; Linic, S., Visible-light-enhanced catalytic oxidation reactions on plasmonic silver nanostructures. *Nature Chem* **2011**, *3* (6), 467-472.
94. Li, Z. T.; Zhu, Z. N.; Liu, W. J.; Zhou, Y. L.; Han, B.; Gao, Y.; Tang, Z. Y., Reversible Plasmonic Circular Dichroism of Au Nanorod and DNA Assemblies. *J Am Chem Soc* **2012**, *134* (7), 3322-3325.
95. Linic, S.; Aslam, U.; Boerigter, C.; Morabito, M., Photochemical transformations on plasmonic metal nanoparticles. *Nat Mater* **2015**, *14* (6), 567-576.
96. Lin, J. D.; Li, H.; Zhang, H.; Chen, W., Plasmonic enhancement of photocurrent in MoS<sub>2</sub> field-effect-transistor. *Appl Phys Lett* **2013**, *102* (20).
97. Lim, D. K.; Jeon, K. S.; Kim, H. M.; Nam, J. M.; Suh, Y. D., Nanogap-engineerable Raman-active nanodumbbells for single-molecule detection. *Nat Mater* **2010**, *9* (1), 60-67.
98. Brongersma, M. L.; Halas, N. J.; Nordlander, P., Plasmon-induced hot carrier science and technology. *Nat Nanotechnol* **2015**, *10* (1), 25-34.
99. Nhxxy1118, The Environment Change in Shi Zuishan. Baidu Library: 2011.
100. Lassiter, J. B.; Aizpurua, J.; Hernandez, L. I.; Brandl, D. W.; Romero, I.; Lal, S.; Hafner, J. H.; Nordlander, P.; Halas, N. J., Close encounters between two nanoshells. *Nano Lett* **2008**, *8* (4), 1212-1218.
101. Wen, F.; Zhang, Y.; Gottheim, S.; King, N. S.; Zhang, Y.; Nordlander, P.; Halas, N. J., Charge Transfer Plasmons: Optical Frequency Conductances and Tunable Infrared Resonances. *ACS nano* **2015**, *9* (6), 6428-6435.

102. Liu, N.; Tang, M. L.; Hentschel, M.; Giessen, H.; Alivisatos, A. P., Nanoantenna-enhanced gas sensing in a single tailored nanofocus. *Nat Mater* **2011**, *10* (8), 631-636.
103. Perez-Gonzalez, O.; Zabala, N.; Borisov, A. G.; Halas, N. J.; Nordlander, P.; Aizpurua, J., Optical Spectroscopy of Conductive Junctions in Plasmonic Cavities. *Nano Lett.* **2010**, *10* (8), 3090-3095.
104. Dong, S.; Zhan, K.; Yu, Z. P.; Fan, J. A., Electrochemically Programmable Plasmonic Antennas. *ACS nano* **2016**, *10* (7), 6716-6724.
105. Zhang, P.; Wang, T.; Gong, J., Mechanistic Understanding of the Plasmonic Enhancement for Solar Water Splitting. *Adv Mater* **2015**, *27* (36), 5328-5342.
106. Knight, M. W.; Sobhani, H.; Nordlander, P.; Halas, N. J., Photodetection with Active Optical Antennas. *Science* **2011**, *332* (6030), 702-704.
107. Shim, M.; McDaniel, H., Anisotropic nanocrystal heterostructures: Synthesis and lattice strain. *Curr Opin Solid St M* **2010**, *14* (5), 83-94.
108. Chen, H.; Qiu, Q.; Sharif, S.; Ying, S.; Wang, Y.; Ying, Y., Solution-Phase Synthesis of Platinum Nanoparticle-Decorated Metal-Organic Framework Hybrid Nanomaterials as Biomimetic Nanoenzymes for Biosensing Applications. *ACS Appl Mater Interfaces* **2018**, *10* (28), 24108-24115.
109. Hodges, J. M.; Biacchi, A. J.; Schaak, R. E., Ternary Hybrid Nanoparticle Isomers: Directing the Nucleation of Ag on Pt-Fe<sub>3</sub>O<sub>4</sub> Using a Solid-State Protecting Group. *ACS nano* **2014**, *8* (1), 1047-1055.
110. Wang, L.; Chen, R.; Ren, Z. F.; Ge, C. W.; Liu, Z. X.; He, S. J.; Yu, Y. Q.; Wu, C. Y.; Luo, L. B., Plasmonic silver nanosphere enhanced ZnSe nanoribbon/Si heterojunction optoelectronic devices. *Nanotechnology* **2016**, *27* (21).

111. Liang, Z. Q.; Sun, J.; Jiang, Y. Y.; Jiang, L.; Chen, X. D., Plasmonic Enhanced Optoelectronic Devices. *Plasmonics* **2014**, *9* (4), 859-866.
112. Guo, C. X.; Xie, J.; Yang, H.; Li, C. M., Au@CdS Core-Shell Nanoparticles-Modified ZnO Nanowires Photoanode for Efficient Photoelectrochemical Water Splitting. *Adv Sci (Weinh)* **2015**, *2* (12), 1500135.
113. Sun, Z.; Yang, Z.; Zhou, J.; Yeung, M. H.; Ni, W.; Wu, H.; Wang, J., A general approach to the synthesis of gold-metal sulfide core-shell and heterostructures. *Angewandte Chemie* **2009**, *48* (16), 2881-5.
114. Wu, B. H.; Liu, D. Y.; Mubeen, S.; Chuong, T. T.; Moskovits, M.; Stucky, G. D., Anisotropic Growth of TiO<sub>2</sub> onto Gold Nanorods for Plasmon-Enhanced Hydrogen Production from Water Reduction. *J Am Chem Soc* **2016**, *138* (4), 1114-1117.
115. Niu, Z.; Cui, F.; Yu, Y.; Becknell, N.; Sun, Y.; Khanarian, G.; Kim, D.; Dou, L.; Dehestani, A.; Schierle-Arndt, K.; Yang, P., Ultrathin Epitaxial Cu@Au Core-Shell Nanowires for Stable Transparent Conductors. *J Am Chem Soc* **2017**, *139* (21), 7348-7354.
116. Zhang, S.; Zeng, H. C., Solution-Based Epitaxial Growth of Magnetically Responsive Cu@Ni Nanowires. *Chem Mater* **2010**, *22* (4), 1282-1284.
117. Hong, J. W.; Wi, D. H.; Lee, S.-U.; Han, S. W., Metal–Semiconductor Heteronanocrystals with Desired Configurations for Plasmonic Photocatalysis. *J Am Chem Soc* **2016**, *138* (48), 15766-15773.
118. Lee, S.-U.; Hong, J. W.; Choi, S.-I.; Han, S. W., Universal Sulfide-Assisted Synthesis of M–Ag Heterodimers (M = Pd, Au, Pt) as Efficient Platforms for Fabricating Metal–Semiconductor Heterostructures. *J Am Chem Soc* **2014**, *136* (14), 5221-5224.



119. Pang, M.; Hu, J.; Zeng, H. C., Synthesis, Morphological Control, and Antibacterial Properties of Hollow/Solid Ag<sub>2</sub>S/Ag Heterodimers. *J Am Chem Soc* **2010**, *132* (31), 10771-10785.
120. Tan, C.; Chen, J.; Wu, X.-J.; Zhang, H., Epitaxial growth of hybrid nanostructures. *Nature Reviews Materials* **2018**, *3*, 17089.
121. Habas, S. E.; Lee, H.; Radmilovic, V.; Somorjai, G. A.; Yang, P., Shaping binary metal nanocrystals through epitaxial seeded growth. *Nat Mater* **2007**, *6* (9), 692-697.
122. Kim, M.; Ko, S. M.; Kim, J.-M.; Son, J.; Lee, C.; Rhim, W.-K.; Nam, J.-M., Dealloyed Intra-Nanogap Particles with Highly Robust, Quantifiable Surface-Enhanced Raman Scattering Signals for Biosensing and Bioimaging Applications. *Acs Central Sci* **2018**, *4* (2), 277-287.
123. Mulvihill, M. J.; Ling, X. Y.; Henzie, J.; Yang, P., Anisotropic Etching of Silver Nanoparticles for Plasmonic Structures Capable of Single-Particle SERS. *J Am Chem Soc* **2010**, *132* (1), 268-274.
124. Xue, G.; Dong, J., Stable silver substrate prepared by the nitric acid etching method for a surface-enhanced Raman scattering study. *Anal Chem* **1991**, *63* (20), 2393-2397.
125. Mikhlin, Y. L.; Vishnyakova, E. A.; Romanchenko, A. S.; Saikova, S. V.; Likhatski, M. N.; Larichev, Y. V.; Tuzikov, F. V.; Zaikovskii, V. I.; Zharkov, S. M., Oxidation of Ag nanoparticles in aqueous media: Effect of particle size and capping. *Appl Surf Sci* **2014**, *297*, 75-83.
126. Chen, J.; McLellan, J. M.; Siekkinen, A.; Xiong, Y.; Li, Z. Y.; Xia, Y., Facile synthesis of gold-silver nanocages with controllable pores on the surface. *J Am Chem Soc* **2006**, *128* (46), 14776-7.

127. Skrabalak, S. E.; Chen, J.; Au, L.; Lu, X.; Li, X.; Xia, Y., Gold Nanocages for Biomedical Applications. *Adv Mater* **2007**, *19* (20), 3177-3184.
128. Skrabalak, S. E.; Au, L.; Li, X.; Xia, Y., Facile synthesis of Ag nanocubes and Au nanocages. *Nat Protoc* **2007**, *2* (9), 2182-90.
129. MacDonald, K. F.; Sámson, Z. L.; Stockman, M. I.; Zheludev, N. I., Ultrafast active plasmonics. *Nat. Photon.* **2008**, *3*, 55.
130. Jiang, Y.; Tian, B., Inorganic semiconductor biointerfaces. *Nature Reviews Materials* **2018**.
131. Di Bartolomeo, A., Graphene Schottky diodes: An experimental review of the rectifying graphene/semiconductor heterojunction. *Phys Rep* **2016**, *606*, 1-58.
132. Kasper, M.; Gramse, G.; Hoffmann, J.; Gaquiere, C.; Feger, R.; Stelzer, A.; Smoliner, J.; Kienberger, F., Metal-oxide-semiconductor capacitors and Schottky diodes studied with scanning microwave microscopy at 18 GHz. *J Appl Phys* **2014**, *116* (18).
133. Hagedorn, K.; Li, W. Y.; Liang, Q. J.; Dilger, S.; Noebels, M.; Wagner, M. R.; Reparaz, J. S.; Dollinger, A.; Gunne, J. S. A. D.; Dekorsy, T.; Schmidt-Mende, L.; Polarz, S., Catalytically Doped Semiconductors for Chemical Gas Sensing: Aerogel-Like Aluminum-Containing Zinc Oxide Materials Prepared in the Gas Phase. *Adv Funct Mater* **2016**, *26* (20), 3424-3437.
134. Yu, X.; Li, L.; Su, Y.; Jia, W.; Dong, L.; Wang, D.; Zhao, J.; Li, Y., Platinum-Copper Nanoframes: One-Pot Synthesis and Enhanced Electrocatalytic Activity. *Chemistry* **2016**, *22* (14), 4960-5.
135. Xu, J.; Cui, J.; Guo, C.; Zhao, Z.; Jiang, R.; Xu, S.; Zhuang, Z.; Huang, Y.; Wang, L.; Li, Y., Ultrasmall Cu<sub>7</sub> S<sub>4</sub> @MoS<sub>2</sub> Hetero-Nanoframes with Abundant

Active Edge Sites for Ultrahigh-Performance Hydrogen Evolution. *Angewandte Chemie* **2016**, *55* (22), 6502-5.

136. Pei, J.; Mao, J.; Liang, X.; Chen, C.; Peng, Q.; Wang, D.; Li, Y., Ir-Cu nanoframes: one-pot synthesis and efficient electrocatalysts for oxygen evolution reaction. *Chemical communications* **2016**, *52* (19), 3793-6.

137. Ma, H.; Li, Y.; Wang, Y.; Hu, L.; Zhang, Y.; Fan, D.; Yan, T.; Wei, Q., Cubic Cu<sub>2</sub>O nanoframes with a unique edge-truncated structure and a good electrocatalytic activity for immunosensor application. *Biosens Bioelectron* **2016**, *78*, 167-173.

138. Becknell, N.; Kang, Y.; Chen, C.; Resasco, J.; Kornienko, N.; Guo, J.; Markovic, N. M.; Somorjai, G. A.; Stamenkovic, V. R.; Yang, P., Atomic Structure of Pt<sub>3</sub>Ni Nanoframe Electrocatalysts by in Situ X-ray Absorption Spectroscopy. *J Am Chem Soc* **2015**, *137* (50), 15817-24.

139. Chen, C.; Kang, Y.; Huo, Z.; Zhu, Z.; Huang, W.; Xin, H. L.; Snyder, J. D.; Li, D.; Herron, J. A.; Mavrikakis, M.; Chi, M.; More, K. L.; Li, Y.; Markovic, N. M.; Somorjai, G. A.; Yang, P.; Stamenkovic, V. R., Highly crystalline multimetallic nanoframes with three-dimensional electrocatalytic surfaces. *Science* **2014**, *343* (6177), 1339-43.

140. Camposeo, A.; Persano, L.; Manco, R.; Wang, Y.; Del Carro, P.; Zhang, C.; Li, Z. Y.; Pisignano, D.; Xia, Y., Metal-Enhanced Near-Infrared Fluorescence by Micropatterned Gold Nanocages. *ACS nano* **2015**, *9* (10), 10047-54.

141. Xia, Y.; Skrabalak, S. E., Improving biomedical imaging with gold nanocages. *SPIE Newsroom* **2008**, 1200705 1135.

142. Zhang, L.; Roling, L. T.; Wang, X.; Vara, M.; Chi, M.; Liu, J.; Choi, S. I.; Park, J.; Herron, J. A.; Xie, Z.; Mavrikakis, M.; Xia, Y., NANOCATALYSTS.

Platinum-based nanocages with subnanometer-thick walls and well-defined, controllable facets. *Science* **2015**, *349* (6246), 412-6.

143. Oh, M. H.; Yu, T.; Yu, S. H.; Lim, B.; Ko, K. T.; Willinger, M. G.; Seo, D. H.; Kim, B. H.; Cho, M. G.; Park, J. H.; Kang, K.; Sung, Y. E.; Pinna, N.; Hyeon, T., Galvanic replacement reactions in metal oxide nanocrystals. *Science* **2013**, *340* (6135), 964-8.

144. Wu, H.-L.; Sato, R.; Yamaguchi, A.; Kimura, M.; Haruta, M.; Kurata, H.; Teranishi, T., Formation of pseudomorphic nanocages from Cu<sub>2</sub>O nanocrystals through anion exchange reactions. *Science* **2016**, *351* (6279), 1306-1310.

145. Becknell, N.; Son, Y.; Kim, D.; Li, D. G.; Yu, Y.; Niu, Z. Q.; Lei, T.; Sneed, B. T.; More, K. L.; Markovic, N. M.; Stamenkovic, V. R.; Yang, P. D., Control of Architecture in Rhombic Dodecahedral Pt-Ni Nanoframe Electrocatalysts. *J Am Chem Soc* **2017**, *139* (34), 11678-11681.

146. Kwon, T.; Jun, M.; Kim, H. Y.; Oh, A.; Park, J.; Baik, H.; Joo, S. H.; Lee, K., Vertex-Reinforced PtCuCo Ternary Nanoframes as Efficient and Stable Electrocatalysts for the Oxygen Reduction Reaction and the Methanol Oxidation Reaction. *Adv Funct Mater* **2018**, *28* (13).

147. Kwon, H.; Kabiraz, M. K.; Park, J.; Oh, A.; Baik, H.; Choi, S. I.; Lee, K., Dendrite-Embedded Platinum-Nickel Multiframes as Highly Active and Durable Electrocatalyst toward the Oxygen Reduction Reaction. *Nano Lett* **2018**, *18* (5), 2930-2936.

148. Park, J.; Sa, Y. J.; Baik, H.; Kwon, T.; Joo, S. H.; Lee, K., Iridium-Based Multimetallic Nanoframe@Nanoframe Structure: An Efficient and Robust

Electrocatalyst toward Oxygen Evolution Reaction. *ACS nano* **2017**, *11* (6), 5500-5509.

149. Park, J.; Kanti Kabiraz, M.; Kwon, H.; Park, S.; Baik, H.; Choi, S. I.; Lee, K., Radially Phase Segregated PtCu@PtCuNi Dendrite@Frame Nanocatalyst for the Oxygen Reduction Reaction. *ACS nano* **2017**, *11* (11), 10844-10851.

150. Park, J.; Kim, J.; Yang, Y.; Yoon, D.; Baik, H.; Haam, S.; Yang, H.; Lee, K., RhCu 3D Nanoframe as a Highly Active Electrocatalyst for Oxygen Evolution Reaction under Alkaline Condition. *Adv Sci* **2016**, *3* (4).

151. Oh, A.; Baik, H.; Choi, D. S.; Cheon, J. Y.; Kim, B.; Kim, H.; Kwon, S. J.; Joo, S. H.; Jung, Y.; Lee, K., Skeletal Octahedral Nanoframe with Cartesian Coordinates via Geometrically Precise Nanoscale Phase Segregation in a Pt@Ni Core-Shell Nanocrystal. *ACS nano* **2015**, *9* (3), 2856-2867.

152. Sadovnikov, S. I.; Gusev, A. I., Recent progress in nanostructured silver sulfide: from synthesis and nonstoichiometry to properties. *J Mater Chem A* **2017**, *5* (34), 17676-17704.

153. Dong, L.; Ji, G.; Liu, Y.; Xu, X.; Lei, P.; Du, K.; Song, S.; Feng, J.; Zhang, H., Multifunctional Cu–Ag<sub>2</sub>S nanoparticles with high photothermal conversion efficiency for photoacoustic imaging-guided photothermal therapy in vivo. *Nanoscale* **2018**, *10* (2), 825-831.

154. Jiang, Q.; Zeng, W.; Zhang, C.; Meng, Z.; Wu, J.; Zhu, Q.; Wu, D.; Zhu, H., Broadband absorption and enhanced photothermal conversion property of octopod-like Ag@Ag<sub>2</sub>S core@shell structures with gradually varying shell thickness. *Sci Rep-Uk* **2017**, *7* (1), 17782.

155. Ding, X.; Liow, C. H.; Zhang, M.; Huang, R.; Li, C.; Shen, H.; Liu, M.; Zou, Y.; Gao, N.; Zhang, Z.; Li, Y.; Wang, Q.; Li, S.; Jiang, J., Surface Plasmon

Resonance Enhanced Light Absorption and Photothermal Therapy in the Second Near-Infrared Window. *J Am Chem Soc* **2014**, *136* (44), 15684-15693.

156. Ruiz, D.; del Rosal, B.; Acebrón, M.; Palencia, C.; Sun, C.; Cabanillas-González, J.; López-Haro, M.; Hungría, A. B.; Jaque, D.; Juarez, B. H., Ag/Ag<sub>2</sub>S Nanocrystals for High Sensitivity Near-Infrared Luminescence Nanothermometry. *Adv Funct Mater* **2016**, *27* (6), 1604629.

157. Feng, Y.; Liu, H.; Yang, J., A selective electrocatalyst-based direct methanol fuel cell operated at high concentrations of methanol. *Sci Adv* **2017**, *3* (6).

158. Wang, D.; Hao, C.; Zheng, W.; Peng, Q.; Wang, T.; Liao, Z.; Yu, D.; Li, Y., Ultralong Single-Crystalline Ag<sub>2</sub>S Nanowires: Promising Candidates for Photoswitches and Room-Temperature Oxygen Sensors. *Adv Mater* **2008**, *20* (13), 2628-2632.

159. Shi, X.; Chen, H.; Hao, F.; Liu, R.; Wang, T.; Qiu, P.; Burkhardt, U.; Grin, Y.; Chen, L., Room-temperature ductile inorganic semiconductor. *Nat Mater* **2018**, *17* (5), 421-426.